

Magnetic and structural properties of thin films and nanoparticles studied by scattering methods

Der Fakultät für Mathematik, Informatik und Naturwissenschaften der Rheinisch-
Westfälischen Technischen Hochschule Aachen vorgelegte Dissertation zur Erlangung des
akademischen Grades eines Doktors der Naturwissenschaften

von

Master of Science

Mikhail Feygenson

aus

Komsomolsk-on-Amure, Russische Föderation

Berichter: Universitätsprofessor Dr. Thomas Brückel

Tag der mündlichen Prüfung: 05.06.2007

Diese Dissertation ist auf den Internetseiten der Hochschulbibliothek online verfügbar

Zusammenfassung

Diese Arbeit befasst sich mit der Untersuchung der magnetischen und strukturellen Eigenschaften von magnetischen Dünnschichten und Nanopartikeln mittels Streumethoden.

Die Struktur von epitaktisch gewachsenen Fe/Cr/Fe Übergittern wurde mit anomaler Röntgenstreuung untersucht, dabei wurden zwei verschiedene Röntgenenergien verwendet: (i) $E_1=5985\text{eV}$, nah an der Cr K-Kante, um den maximalen Kontrast der Fe/Cr Grenzflächen zu erzeugen und (ii) $E_2=6940\text{eV}$ am Punkt des geringsten Kontrastes zwischen Eisen und Chrom. Es wurden die spekuläre Reflektivität, longitudinale diffuse Streuung und Omega-Scan für beide Energien gemessen. Die Simulationen im Rahmen der Bornschen Näherung mit gestörten Wellen (DWBA - Distorted Wave Born Approximation), erlaubten uns die Morphologie der Grenzflächen quantitativ zu beschreiben. Sowohl die Rauheit, der Hurst Parameter und die Dicke jeder Schicht als auch eine Oxidationsschicht an der Oberfläche der Probe konnten aus den Daten abgeleitet werden. Die Stärken und Grenzen dieser Methode werden in der Arbeit dargelegt. Der Einfluss des Confinements auf das magnetische Verhalten wurde anhand von in porösem Glas eingebetteten MnO, mittels Beobachtung der magnetischen Ordnung und des Phasenübergangs durch polarisierte Neutronenstreuung, untersucht.

Die Nanoporen, die mit MnO gefüllt sind, sind wurmartige Strukturen mit einem typischen Durchmesser von 7nm. Aus der Temperaturabhängigkeit der Intensität des magnetischen $(\frac{1}{2}\frac{1}{2}\frac{1}{2})$ Braggreflexes ließ sich schließen, dass für MnO Nanopartikel der Phasenübergang kontinuierlich ist und bei einer Néel-Temperatur von $T_N=122\text{K}$ liegt. Dies steht im Gegensatz zum Verhalten von MnO Volumenkristallen, welches einen Phasenübergang 1. Ordnung bei 118K aufweist. Desweiteren konnte man beobachten, dass ein Teil der MnO Nanopartikel noch bei 10K ungeordnet blieben, was auf Frustration, an den Grenzen zwischen MnO und Glas, hinweist.

Der kontinuierliche Charakter und die ungewöhnliche Temperaturabhängigkeit, mit einem verringerten Ordnungsparameter, des Übergangs, wurde in einem Modell durch oberflächeninduzierte Unordnung beschrieben. Zur Untersuchung des "spin-canting" Effektes in magnetischen Nanopartikeln wurden zunächst Cobalt Nanopartikel synthetisiert. Dazu wurden Wasser-in-Öl Mikroemulsionen verwendet, die durch nichtionische Tenside wie C_{12}E_5 oder Igepal CO520 stabilisiert wurden und in der wässrigen Phase NaBH_4 enthielten.

Die Bildung der Co Nanopartikel erfolgte unmittelbar bei Zugabe einer Lösung von $\text{Co}(\text{AOT})_2$ in Hexan. Es wurde festgestellt, dass schon das in der Mikroemulsion enthaltene Wasser zur Oxidation der Partikel führt. Daher wurde ein neuer Syntheseweg entwickelt, der aus der Reduktion von wasserfreien $\text{Co}(\text{AOT})_2$ Mizellenlösungen mit verschiedenen organischen Borhydriden besteht. Diese Partikel sind in Lösung und unter Stickstoffatmosphäre aufbewahrt für Wochen gegen Oxidation stabil. Zur strukturellen Charakterisierung der Co Nanopartikel wurden Kleinwinkelstreuexperimente an der JUSIFA beamline des DORIS Speicherringes am HASYLAB in Hamburg durchgeführt. Die Verfeinerung der gemessenen Streukurven im Rahmen des Beaucage Formalismus liefert Partikelgrößen von 3.8(5) bzw. 5.4(1) nm. Zur magnetischen Charakterisierung wurden SQUID-Messungen an den Partikeln in Lösung durchgeführt, wofür zunächst ein neuer Probenhalter entwickelt werden musste. Die gemessenen Co Nanopartikel sind superparamagnetisch mit einer blocking-Temperatur von etwa 10K.

Summary

The present work concerns the magnetic and structural proprieties of magnetic thin films and magnetic nanoparticles studied by scattering methods.

The structural properties of epitaxially grown Fe/Cr/Fe trilayer were studied with anomalous x-ray scattering. Two different x-ray energies have been used; (i) one $E_1=5985\text{eV}$ to match the maximum contrast of the Fe/Cr interface close to the Cr absorption K-edge and (ii) a second one $E_2=6940\text{eV}$ where the Fe/Cr interface displays the lowest contrast. The specular reflectivity and longitudinal diffuse scans together with omega scans for both energies were measured. The simulations within the frame of Distorted Wave Born Approximation (DWBA) allowed us to describe quantitatively the morphology of each interface. The roughness, Hurst parameter and the thickness of every layer as well as an oxidation effect at the surface of the sample are derived. The strength and limitations of the method are discussed. The influence of confinement on the magnetic behavior, was investigated in MnO embedded in a porous glass. We studied the magnetic order and phase transition of MnO nanoparticles by polarized neutron scattering.

The nanopores filled with MnO are wormlike structures with a typical diameter of 7nm. From the temperature dependence of the magnetic $(\frac{1}{2} \frac{1}{2} \frac{1}{2})$ Bragg intensity we obtained that for the MnO nanoparticles the phase transition is continuous with a Néel temperature $T_N=122\text{K}$. This is in contrast to bulk MnO, which exhibits a first order phase transition at 118K. Furthermore, we observed that a part of the MnO nanoparticle material remains disordered even at 10K, which indicates frustration at the interface MnO to glass.

The continuous character of the transition and the unusual temperature dependence with a reduced order parameter was described and modelled by surface induced disorder.

In order to study the spin-canting effect in magnetic nanoparticles, we explored a synthesis route of Co nanoparticles in which we employed water-in-oil microemulsions that are stabilized by the nonionic surfactants of the ethoxylated alkyl- or arylether series such as C₁₂E₅ and Igepal CO520 and contain the NaBH₄-solution. Co nanoparticle formation is then induced by injecting a solution of Co(AOT)₂ in hexane. We found out that the water inside the microemulsion leads already to oxidation of the particles.

Therefore we developed a new route without water by reducing Co(AOT)_2 micellar solutions with different organic borhydrides for particle synthesis. These particles are stable in solution against oxidation for weeks if stored under nitrogen atmosphere.

For a structural characterization of the Co nanoparticles, we performed small-angle x-ray scattering experiments at the JUSIFA beamline of the DORIS storage ring at HASYLAB, Hamburg. A refinement of scattering curves within the Beaucage formalism yields particle diameters of 3.8 (5)nm and 5.4 (1)nm, respectively.

For a magnetic characterization, we performed SQUID measurements of the particles in solution, for which a special sample container had to be developed. The particles are superparamagnetic with a blocking temperature of about 10K.

Contents

1. Introduction to nanomagnetism	1
1.1. Magnetic materials today	1
2. Magnetic properties of thin films	3
2.1. The giant magnetoresistance effect	3
2.1.1. Physics of the GMR effect	4
2.2. Exchange bias	5
2.2.1. Physics of exchange bias	8
2.3. Industrial applications of thin films	9
3. Magnetic properties of nanoparticles	12
3.1. Magnetic properties of a single nanoparticle	12
3.1.1. Single domain state	13
3.1.2. Superparamagnetism	14
3.1.3. Surface related effects	17
3.2. Magnetic properties of an assembly of nanoparticles	25
4. Experimental methods for the investigation of nanoscaled materials	31
4.1. Introduction to polarized neutron scattering	31
4.1.1. Nuclear scattering	32
4.1.2. Magnetic scattering	33
4.1.3. Nuclear spin-dependent scattering	35
4.1.4. Rules of separation	36
4.2. Structural properties by small-angle x-ray scattering	37
4.3. Magnetic and structural properties by small-angle polarized neutron scattering	42
4.3.1. Non-interacting nanoparticles	42
4.3.2. Interacting nanoparticles	44
5. Contrast variation by anomalous x-ray scattering applied to investigation of the interface morphology in a GMR Fe/Cr/Fe trilayer	47
5.1. Sample preparation	48

5.2. Experiment	48
5.3. Contrast variation	49
5.4. Specular reflectivity	51
5.5. Diffuse scattering	55
5.6. Results and discussion	59
6. Magnetic order in MnO nanoparticles	63
6.1. MnO embedded in porous glass: sample preparation	63
6.2. Physical and magnetic properties of bulk MnO	63
6.3. Diffuse neutron scattering spectrometer DNS	64
6.4. Polarized neutron scattering on MnO in porous glass	66
6.5. Analytical treatment of the measured data	69
6.5.1. Initialization of entry parameters	71
6.6. Results and discussion	74
7. Magnetic and structural properties of Co nanoparticles	77
7.1. Colloidal synthesis of nanoparticles	77
7.2. Sample preparation details	79
7.3. Magnetic properties	82
7.4. Structural properties	83
7.5. Results and discussion	88
8. Outlook: Further development of topics	91
8.1. GMR properties of Fe/Cr/Fe trilayer and multilayer compared with x-ray data	91
8.2. Magnetic correlations in MnO nanoparticles	94
8.3. Polarized neutron measurements of Co nanoparticles in solution	96
8.3.1. Background due to incoherent scattering	97
8.3.2. Required Q -range	99
8.3.3. Resolution effects	100
8.3.4. Simulations of the spin-canting effect	102
A. Scattering length density and electron density	106

B. Calculation of the peak-to-background ratio for magnetic Bragg peak at low temperature	107
C. The list of the frequently used symbols and abbreviations	112
D. Acknowledgments	114
E. Curriculum Vitae	115
F. Eidesstattliche Erklärung	116
References	117

1. INTRODUCTION TO NANOMAGNETISM

This work deals with modern aspects of nanomagnetism, focusing on novel approaches to its interpretation. With scattering methods we will take a deep look into the magnetic and structural properties of nanoscaled materials. Aspects of nonmagnetic materials on various length scales are covered in this thesis, spanning from magnetic nanoparticles with sizes below 10nm in solution up to influence of confinement on a 100nm length scale on magnetic phase transition. The advances made in experimental techniques over the last decade new generation synchrotron source or high flux neutron instruments, allows investigation of nanomagnetism in great detail, which was inaccessible in the last century.

In the next sections we will try to give an answer to the following questions:

What are the challenges in the study of nanomagnetism in fundamental research?

What is the importance of nanomagnetism for applications?

1.1. Magnetic materials today

Before starting a discussion about challenges in the field of nanomagnetism let us first clarify the importance of magnetic materials and the role they play in the modern world.

The global market for magnetic materials was worth about 30B\$/year in 1999 [1] and this number is continuously increasing.

The research of magnetism has never stopped since ancient times, when the first application of iron and loadstone as the south-pointer and compass has emerged. The different ages in the history of magnetism are nicely outlined by J.M.D. Coey (Tab.I).

TABLE I: The ages of of the history of the magnetism according to J.M.D. Coey [4].

Age	Time	Key names	Driver	Achievements	Materials	Applications/devices
Ancient	-1000-1500	Shen Kua	State	Force field,	Iron, Lodestone	South-pointer, compass
		Petrus		induced magnetism,		
		Peregrinus		thermoremanence		
Early	1500-1820	Gilbert	Navy	Earth's field	Iron,	Dip circle,
		Descartes			Lodestone	Horseshoe magnet
		D. Bernoulli				
Electromagnetic	1820-1900	Oersted, Ampere,	Industry (infrastructure)	Electromagnetic induction,	Electrical steels	Motors, generators, telegraph, wireless, magnetic recording
		Faraday,		Maxwell's		
		Maxwell, Hertz		equations		
Understanding	1900-1935	Weiss, Bohr,	Academy	Spin, Exchange	Alnico	
		Heisenberg,		interactions		
		Pauli, Dirac,				
		Landau				
High frequency	1935-1960	Bloch, Pound,	Military	Microwaves, EPR,	Ferrites	Radar, television, MRI
		Purcell		FMR, NMR		
Applications	1960-1995		Industry	New materials	Nd-Fe-B,	Consumer
			(consumers)	miniaturisation of magnetic circuits	Sm-Co	electronics
Spin Electronics	1995-...		Industry	Thin film devices	Multilayers	High density
			(consumers)			magnetic recording, MRAM...

According to his classification, we have entered the age of spin electronics or spintronics, where the spin of the electron, not just its charge, is employed for information storage, processing and transport. Besides the many fundamental challenges in nanomagnetism outlined below, it is their potential applications which drive the research field of nanomagnetism.

2. MAGNETIC PROPERTIES OF THIN FILMS

2.1. The giant magnetoresistance effect

The giant magnetoresistance (GMR) effect is a beautiful example how the discovery of a novel quantum mechanical effect in magnetism has driven fundamental research and led to an impressive breakthrough in technology. The effect was observed in 1988 simultaneously by P.Grünberg [2] and A.Fert [3]. A significant decrease of the resistance was observed in a Fe/Cr/Fe trilayer at an applied magnetic field compared to zero field resistance. In general, a GMR system is composed of two ferromagnetic layers separated by a non-magnetic spacer with a thickness of several Angstroms. Its thickness is chosen such that an antiparallel coupling of the ferromagnetic layers occurs at the absence of an external magnetic field due to interlayer exchange coupling [2]. The application of a magnetic field of several tens of milli Tesla forces magnetization of the two FM layers to become parallel. Now if one compares the resistance of a multilayer GMR system with and without the external magnetic field the difference is about 80% as it was shown by M.N.Baibich et al., (Fig.1). The understanding of the GMR effect lies in the quantum description of an electron. It is known that in a ferromagnetic material an electron has a spin which can be aligned parallel or antiparallel ("spin up" and "spin down", respectively) to the direction of the magnetization. In an external magnetic field the layers are saturated and aligned parallel to each other. The electrons with the spin parallel to the magnetization direction in the magnetic layers are weakly scattered and contribute to the current. Opposite to this case the electrons with the spin antiparallel to the magnetization direction undergo strong scattering and play a minor role in the charge transport. As a result, in an applied magnetic field the resistance is smaller compared to zero-field.

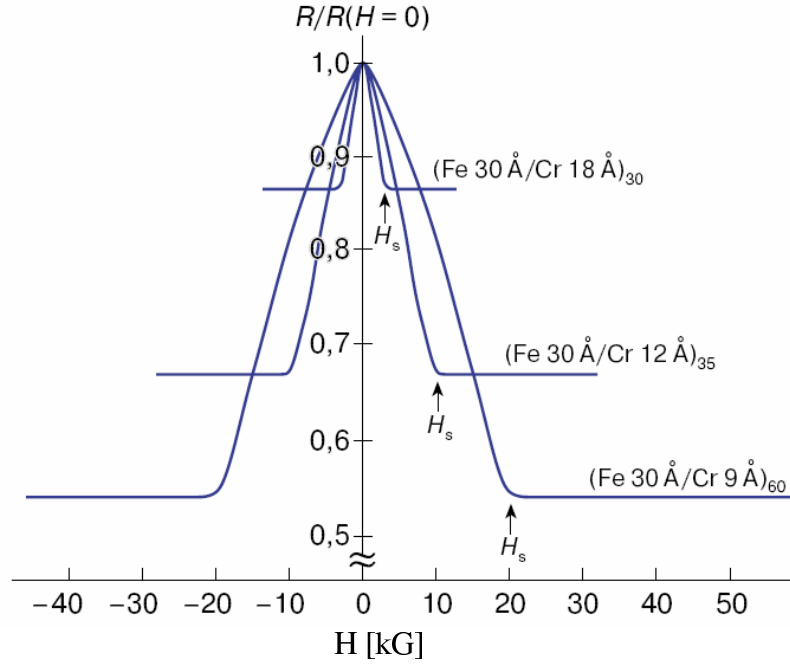


FIG. 1: The GMR effect for Fe/Cr multilayers at $T=4.2\text{K}$. The current and the applied field are along the same $[110]$ axis in the plane of the layers. Taken from [3].

2.1.1. Physics of the GMR effect

The magnetoresistance effect itself is the relative change of the resistance in an external magnetic field.

$$\delta_H = \frac{\rho(H) - \rho(0)}{\rho(0)} \quad (1)$$

Where $\rho(0)$ is the resistance at zero magnetic field and $\rho(H)$ at the magnetic field H . For Fe and Co the longitudinal magnetoresistance effect (when orientation of applied magnetic field and current is parallel) is about 0.07% in the field $H=1\text{T}$ at room temperature [5]. The GMR effect is about 80% for Fe/Cr superlattice at $T=4.2\text{K}$ and $H=2\text{T}$ (Fig.1). This was the reason why the new discovery got the prefix giant.

Let us explain the GMR effect using the band structure of electrons in a solid. In 3d-ferromagnetic materials (Fe,Co,Ni) the 4s-electrons and magnetic 3d-electrons are responsible for the charge transport.

Current models for the GMR effects assume that s-electrons carry mainly the current but

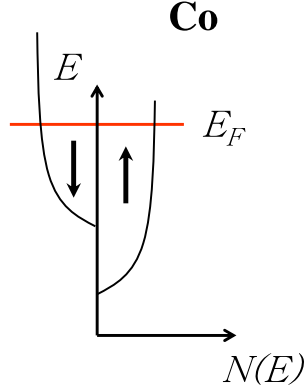


FIG. 2: The schematic density of states of majority and minority 3d-electrons for Co. E_F is the Fermi energy level.

the d -states are those into which the electrons are scattered. As it is seen from Fig.2 the density of states close to the Fermi energy is different for spin up and spin down electrons. Therefore, the electrons with spin down are scattered more than those with spin up.

In order to estimate the contribution of the spin-polarized electrons to the conductivity it is important to know the effective spin diffusion length of the polarized electron. This quantity defines the average distance travelled by an electron in a given material before a scattering process occurs which involves a change of the spin state (spin flip processes) For almost all ferromagnetics this length is in the range of $10 - 100\text{\AA}$. This is why the progress in the preparation of thin films made possible to investigate GMR effect in thin films. The amplitude of the GMR effect depends on the material and thickness of a spacer layer inside a multilayer. Normally, the thickness is in the range of $10 - 20\text{\AA}$.

2.2. Exchange bias

The exchange bias effect occurs in a system with ferromagnetic (FM) - antiferromagnetic (AFM) interface. The effect manifests itself in a shift of the hysteresis loop when the system is field cooled to the temperature lower than the Néel temperature of the AFM as it is shown in Fig.3.

The effect is associated with the additional exchange anisotropy created at the FM/AFM interface. The condition is that the Curie temperature of the FM has to be larger than the

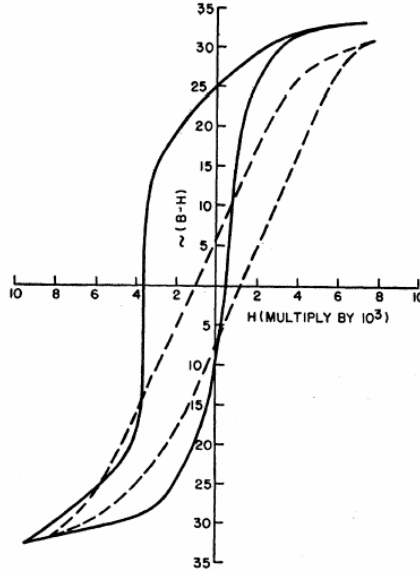


FIG. 3: The hysteresis loop of fine Co particles coated by CoO layer at 77K. The dashed line is the zero field cooled, the solid one is the saturation field cooled procedure. Taken from [6].

Néel temperature of the AFM.

The effect was observed for the first time in 1956 by Meiklejohn and Bean in Co particles coated by antiferromagnetic CoO layer.

Despite the fact that the complete quantitative description of exchange bias is still under debate, an intuitive explanation can be given.

We start from a temperature T below the Curie temperature (T_C) of the FM, but above the Néel temperature (T_N) of the AFM (Fig.4). When the sample is cooled down to a temperature lower than T_N in the presence of an external magnetic field, the spins in the bottom layer become antiferromagnetically ordered. During field reversal, the AF layer keeps its magnetic state, while magnetization of the FM layer begins to rotate. The AFM spins exert a microscopic torque on the spins of FM to keep them at their original orientation. This is why the field needed to reverse the magnetization in the FM layer becomes larger compared to that one in the absence of AFM layer.

To reverse the magnetization back to its original orientation a much smaller field is needed due to the same direction of the field and microscopic torque [6].

These two effects lead to the shift of the hysteresis loop to the left in the magnetic field axis. The effect was observed in small particles as well as in thin films. The thin films displaying

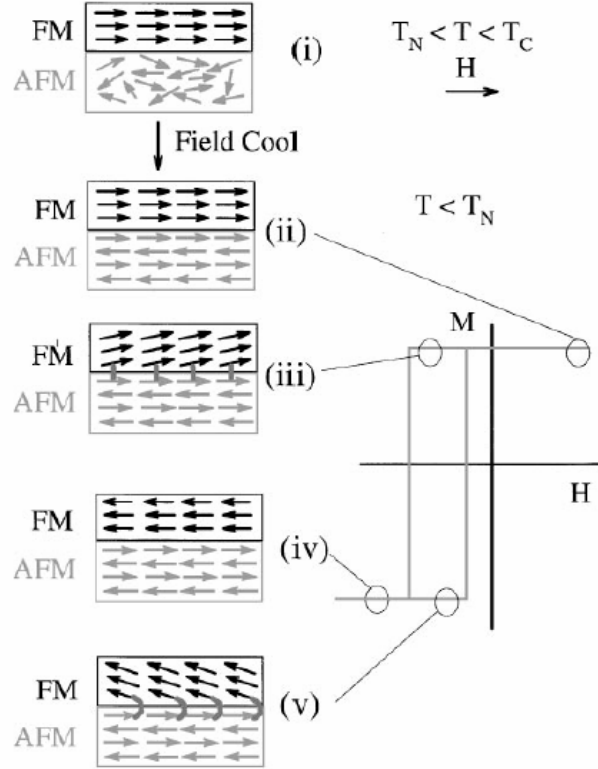


FIG. 4: Schematic representation of spins dynamic in exchange biased thin layers system. Taken from [7].

exchange bias were the most widely studied systems. The progress in thin film preparation techniques allows controlling and changing the properties of interfaces and many experimental methods are dedicated for quantitative characterization of the interfaces. The other reason of such intensive research is the industrial applications of the exchange biasing thin films which will be discussed further.

The exchange bias was observed in systems containing AFM oxides (Co-CoO, Ni-NiO, Fe-FeO), metallic AFMs ($\text{Fe}_{50}\text{Mn}_{50}$), other AFM materials (FeF_2 , MnF_2) and ferrimagnets ($\text{Fe}_{20}\text{Ni}_{80}\text{-TbCo}$, $\text{Fe}_{20}\text{Ni}_{80}\text{-DyCo}$, $\text{Fe}_{20}\text{Ni}_{80}\text{-TbFe}$ and etc). A topical review on the exchange bias effect can be found in [7].

2.2.1. Physics of exchange bias

Many experiments were carried out in order to study the dependence of exchange bias on the interfacial roughness, thickness of AFM and FM layer and strength of interaction between the spins at the interface.

However, it is possible even within the simple picture described above to introduce a model description which is qualified to explain some experimental results.

In the frame of this simple model the energy of exchange bias per unit area, assuming the coherent rotation of magnetization can be written as [8]:

$$E = -HM_{FM}t_{FM}\cos(\theta - \beta) + K_{FM}t_{FM}\sin^2\beta + K_{AFM}t_{AFM}\sin^2\alpha - J_{INT}\cos(\beta - \alpha) \quad (2)$$

Where H is applied magnetic field, M_{FM} is the saturation magnetization, t_{FM} and t_{AFM} are the thicknesses of FM and AFM layers respectively, K_{FM} and K_{AFM} are the anisotropy constants, J_{INT} is the interface coupling constant, β , α and θ are the angles defined in Fig.5. The AFM and FM anisotropy axes are assumed to be collinear.

The first term in eq.(2) accounts for the effect of the applied magnetic field on the FM layer, the second term is the effect of the FM anisotropy, the third term takes into account AFM anisotropy and the last one is the interface coupling.

In the simplest case when:

- $K_{FM}t_{FM} \ll K_{AFM}t_{AFM}$ (FM anisotropy is negligible small)
- $K_{AFM}t_{AFM} \geq J_{INT}$

the minimization of the energy with respect to the angles α and β leads to the expression for the value of the hysteresis loop shift along the field axis:

$$H_E = \frac{J_{INT}}{M_{FM}t_{FM}} \quad (3)$$

However, the predicted value of exchange bias (eq.3) is several orders of magnitude larger than the experimental results in the case when J_{INT} is taken to be similar to the ferromagnetic exchange. For the explanation of this disagreement, the simple model was modified in order to take into account the following effects: domain formation in AFM and FM layers, field effect on the AFM layer, grain size distribution, non-collinearity of AFM-FM spins, random anisotropy in the AFM layer, uncompensated surface spins, interfacial roughnesses.

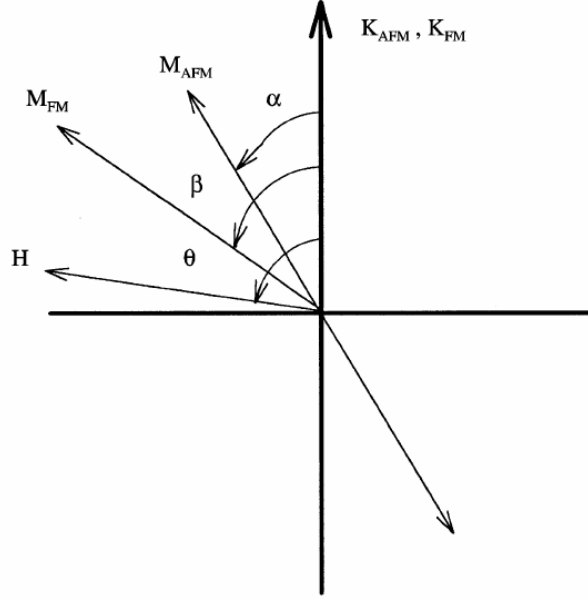


FIG. 5: The definitions of the angles involved in (2). AFM and FM anisotropy axes are assumed collinear and AFM sublattice magnetization M_{AFM} has two opposite directions. Taken from [7].

2.3. Industrial applications of thin films

In the year of discovery of the GMR effect, an initial concept for using the GMR effect in magnetic recording was disclosed [9]. For recording materials one of the most important issues is the areal density of a recording media. It defines how much information can be stored within a certain volume of a recording media. The areal density (normally expressed as billions of bits per square inch of disk surface area, $Gbits/in^2$) is the product of linear density (bits of information per inch of track) multiplied by track density (tracks per inch) [10]. In order to increase the areal density the size of the bits can be decreased. However, it will lead to the smaller writing fields. The challenge is to obtain the more sensitive reading/writing heads which could detect smaller recorded bits and read these bits at higher data rates.

Using reading heads based on the GMR effect, it was possible to achieve an areal density beyond $100 Gbyte/in^2$. Such reading heads are based on the magnetic tunnel junction (MTJ). It consists of two ferromagnetic layers separated by an isolator as it is shown in Fig.6. The magnetization of the bottom most layer (pinned layer) is fixed by the close contact with the

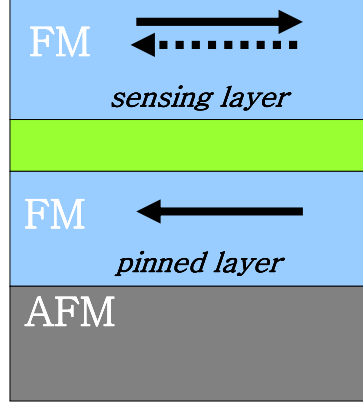


FIG. 6: The concept of the magnetic tunnel junction

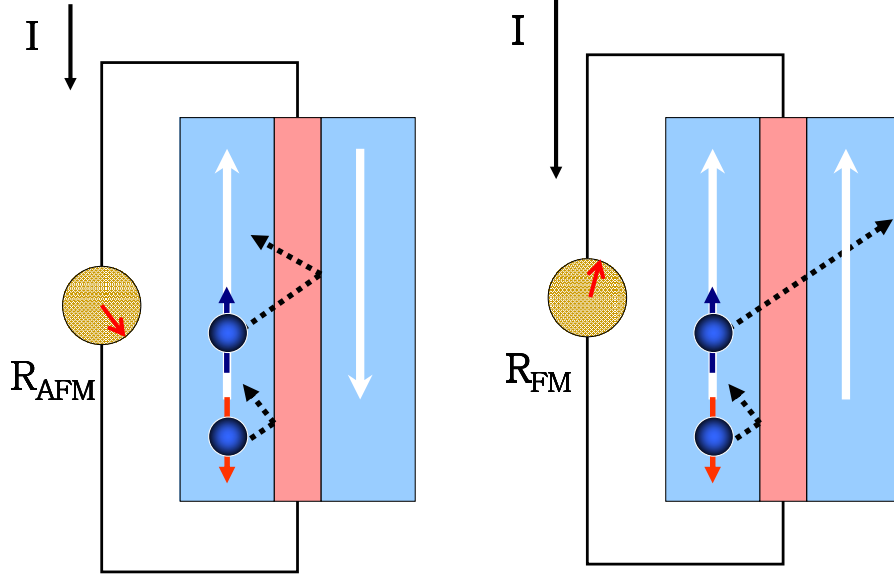


FIG. 7: The principle of the TMR effect. For the antiferromagnetic configuration of the magnetic layers $R_{AFM} \gg R_{FM}$.

antiferromagnetic layer due to the exchange biasing. The magnetization of the top most layer (sensing layer) is able to change direction even in small magnetic fields. Therefore, depending on the applied magnetic fields the configuration of pinned and sensing layers will be changed from ferromagnetic to antiferromagnetic. Such change will lead to the different tunneling current depending on the magnetic field (see Fig.7). This phenomenon is called tunneling magnetoresistance (TMR).

The MTJ is not used only for reading/writing heads but also as a basis of the Magnetic Random Access Memory (MRAM). The advantage of MRAM compare to the usual RAM is the higher speed performance and lower cost.

3. MAGNETIC PROPERTIES OF NANOPARTICLES

In this section we will give a brief introduction to new fundamental properties characteristic for nanoparticles compared to those of bulk materials.

The main difference between the bulk and nano-materials is the number of atoms involved. In case of nanoparticles most of the atoms are located at the surface. For example, fcc-Co nanoparticles with diameter around 1.6nm with a lattice constant 0.36nm, will have about 200 atoms and 60% of them will be at the surface [11].

Therefore, when the size of a material is reduced to the nanometer scale new mesoscopic phenomena characteristic of this intermediate state of matter, found neither in bulk nor in molecular systems, develop.

In the following subsections we will distinguish magnetic properties of a single nanoparticle and assembly of nanoparticles. For a single nanoparticle surface related effects and effects due to the finite size of nanoparticles are distinguished.

3.1. Magnetic properties of a single nanoparticle

The magnetic behavior of a single nanoparticle is driven by two general magnetic contributions. The first one is the magnetic behavior due to the finite-size of a particle, the second one is due to atoms located at the surface of a particle. It is a commonly accepted assumption to represent a nanoparticle as a combination of the core (where, the spins are ordered below a critical temperature, and magnetic behavior is the same as in bulk) and the shell (where the spins are disordered even at the lowest temperature). The magnetic behavior of the core and shell is quite different, leading to the competition resulting in a final magnetic state of a nanoparticle. For smaller particles the surface effects become dominant due to the larger number of spins at the surface, while in case of large particles, the magnetic behavior of the core is dominant.

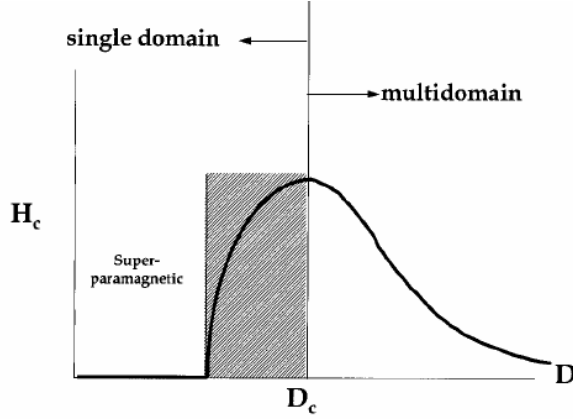


FIG. 8: Qualitative illustration of the behavior of the coercivity field in nanoparticle systems as the particle size changes. Taken from [12].

3.1.1. Single domain state

In ferromagnetic materials magnetic domains are formed in order to reduce the magnetostatic energy (demagnetizing fields) and therefore minimize the total energy. However, if the size of material is reduced down to the nanometer scale the energy cost to create a domain wall would be greater than the corresponding reduction in the magnetostatic energy. Therefore below a critical size, a ferromagnet will be in an uniform single domain state. This approximation does not take into account the surface effects, but it is good enough to explain some experimental results. This is why the "single domain" state rather defines the state where no domain walls are created. The transition to the single domain state is obviously a size dependent effect, which can be probed by a number of experimental techniques. Fig.8 qualitatively illustrates the dependence of the coercivity field H_c on the particle size. Below a critical size (which depends on the material) the H_c is zero and a superparamagnetic behavior (see below) is observed, which indicates the single domain magnetization state. The peak around the critical size is broad due to the particles size distribution. The critical size at which a particle becomes single domain is a result of competition between exchange coupling and magnetostatic energy, and therefore depends on the geometry, anisotropy, and saturation magnetic moment M_S of the particle.

The exchange length $l_{ex} = (A/\mu_0 M_S^2)^{1/2}$ is the distance where atomic exchange interactions dominate over demagnetizing fields. A is the exchange constant of order $10^{-11} J/m$, and μ_0

TABLE II: Estimated single-domain sizes for spherical particles with no shape anisotropy [12].

material	$D_{crit}[nm]$
Co	70
Fe	14
Ni	55
Fe_3O_4	128
$\gamma - Fe_2O_3$	166

is the vacuum permeability. Thus, a nanoparticle with the size of the order of l_{ex} should have a single domain magnetization state (see Tab.II).

3.1.2. Superparamagnetism

The direct consequence of the single domain state is the superparamagnetism of nanoparticles. The magnetic order in bulk materials is driven by exchange interactions, which results in a ferromagnetic or an antiferromagnetic type of the magnetic order. The paramagnetic behavior is observed above the Curie temperature (for ferromagnetics) and the Néel temperature (for antiferromagnetics) when the thermal fluctuations overcome the exchange interactions and lead to random fluctuations of atomic magnetic moments.

A similar temperature dependent behavior is typical for magnetic nanoparticles. If we assume an uniaxial anisotropy of magnetic nanoparticles then the magnetic anisotropy energy due to the magnetocrystalline and shape anisotropy is given by [13]:

$$E(\theta) = KV \sin^2 \theta \quad (4)$$

where θ is the angle between the magnetization direction and an easy direction of magnetization (easy axis), K is the uniaxial anisotropy constant, V is the volume of a nanoparticle. $\Delta E = KV$ is the anisotropy energy barrier separating both easy directions for the magnetization, which are in zero magnetic field equal to $\theta = 0$ and $\theta = \pi$. It is important that the height of the energy barrier depends on the particle size.

The relaxation time τ is the average time of transition between two minima of the magnetic

anisotropy energy over the barrier ΔE and can be expressed via Arrhenius'law [14]:

$$\tau^{-1} = f_0 e^{-\Delta E/k_B T} \quad (5)$$

where, f_0 is often taken as a constant of value 10^9s^{-1} , k_B is the Boltzmann constant, T is the temperature.

If thermal stability is desired for $\tau = 100 \text{s}$ (typical measuring time of conventional magnetometers) then

$$T_B = KV/25k_B \quad (6)$$

where, T_B is so-called the blocking temperature which depends on the size and anisotropy constant of a nanoparticle.

If non-interacting nanoparticles are ferromagnetic, they are blocked and in a ferromagnetic state with an irreversible magnetization below T_B , whereas above T_B the magnetization is reversible and the particles are characterized by superparamagnetic behavior. Assuming non-interacting nanoparticles, the anisotropy energy constant can be derived from the blocking temperature (see eq.6). In case of interacting nanoparticles, the definition of τ and T_B becomes a non-trivial task.

Experimentally, the blocking temperature can be obtained from magnetic measurements by zero-field cooled (ZFC) and field cooled (FC) procedures. At ZFC procedure the particles are cooled down to the lowest temperature possible at zero magnetic field and then the small magnetic field (in the range of tens milli Tesla) is applied and magnetization is measured as a function of temperature, during heating of the sample up to room temperature. The FC procedure is the same, but the small field is also applied during the cooling of a sample.

An example of ZFC/FC measurements for a liquid solution of Co nanoparticles is shown in Fig.15a. From this figure the blocking temperature is about 58K, where the ZFC branch displays a broad peak. The broadening of this peak is attributed to the particles size distribution. It is seen from eq.(6) that small particles experience the transition to a superparamagnetic state at lower temperatures than larger ones. However, we would like to stress again, that the blocking temperature is not only defined by the size and uniaxial anisotropy constant. In reality, nanoparticles might have crystal, shape, stress, externally induced (e.g. interaction with ligands) and exchange anisotropies (e.g. oxidation effects). As it was shown by Hormes et.al.,[15] the particles with the same size have significantly different blocking

TABLE III: The blocking temperature T_B of Co nanoparticles as a function of size and coating. Taken from [15].

Size [nm]	Blocking temperature [K]	Coating
5, 9, 12	$\sim 70, 304, 656$	"No-coating" theory
2.5	12	Oleic acid
3	28	Oleic acid
3	60	Tetraalkylammonium chlorid
3	10	Au
~ 3	>300	Au
~ 3	235	Cu
~ 3	28	SB12
3, 6, 8, 11	$\sim 10, 40, 100, 250$	Oleic acid/trioctylphosphine
4	~ 600	Polyethylene
4	10	C or Al_2O_3
4	~ 290	CoO
4.4	30	Didodecyldimethylammonium Bromide (DDAB)
5	200	CoO
5	Above 300	Polydimethylphenyloxide
5.8	58	Trioctylphosphine
6.5, 8, 9.5	60, 100, 150	Oleic acid/triphenylphosphine
8	65	Lauric acid
9	105	Oleic acid/trialkylphosphine
10	40	Oleic acid

temperatures (see Tab.III).

In the measurement of a hysteresis loop (M vs H), superparamagnetism manifests itself in the absence of a coercivity field H_c (see Fig.9), as it was schematically shown in Fig.8. For the simplest case of non-interacting nanoparticles at $MH \ll k_B T$ (superparamagnetic state) the magnetization dependence on the applied magnetic field can be described by the

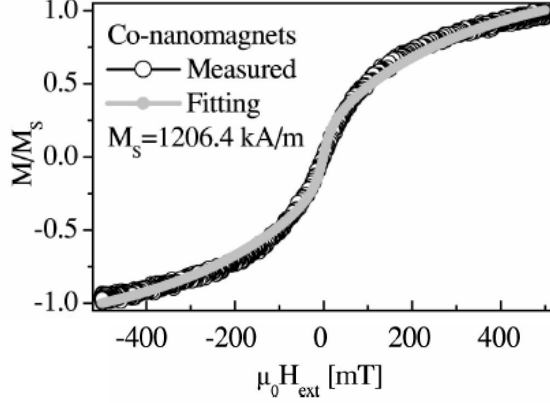


FIG. 9: Langevin fit of the normalized magnetization corresponding to the Co nanoparticles with mean size 3.3nm coated with oleic acid molecules, dispersed on carbon coated TEM Cu grid. Taken from [16].

Langevin function [16]:

$$\frac{M(H)}{M_S} = \int_0^\infty f(V) \left[\coth \left(\frac{M_S V H}{k_B T} \right) - \frac{k_B T}{M_S V H} \right] dV \quad (7)$$

where, M_S is the saturation magnetization of a single nanoparticle, $f(V)$ is the volume distribution function, V is the volume of a nanoparticle, H is an external applied magnetic field. This result is identical to the classical treatment of paramagnetism with the atomic moment replaced by the particle moment, hence the name is "superparamagnetism".

3.1.3. Surface related effects

As it was mentioned before a magnetic behavior below T_B of a nanoparticle is commonly described in terms of a magnetically ordered core and a disordered surface layer (core-shell model). Here, we will explain the differences in the behavior of surface spins compared to those in a core and new effects which arise from these differences.

Surface related effects play a major role in magnetic properties of nanoparticles due to a significant increase of the surface-to-volume ratio of atoms, compared to the bulk. The ratio increases with decreasing particle size. The reduction of the coordinate number (the total number of the nearest neighbors around a single atom) of surface atoms and the lack of

translational symmetry at the particle boundaries can introduce frustration and spin disorder.

Therefore, the competition between both magnetic orders will lead to the magnetic ground state of a nanoparticle which will be different from the simple assumption of a single domain with a perfect magnetic ordering corresponding to the bulk solid.

The model of a random canting of the surface spins caused by competing antiferromagnetic interactions between sublattices was first proposed by Coey for the explanation of a reduction of M_S in γ -Fe₂O₃ ferrimagnetic nanoparticles of 6nm in size [17]. He found that even a magnetic field of 5T was not enough to align all spins along the field. A principal finite size effect of a ferrimagnetic nanoparticle is the breaking of a large number of exchange bonds for surface atoms. In ferrites, the superexchange interaction between the magnetic cations is predominantly antiferromagnetic. The superexchange interaction is mediated by an intervening oxygen anion, when electrons are shared between 3d orbitals of the metal cations and 2p orbitals of the oxygen anions. The exchange bonds are broken when the oxygen anion is missing from the surface of a nanoparticle. If a nanoparticle is coated with an organic shell the electrons which are involved in chemical bonding no longer participate in the superexchange. In both cases the break of the exchange bonds will lead to the reduction of the effective coordination number of the surface atoms. The calculations of Kodama et.al., [18, 19] have shown that broken exchange bonds are sufficient to induce surface spin disorder (see Fig.10) and that the superexchange is very sensitive to bond angles and lengths, which are modified at the surface.

This can have a particularly strong effect on ionic materials, since the exchange interactions are largely antiferromagnetic superexchange interactions. The existence of canted spins was founded experimentally in different ferrimagnetic oxides as NiFe₂O₄, CoFe₂O₄, CuFe₂O₄ by Mössbauer spectroscopy, polarized and inelastic neutron scattering, and ferromagnetic resonance [20–24].

Similar effects were observed in ferromagnetic nanoparticles. For the metal particles, the origin of magnetic ordering is different from superexchange, but the reduction of the effective coordination number for surface atoms leads to similar effects. Ab initio local spin density calculations for Fe, Ni, and Co free surfaces have indicated enhanced moments for the first few atomic layers, by as much as 30% [25, 26].

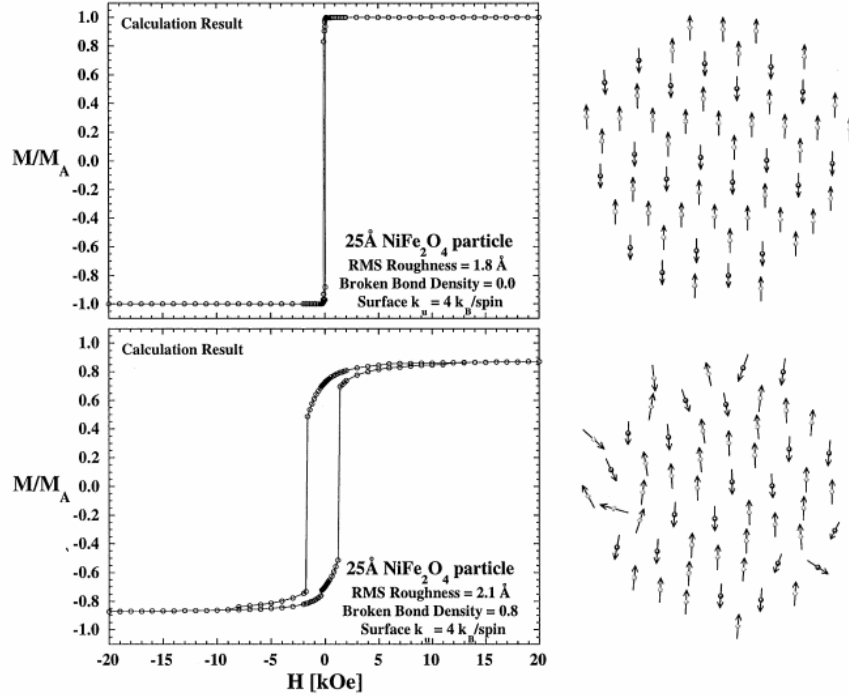


FIG. 10: Calculated hysteresis loops for a 25 Å ferrimagnetic NiFe_2O_4 nanoparticle, with a surface anisotropy of $4k_B/\text{spin}$. (a) Particle with no broken bonds and low roughness ($\text{rms} = 1.8 \text{ \AA}$), hence no surface spin disorder. (b) Particle broken bond density 0.8 and higher roughness ($\text{rms} = 2.1 \text{ \AA}$), hence significant surface spin disorder. Different colors of spots represent the magnetic sublattices (called A and B) separated by oxygen atoms. Taken from [19].

The theoretical explanation was given by Liu [25], where the effects of the local environment on the electronic structure and magnetic moments of Fe, Co and Ni were studied by confining these atoms to sites in various nanosized structures (chains, layers and crystals).

The different symmetry at the surface modifies the electronic structure of the atoms, which gives rise to an enhancement of the magnetic moment per atom, because of the band narrowing (sharper density of states) caused by the lack of atomic orbital overlap at the surface [25].

Experimentally, this was observed by measuring T_B of colloidal Co nanoparticles with the size range from 1.8nm up to 4.4nm. The magnetic moment per particle was calculated from

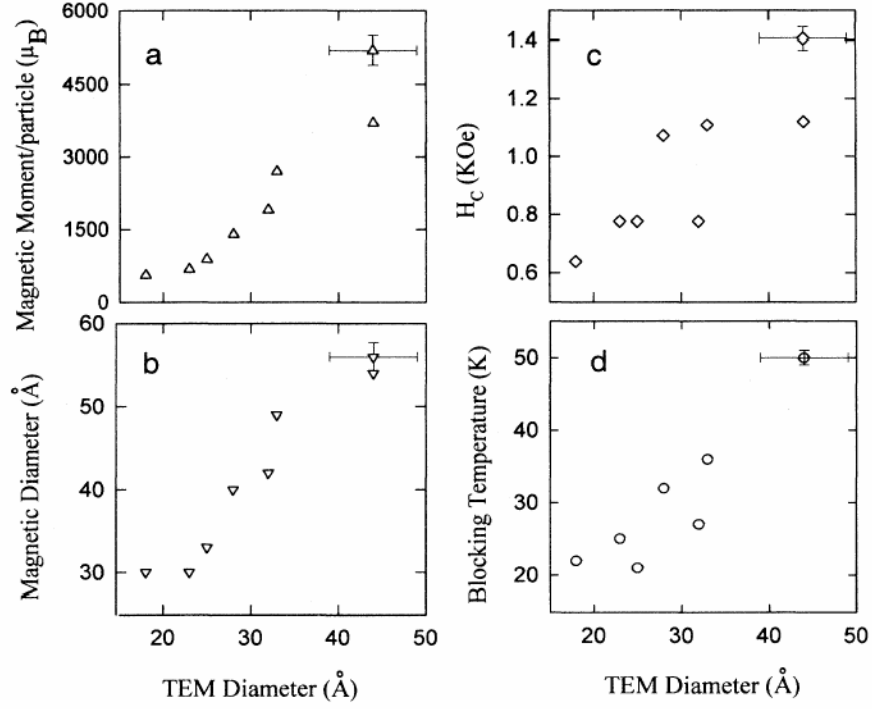


FIG. 11: The magnetic behavior of liquid solution of Co nanoparticles: (a) magnetic moment per particle determined from the susceptibility using eq.(8), (b) magnetic particles diameter obtained from M_S (increase of magnetic size compare to the size obtained with TEM is under discussion) (c) size dependence of coercivity field H_c at 10K, (d) the blocking temperature as a function of particle size. Taken from [27].

the susceptibility measurements above the blocking temperature at low magnetic field [27]:

$$\chi = \frac{\mu M_s}{3k_B T} \quad (8)$$

where, M_s is the saturation magnetization, which was defined from hysteresis loop measurements (not shown). From eq.(8) the magnetic moment per particle was derived as a function of size (Fig.11a). Using the saturation magnetization and μ they derived the magnetic particle size which shown in Fig.11b. The blocking temperature increases as the particles size increases as expected from eq.(6).

In the case of non-interacting nanoparticles eq.(6) can be used to define the anisotropy constant K , where the volume of a particle V is obtained by TEM. Fig.12(a) shows the anisotropy constant of Co nanoparticles as a function of the particle diameter. The

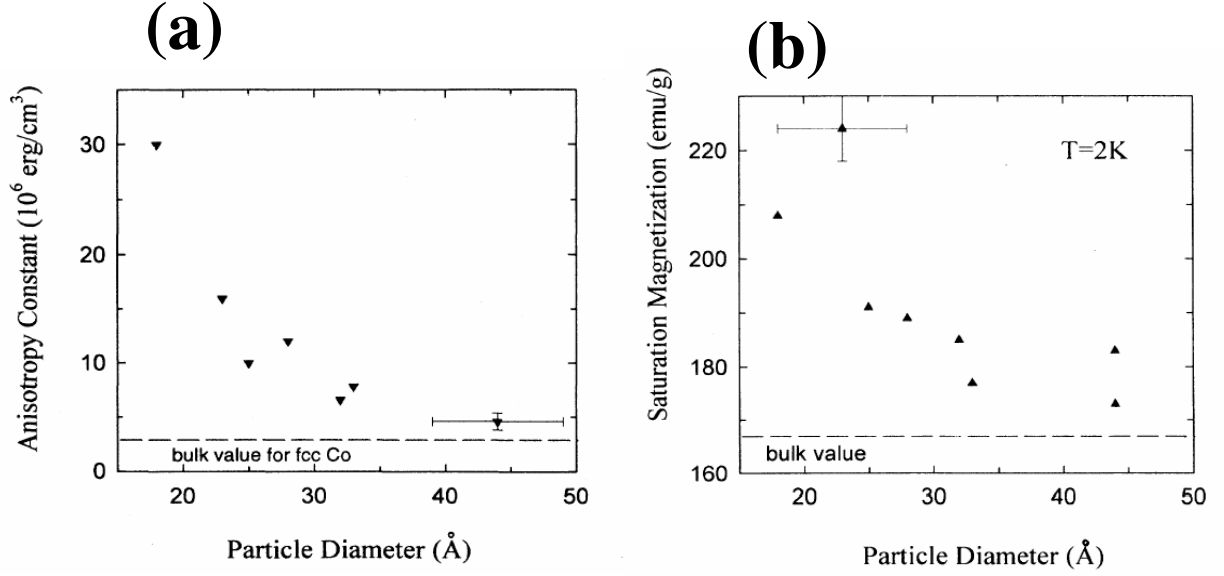


FIG. 12: The magnetic properties of Co nanoparticles: (a) the anisotropy constant as a function of the particle size derived from eq.(6), (b) the saturation magnetization of Co particles at $T = 2\text{K}$ as a function of particle diameter. Taken from [27].

anisotropy constant increases with decreasing particles size. The explanation of this effect is given in terms of a surface anisotropy, due to the large amount of surface atoms for the nanoparticles of 1.8 - 4.4nm in size. These atoms can have a large anisotropy which leads to enhancement of the total anisotropy energy. Effects due to shape anisotropy and oxidation were excluded because of the spherical size of the nanoparticles with a narrow size distribution (obtained by TEM) and the sample preparation (particles were not exposed to air during preparation).

The magnetic measurements show an increase of M_S with decreasing particle size (see Fig.12(b)). Enhanced saturation magnetization implies an enhanced magnetic moment per atom. For this type of Co nanoparticles the enhancement is about 30% compared to bulk Co [27].

The direct consequence of the surface spin canting is a magnetization distribution inside the nanoparticle. Intuitively, it is clear that the magnetization will be reduced from the core to the surface due to the surface spin canting.

Kachkachi et.al., calculated a magnetization profile for $\gamma\text{-Fe}_2\text{O}_3$ nanoparticles with differ-

ent sizes [28]. They used Monte Carlo simulations for a microscopic model for magnetic nanoparticles including exchange and dipolar interactions, and bulk and surface anisotropy, and investigated the thermal and spatial behaviors of the core and surface magnetization of nanoparticles with different sizes, and hence of different surface contributions.

The model is based on the classical anisotropic Dirac-Heisenberg (exchange and dipolar) Hamiltonian, describing the spinel structure of the (spherical or ellipsoidal) ferrimagnetic nanoparticles:

$$H = H_{DH} + H_{dip} \quad (9)$$

where, H_{DH} is the anisotropic Dirac-Heisenberg Hamiltonian taking into account the exchange, anisotropy and Zeeman contributions [28]:

$$H_{DH} = - \sum_{i, \mathbf{n}} \sum_{\alpha, \beta=A, B} J_{\alpha\beta} \mathbf{S}_i^\alpha \cdot \mathbf{S}_{i+\mathbf{n}}^\beta - K \sum_{i=1}^{N_t} (\mathbf{S}_i \cdot \mathbf{e}_i)^2 - (g\mu_B)H \sum_{i=1}^{N_t} \mathbf{S}_i \quad (10)$$

and the pairwise long-range dipolar interactions:

$$H_{dip} = \frac{(g\mu_B)^2}{2} \sum_{i \neq j} \frac{(\mathbf{S}_i \cdot \mathbf{S}_j)R_{ij}^2 - 3(\mathbf{S}_i \cdot \mathbf{R}_{ij}) \cdot (\mathbf{R}_{ij} \cdot \mathbf{S}_j)}{R_{ij}^5} \quad (11)$$

where $J_{\alpha\beta}$ (positive or negative) are the exchange coupling constants between (the $\alpha, \beta = A, B$) nearest neighbors spanned by the unit vector \mathbf{n} , \mathbf{S}_i^α is the (classical) spin vector of the α -th atom at site i , H is the uniform magnetic field applied to all spins (of number N_t) in the particle, $K > 0$ is the anisotropy constant and \mathbf{e}_i is the single-site anisotropy axis, g is the Landé factor, μ_B is the Bohr magneton and \mathbf{R}_{ij} is the vector connecting any two spins on sites i and j of the particle, $R_{ij} = ||\mathbf{R}_{ij}||$. The particle is considered as spinel with two different iron sites, a tetrahedric Fe^{3+} site (denoted by A) and an octahedric Fe^{3+} site (denoted by B) [28].

The model assumes that a particle with the radius in the range of 2-3.5nm is composed of a core containing N_c spins, and a surface shell surrounding it that contains N_s spins, so that the total number of spins $N_t = N_c + N_s$. Thus varying the size of the particle while maintaining the thickness of the surface shell constant ($\sim 0.35\text{nm}$, according to Mössbauer-effect analysis [29]), is equivalent to varying the surface-to-total number of spins, $N_{st} = N_s/N_t$.

The classical Monte Carlo method based on the Metropolis algorithm allows one to calculate the spatial variation of the local magnetization of a spherical nanoparticle (Fig.13), at differ-

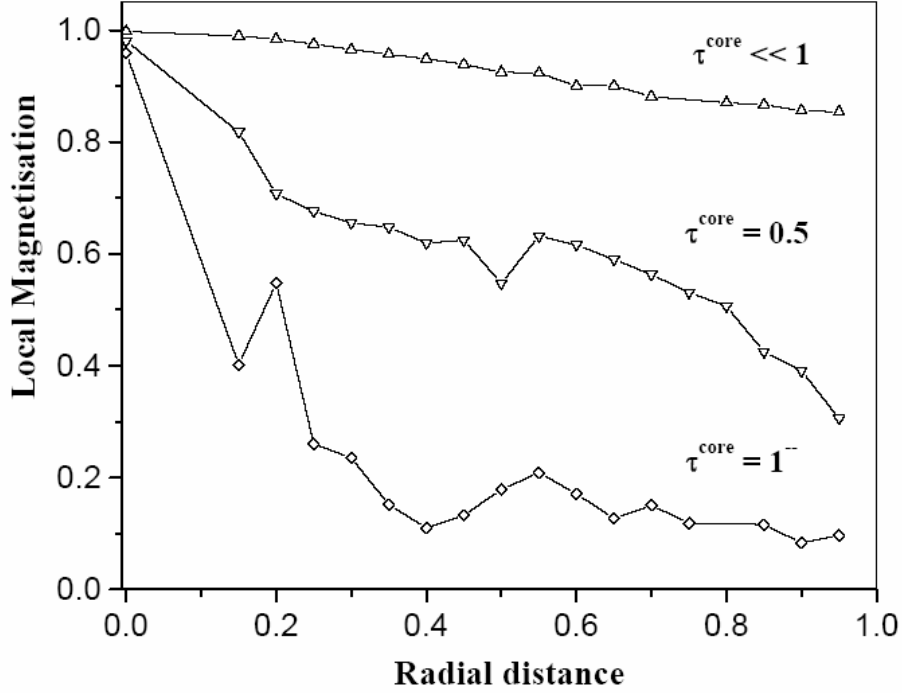


FIG. 13: The spatial evolution of the orientation of the magnetic moment inside the particle as a function of the radial distance, for a spherical nanoparticle of 3140 spins, for different reduced temperatures τ^{core} . Taken from [28].

ent reduced temperatures of the core $\tau^{core} = T/T_c^{core}$, with T_c^{core} is the highest core "critical temperature". It is seen in Fig.13 that the misalignment of spins starts at the surface and gradually propagates into the core. This could be related to the gradual canting of spins confirmed by Mössbauer spectroscopy even at 4.2 K [29].

The magnetization distribution within a magnetic nanoparticle can be studied experimentally using small-angle polarized neutron scattering. The power of this method was demonstrated by Wiedenmann et.al., [30, 31], in the case of dilute and concentrated Co-ferrofluids. The spin canting effect in a magnetization profile was not directly obtained from the simulations of measured data, which is due to the high polydispersity of the Co nanoparticles. Nevertheless, the method is valid while the quality of required samples will be discussed later on.

The Co nanoparticles coated by pure oleoylsarcosine surfactant in fully deuterated toluene were measured by Wiedenmann et.al, [30–32] with polarized (SANS POL) and non-polarized

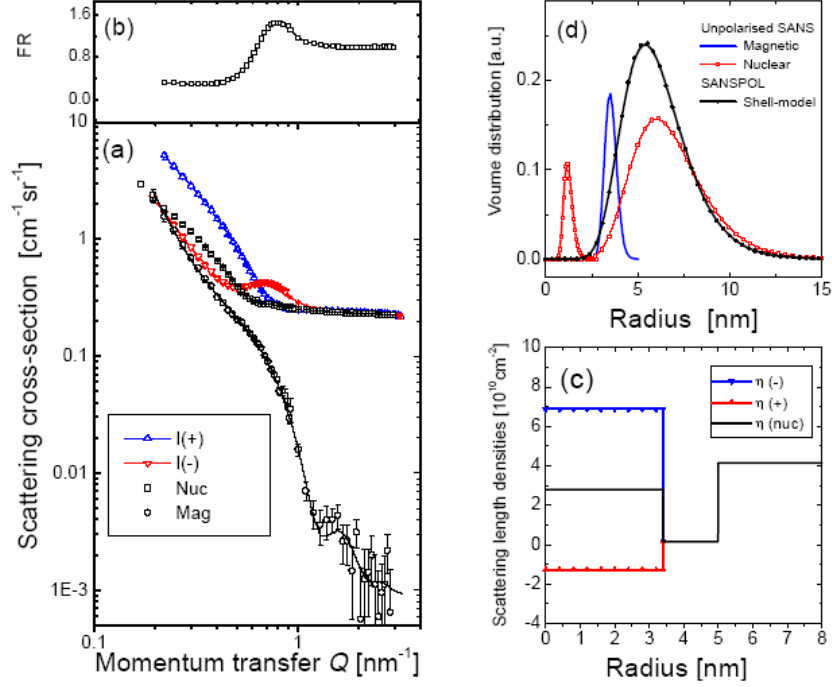


FIG. 14: The measured SANS and SANSPOLE intensities for a Co-ferrofluid. (a) intensities for both polarization states and extracted F_M and F_N form factors (magnetic and nuclear, respectively), (b) flipping ratio. Solid lines: fit using the parameters on the right side. (c) SLD profile, (d) volume distribution for spheres of radius R (non-polarized study) and of composite particles as a function of the outer radius (SANSPOLE). Taken from [31].

(SANS) small-angle neutron scattering. Fig.14 shows the intensities for both polarization states, and derived F_M and F_N form factors (the detailed explanation of the small-angle polarized neutron scattering technique and each of form factors is given in Section 4.3) The fit of the data was done by using eq.(68,69,74) with size distributions and scattering length density (SLD) profiles given in Fig.(14c,d). The following model was applied: a spherical nonmagnetic shell with outer radius R and an inner magnetic sphere (core) with a radius $R' = aR$. The form factor is given by:

$$F_{shell}(Q) = [(\Delta\rho_1 - \Delta\rho_2)f_{sph}(QR') + \Delta\rho_2f_{sph}(QR)]V_p \quad (12)$$

with

$$f_{shp}(x) = 3[\sin x - x \cos x]/x^3 \quad (13)$$

Where, $\Delta\rho_1^{(\pm)} = \rho_{1N} \pm \rho_{1M} - \rho_{matrix}$ is the scattering contrast for the magnetic Co nanopar-

ticle with respect to the matrix, which depends on the polarization state of a neutron. $\Delta\rho_2 = \rho_{2N} - \rho_{matrix}$ is the scattering contrast for a non-magnetic ligand shell with respect to the matrix.

Below the value of $Q = 6.8\text{nm}^{-1}$ the flipping ratio is less than one. It means that the intensities measured for different polarization states (when Q perpendicular to an external magnetic field) are different: $I^+(\perp) > I^-(\perp)$. At the given experimental geometry these intensities can be written as follow:

$$\begin{aligned} I^+(Q, \alpha) &= F_N^2 + (F_M^2 - 2PF_NF_M) \\ I^-(Q, \alpha) &= F_N^2 + (F_M^2 + 2P\varepsilon F_NF_M) \end{aligned} \tag{14}$$

From these formulas it is seen that when $I^+(\perp) > I^-(\perp)$ the magnetic form factor was negative $F_M < 0$ (below $Q = 6.8\text{nm}^{-1}$).

At value of $Q > 1.35\text{nm}^{-1}$ the flipping ratio is unity (i.e. $F_M = 0$) and there is no magnetic contribution to the scattered intensity.

As a result the density profile (Fig.14c) was constructed according to the core-shell model using equations (12) and (13).

In this model, the magnetic SLD is related to the magnetization of the sample, but it is constant inside the Co nanoparticle. In the fitting routine no spin canting effects were taking into account. However, the used model is good enough to describe the data. The observed scattering intensity is smeared out due to the finite resolution of the instrument and a polydispersity of Co nanoparticles. When the size distribution is broad these two effects are difficult to distinguish.

Therefore, in order to probe the spin canting effects with small-angle polarized neutron scattering, highly monodisperse nanoparticles are needed.

3.2. Magnetic properties of an assembly of nanoparticles

When nanoparticles are ordered on a substrate, the additional interactions and effects come into play. An assembly of nanoparticles manifests itself in new properties which are different from a dilute solution of nanoparticles.

We define an ordered array of nanoparticles as a number of particles (with narrow size distribution) deposited on a substrate, and well separated by an average distance D .

The main idea of producing such arrays for fundamental research is to study the inter-particle interactions. It is possible now to produce nanoparticle superlattices with different sizes of the particles and different lattice spacings, in order to study interactions as a function of these length scales. For industrial applications, the aim is to create extremely high density memory devices.

When the magnetic particles are concentrated in solution or arranged in a monolayer on a substrate new effects come into play. Due to a reduced distance between the nanoparticles the following interactions are to be expected [33]: (i) dipole-dipole interactions, which always exist; (ii) exchange interactions through the surface of the particles, which are in close contact; (iii) in granular solids, RKKY interaction through a metallic matrix when particles are also metallic and superexchange interaction when the matrix is insulating.

In contrast to non-interacting magnetic nanoparticles, the magnetic state of an assembly is defined by minimizing the total energy including the interactions. The final magnetic state would be different to that for isolated single nanoparticles. The minimization of the total energy might lead to spin-glass like magnetic behavior of a concentrated solution of nanoparticles.

The effect of inter-particle interactions on the magnetic behavior can be demonstrated in the following example.

The magnetic energy of a particle i , which interacts with its neighbors j is can be written as [34]:

$$E_i = KV_i \sin^2 \theta - \mathbf{M}_i \sum_j K_{ij} \mathbf{M}_j \quad (15)$$

where \mathbf{M}_i and \mathbf{M}_j is the magnetization of the particles i and j , respectively, K_{ij} is the effective exchange coupling constant due to the coupling between surface atoms belonging to neighboring nanoparticles.

If the interactions are negligibly small, then the first term in eq.(15) i.e. the single particle anisotropy dominates. Thus, the energy minimum can be achieved at $\theta = 0$ and $\theta = \pi$. It corresponds to the superparamagnetic relaxation between the two easy directions of magnetization, just as in case of a single nanoparticle (see eq.4). However, if the interactions are strong and the second term is predominant, there might be only one energy minimum for the particle i and the ordered (collective) magnetic state can be obtained [35–37].

The dipole-dipole interactions play a role when particles are brought into close contact. Then a single particle can be approximated as a dipole with moment m and length l , and the magnetic field (H_d) at distance r that it exerts on its neighbor can be calculated:

$$H_d \sim \frac{2mr}{[r^2 - (l/2)^2]_{r \gg l}^2} \longrightarrow \frac{2m}{r^3} \quad (16)$$

for a point along the line of the dipole, or

$$H_d \sim \frac{m}{[r^2 - (l/2)^2]_{r \gg l}^{(3/2)}} \longrightarrow \frac{m}{r^3} \quad (17)$$

for a point in the direction perpendicular to the dipole. Thus, for example, the field created by a Fe square dot of $100 \times 100\text{nm}^2$ and 20nm thickness, is treated as a dipole of length $l = 100\text{nm}$, at distance $r > 1\mu\text{m}$ is negligible ($H < 0.5\text{mT}$). However, as the distance approaches the $< 100\text{nm}$ regime, the field becomes increasingly larger ($H > 15\text{mT}$) [38]. It is important that due to the $1/r^3$ dependence the strength of the dipole-dipole interactions depends not only on the distance between the particles but also on the distance between the edges of the particles.

The straight forward way to examine inter-particle interactions on the microscopic level is to measure the blocking temperature. The inter-particle interactions will change the superparamagnetic relaxation time τ (eq.5). For instance, in the case of dipolar interactions the relaxation time will be defined as (in the case of uniaxial anisotropy) [39]:

$$\tau = \tau_0 \exp \left(\frac{KV}{k_B T} + \frac{E_{dip}}{k_B T} \right) \quad (18)$$

Fig.15 shows the blocking temperature measurements of a liquid solution of Co nanoparticles (5.8nm in diameter) in pyridine and the same particles organized in 2D network by deposition on cleaved graphite. The observed increase in the blocking temperature in case of the 2D network (63 K) compared to isolated particles (58 K) is attributed to collective magnetic properties resulting from inter-particle interactions [40].

An other example of a direct investigation of inter-particle interactions and ordering in an external magnetic field was demonstrated by Wiedenmann [30].

In this work the polarized small-angle neutron scattering (with and without polarization analysis) was applied to concentrated Co ferrofluids.

The small-angle polarized neutron experiment was performed on Co ferrofluids coated with

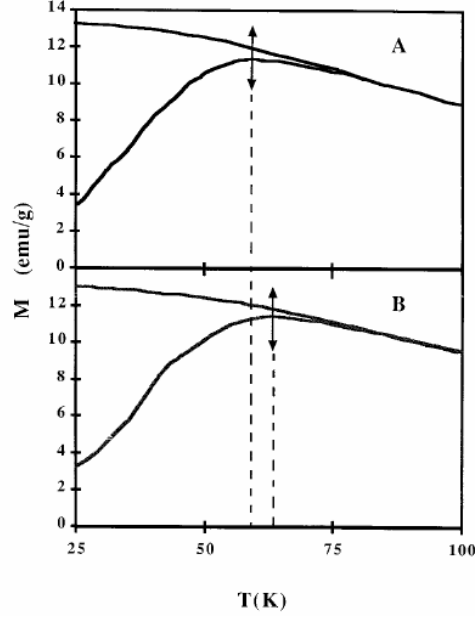


FIG. 15: ZFC/FC curves of Co nanoparticles. The arrow indicates the blocking temperature T_B (a) liquid solution of Co nanoparticles ($T_B = 58\text{K}$), (b) 2D network of Co nanoparticles deposited on cleaved graphite ($T_B = 63\text{K}$). Taken from [40].

surfactant and dispersed in toluene. The size distribution remains the same for all samples while the volume fraction was changed from 0.2 to 6%. The initial polarization of the neutron beam (+) is provided by a transmission-polarizing super-mirror cavity. The polarization of the beam is reversed by a spin-flipper in front of the sample (see Fig.16).

The spin-analysis is based on the very different transmissions $T(+)$ and $T(-)$, of ^3He with nuclear spin polarized anti-parallel (+) and parallel (-) to a guide magnetic field, respectively. The filter cell inside a solenoid providing a longitudinal guide field was housed in a shielding box and placed at 10 cm downstream from the sample exposed to a vertical magnetic field of 0.05 T. With the present set-up two intensities are measured for the incident neutron spin (+) and (-) which are given by [30]:

$$\begin{aligned} I(+)_\text{POLARIS} &= T(+)\text{I}(++) + T(-)\text{I}(-+) \\ I(-)_\text{POLARIS} &= T(+)\text{I}(-+) + T(-)\text{I}(--) \end{aligned} \quad (19)$$

Where, $T(+)$ = 25 – 22% and $T(-)$ = 6 – 8% are the transmission coefficients of the ^3He polarizer for the different polarization states and POLARIS defines the polarized

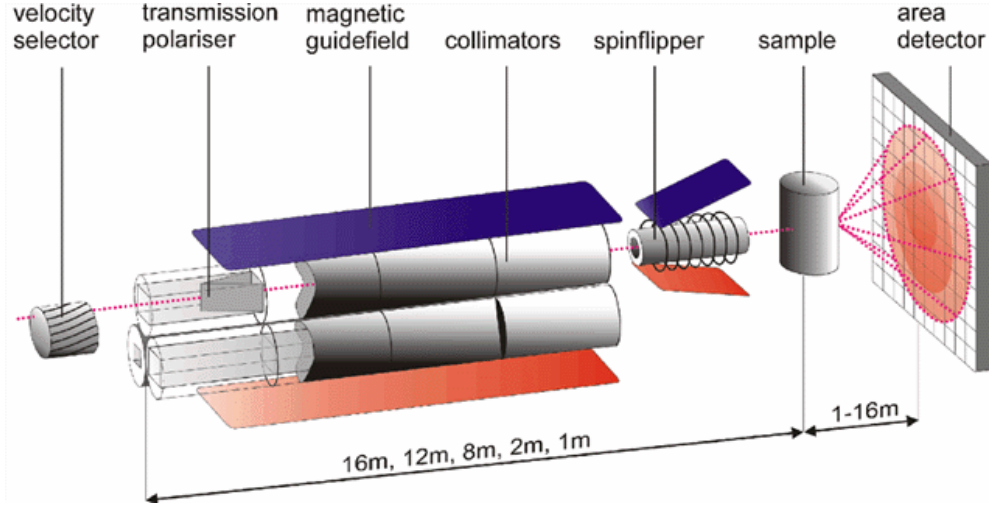


FIG. 16: The sketch of polarized SANS instrument V4 at the BER II reactor of HMI, Berlin. Taken from [47].

small-angle neutron scattering experiment, where the polarization of the scattered neutrons is analyzed (see Section 4.3).

At the field $H=1\text{T}$ perpendicular to the incoming neutron beam all samples with a Co content more than 1% show anisotropic peaks in the 2D detector. The peaks appeared at different values of α angles. When the magnetic field was removed the peaks disappeared. Therefore, the peaks were attributed to a magnetic order induced by the magnetic field.

The structure factor $S(Q, \alpha)$ for a given orientation of α (the angle between the scattering vector \mathbf{Q} and the magnetic field \mathbf{H}) was derived by dividing the measured SANSPOL intensities $I(\pm)(Q, \alpha)$ at given sector angle α by the scattered intensity of the diluted samples where $S(Q, \alpha) = 1$ (Fig.17).

The peak positions correspond to Co nanoparticles arranged in hexagonal planes with magnetizations aligned along the external magnetic field \mathbf{H} (see fig.18). When \mathbf{H} is parallel to the incoming neutrons a diffuse "Debye-Scherrer" ring was observed at Q corresponding to the (001) reflection. That means there is no preferred orientation of the locally ordered Co nanoparticles.

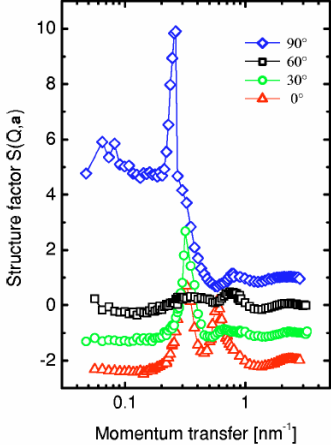


FIG. 17: Anisotropic structure factors for a Co-ferrofluid with 3% concentration for \mathbf{H} perpendicular to the incident neutrons for sectors with a different α angle. Taken from [32].

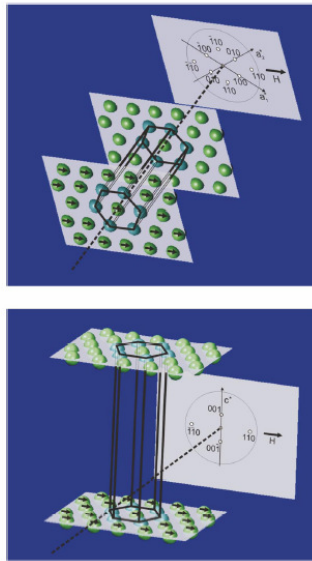


FIG. 18: Schematic representation of two equivalent textures of pseudo-crystalline hexagonal ordering in Co nanoparticles induced by a horizontal magnetic field together with the observed reciprocal lattice points. Taken from [32].

4. EXPERIMENTAL METHODS FOR THE INVESTIGATION OF NANOSCALED MATERIALS

This chapter is dedicated to the experimental methods we used in our work. Here, we will recall some basic aspects of polarized neutron and x-ray scattering. The form factor for spherical particles is derived for small-angle x-ray scattering. Due to the similarity of the basis of small-angle scattering for x-ray and neutrons we will omit the derivation for neutrons. Instead we will discuss the corrections for the differential cross-section in case of neutrons related to the magnetic interactions of neutrons with matter.

4.1. Introduction to polarized neutron scattering

In this section we will highlight some theoretical aspects of neutron scattering (polarized and unpolarized) which are essential for the analysis of the measured data.

The initial quantum state of a neutron incident on the sample is $|\mathbf{k}_i S_i\rangle$, where \mathbf{k}_i is the neutron wave vector and the spin state labels by S . The target (sample) is described by the initial quantum state $|\lambda\rangle$. When the neutron is scattered by the sample the final state of the neutron is $|\mathbf{k}_f S_f\rangle$ and for the sample it is $|\lambda'\rangle$.

In the following text we assume that $S_{i,f}$ are the projections on the z -axis, which is chosen along a magnetic field \mathbf{H}_z , and the subscript symbol z is omitted.

Within the first Born approximation the partial differential cross-section for scattering from the initial state of the system $|\mathbf{k}_i S_i \lambda\rangle$ to the final state $|\mathbf{k}_f S_f \lambda'\rangle$ is given by [41]:

$$\frac{d^2\sigma_s}{d\Omega dE'} = \frac{k_f}{k_i} \left(\frac{m_n}{2\pi\hbar^2} \right) |\langle \mathbf{k}_f S_i \lambda' | V | \mathbf{k}_i S_f \lambda \rangle|^2 \delta(E_\lambda - E_{\lambda'} + E_i - E_f) \quad (20)$$

where, m_n is the neutron mass, E_i and E_f are the initial and final neutron energies, E_λ and $E_{\lambda'}$ are the energies of the target in state $|\lambda\rangle$ and $|\lambda'\rangle$ respectively, V is the interaction potential between the neutron and the sample, $k_{i,f} = |\mathbf{k}_{i,f}|$.

In our work we performed elastic neutron scattering i.e. $k_i = k_f$. Therefore, the scattering cross-section is simplified to

$$\frac{d\sigma}{d\Omega} = \left(\frac{m_n}{2\pi\hbar^2} \right) |\langle \mathbf{k}_f S_f | V | \mathbf{k}_i S_i \rangle|^2 \quad (21)$$

In case of neutron scattering by atoms, two main interactions occur. The first is the short-range nuclear interaction of the neutron with the atomic nucleus (the nuclear

scattering). The second one is the Zeeman interaction of the magnetic moment of the neutron with the magnetic field produced by spin and orbital magnetic moments of the electrons.

4.1.1. Nuclear scattering

The interaction potential of the nuclear scattering is described by the Fermi pseudopotential:

$$V = \frac{2\pi\hbar^2}{m_n} \sum_i b_i \delta(\mathbf{r} - \mathbf{R}_i) \quad (22)$$

where, b_i is the scattering length of atom i , \mathbf{r} is the neutron's position and \mathbf{R}_i is the nucleus position. The scattering amplitude $A(Q)$ is written as

$$A(Q) = \sum_i b_i e^{i\mathbf{Q}\mathbf{R}_i} \quad (23)$$

The differential cross-section is related to the scattering amplitude as follows

$$\frac{d\sigma}{d\Omega} = |A(Q)|^2 \quad (24)$$

For a given element, each isotope will have its own scattering length.

Due to the fact that the nuclear force is dependent on the relative spin orientation, the scattering of a particular nucleus also depends on the relative orientation of the spin of the neutron and of the nucleus. For a nucleus with non-zero spin, b depends on the spin orientation.

These two effects are resulting in a variation of the scattering length from one atomic site to the other. If we assume a random nuclear spin orientation, then the scattering cross-section is written as

$$\frac{d\sigma}{d\Omega} = \left\langle \sum_i b_i e^{i\mathbf{Q}\mathbf{R}_i} \sum_j b_j^* e^{-i\mathbf{Q}\mathbf{R}_j} \right\rangle = \sum_{ij} \langle b_i b_j^* \rangle e^{i\mathbf{Q}(\mathbf{R}_i - \mathbf{R}_j)} \quad (25)$$

where the average is taken over the random distribution.

The individual scattering lengths b_i and b_j are independent and one can write the following conditions:

$$\begin{aligned} i \neq j : \quad & \langle b_i b_j \rangle = \langle b_i \rangle \langle b_j \rangle = \langle b \rangle^2 \\ i = j : \quad & \langle b_i b_j \rangle = \langle b_i \rangle^2 = \langle b^2 \rangle \end{aligned} \quad (26)$$

Which leads to

$$\langle b_i b_j \rangle = \langle b \rangle^2 + \delta_{ij} (\langle b^2 \rangle - \langle b \rangle^2) \quad (27)$$

Therefore, after performing the summation over j , the cross-section will separate into two parts:

$$\frac{d\sigma}{d\Omega} = \langle b \rangle^2 \left| \sum_i e^{i\mathbf{Q}\mathbf{R}_i} \right|^2 + N (\langle b^2 \rangle - \langle b \rangle^2) \quad (28)$$

where, N is the number of scattering nuclei. The first of these terms is the coherent term and the second is the incoherent. The coherent scattering contains all information on the scattering system's cooperative properties. It arises from the average scattering potential experienced by the neutron, i.e. all nuclei scatter with the same coherent scattering length $\langle b \rangle$. Deviations from this average potential are randomly distributed and produce a cross-section which is isotropic for elastic scattering [42].

4.1.2. Magnetic scattering

The magnetic interaction potential can be derived as follows: a neutron has a magnetic moment $\boldsymbol{\mu}_n$ which interacts with the magnetic field of electrons caused by the spin and orbital momentum. Therefore, this magnetic field \mathbf{B}_e can be written as

$$\mathbf{B}_e = \mathbf{B}_{spin} + \mathbf{B}_{orbital} \quad (29)$$

The interaction potential in case of the magnetic scattering is equal to

$$\mathbf{V}_m = -\boldsymbol{\mu}_n \cdot \mathbf{B}_e \quad (30)$$

Using this potential, one can obtain the scattering amplitude for magnetic scattering [43]:

$$A(\mathbf{Q}) = \frac{-\gamma_n r_0}{2\mu_B} \langle S_f | \underline{\sigma}_\alpha | S_i \rangle \mathbf{M}_{\perp\alpha}(\mathbf{Q}) \quad (31)$$

Here, $\mathbf{M}_{\perp}(\mathbf{Q})$ is the component of the Fourier transform of the sample magnetization which is perpendicular to the scattering vector \mathbf{Q} , and only this component contributes to the magnetic scattering, $\gamma_n = -1.913\mu_N$ denotes the magnetic dipole momentum of the

neutron expressed in nuclear magnetons $\mu_N = 5.051 \cdot 10^{-27} J/T$ and r_0 is the classical electron radius. Symbols $\underline{\sigma}_\alpha$ defines the Pauli spin matrices:

$$\underline{\sigma}_x = \begin{pmatrix} 0 & 1 \\ 1 & 0 \end{pmatrix}; \underline{\sigma}_y = \begin{pmatrix} 0 & -i \\ i & 0 \end{pmatrix}; \underline{\sigma}_z = \begin{pmatrix} 1 & 0 \\ 0 & -1 \end{pmatrix} \quad (32)$$

The neutron is a spin-1/2 particle and the behavior of such a particle is described by the two component vector of states:

$$|\psi(\mathbf{r})\rangle = |\psi^+(\mathbf{r})|\chi^+\rangle + |\psi^-(\mathbf{r})|\chi^-\rangle = \begin{pmatrix} \psi^+ \\ \psi^- \end{pmatrix} \quad (33)$$

i.e. by a pair of complex functions $\psi^\pm(\mathbf{r}) = |\psi^\pm| \exp(i\phi_\pm)$, which are the "+" and "-" projections onto two-component basic vectors [44]

$$|\chi^+\rangle = \begin{pmatrix} 1 \\ 0 \end{pmatrix}, |\chi^-\rangle = \begin{pmatrix} 0 \\ 1 \end{pmatrix} \quad (34)$$

In the following text we define $|\chi_\pm\rangle = |\pm\rangle$ for simplicity. These vectors are orthogonal and normalized:

$$\langle +|- \rangle = \langle -|+ \rangle = 0, \quad \langle +|+ \rangle = \langle -|- \rangle = 1 \quad (35)$$

Now it is easy to derive the influence of the spin projection operators on Pauli matrices:

$$\begin{aligned} \underline{\sigma}_x|+\rangle &= |-\rangle & \underline{\sigma}_x|-\rangle &= |+\rangle \\ \underline{\sigma}_y|+\rangle &= i|-\rangle & \underline{\sigma}_y|-\rangle &= -i|+\rangle \\ \underline{\sigma}_z|+\rangle &= |+\rangle & \underline{\sigma}_z|-\rangle &= -|-\rangle \end{aligned} \quad (36)$$

Using equations (35) and (36) one can develop the scattering amplitude $A(Q)$ for different scattering processes:

$$A(\mathbf{Q}) = \frac{-\gamma_n r_0}{2\mu_B} \times \begin{cases} M_{\perp z} & + \rightarrow + \text{ NSF} \\ -M_{\perp z} & - \rightarrow - \text{ NSF} \\ M_{\perp x} - iM_{\perp y} & + \rightarrow - \text{ SF} \\ M_{\perp x} + iM_{\perp y} & - \rightarrow + \text{ SF} \end{cases} \quad (37)$$

where, NSF (non spin-flip scattering) defines the scattering process which conserves the neutron spin and SF (spin-flip scattering) defines the scattering process which reverses the

spin.

It is seen that a magnetization of the sample can reverse the spin of the neutron resulting in SF scattering.

Two rules for the magnetic scattering are derived:

- *Spin-flip* processes are observed for the component of \mathbf{M}_\perp that is perpendicular to the neutron polarization
- *Non-spin flip* processes are observed for the component of \mathbf{M}_\perp that is parallel to the neutron polarization

4.1.3. Nuclear spin-dependent scattering

In this section we consider the non zero spin of the nuclei. In this case the neutron polarization can be parallel or anti-parallel to the nuclear spin \mathbf{I} with different scattering lengths, b_- and b_+ , respectively.

This nuclear spin scattering is treated similar to the magnetic scattering but with different parameters:

$$\mathbf{b} = A + B\hat{S} \cdot \hat{I} \quad (38)$$

where, \hat{I} is the nuclear spin operator and \hat{S} is the neutron spin operator.

$$A = \frac{(I+1)b_+ + Ib_-}{2I+1} \quad B = \frac{b_+ - b_-}{2I+1} \quad (39)$$

The scattering amplitude is derived in the same manner as eq.(37):

$$A(\mathbf{Q}) = \langle S_f | A + B\hat{S} \cdot \hat{I} | S_i \rangle = \begin{cases} A - BI_z & NSF \\ B(I_x - iI_y) & SF \end{cases} \quad (40)$$

The thermal average has to be calculated for the different nuclear spin orientations. The orientation of the nuclear spin is assumed to be random (except for some special cases). This implies:

$$\langle I_x \rangle = \langle I_y \rangle = \langle I_z \rangle = 0 \quad (41)$$

The NSF matrix element therefore is equal to A and the coherent nuclear scattering cross-section is proportional to the coherent length $A = \langle b \rangle = b_{coh}$:

$$\frac{d\sigma}{d\Omega_{coh}}^{NSF} = \langle b^2 \rangle \sum_{r,r'} e^{i\mathbf{Q}(\mathbf{R}' - \mathbf{R})} \quad (42)$$

The NSF matrix element vanishes for incoherent scattering which is proportional to $(\langle b \rangle - \langle b \rangle)$ (see eq.(28)) and we have to consider the following average of the squares of matrix elements

$$\langle I_x^2 \rangle = \langle I_y^2 \rangle = \langle I_z^2 \rangle = \frac{1}{3} I(I+1) \quad (43)$$

from eq.(40) one obtains the spin-incoherent scattering per atom:

$$\begin{aligned} \frac{d\sigma}{d\Omega_{spin-incoh}}^{NSF} &= (\langle b^2 \rangle - \langle b \rangle^2)^{NSF} = \frac{1}{3} \langle B^2 I(I+1) \rangle \\ \frac{d\sigma}{d\Omega_{spin-incoh}}^{SF} &= (\langle b^2 \rangle - \langle b \rangle^2)^{SF} = \frac{2}{3} \langle B^2 I(I+1) \rangle \end{aligned} \quad (44)$$

1/3 of the spin-incoherent part of the nuclear scattering is NSF scattering and 2/3 of it is SF scattering independent of the direction of an external guide field \mathbf{H} .

This is the power of the polarization analysis which allows to separate coherent, spin incoherent and magnetic scattering cross-sections.

If one neglects the magnetic scattering, the coherent and spin incoherent scattering cross-sections can be obtained by combining SF and NSF scattering [43]:

$$\begin{aligned} \frac{d\sigma}{d\Omega_{coh}} &= \frac{d\sigma}{d\Omega}^{NSF} - \frac{1}{2} \frac{d\sigma}{d\Omega}^{SF} \\ \frac{d\sigma}{d\Omega_{incoh}} &= \frac{3}{2} \frac{d\sigma}{d\Omega}^{SF} \end{aligned} \quad (45)$$

4.1.4. Rules of separation

When the total scattering cross-section involves magnetic scattering, a magnetic field variation is needed (perpendicular and parallel to \mathbf{Q}) in order to separate the magnetic part. The scattering cross-sections obtained by a magnetic field variation are listed in the following Table:

field/polarization	SF intensities	NSF intensities
$\mathbf{H} \parallel \mathbf{Q}$	$\sigma_{mag} + \frac{2}{3}\sigma_{inc} + \sigma_{bg}$	$\sigma_{coh} + 0 \cdot \sigma_{mag} + \frac{1}{3}\sigma_{inc} + \sigma_{bg}$
$\mathbf{H} \perp \mathbf{Q}$	$\frac{1}{2}\sigma_{mag} + \frac{2}{3}\sigma_{inc} + \sigma_{bg}$	$\sigma_{coh} + \frac{1}{2}\sigma_{mag} + \frac{1}{3}\sigma_{inc} + \sigma_{bg}$

Based on the table one can obtain the magnetic cross-section as

$$\frac{d\sigma}{d\Omega_{mag}} = 2 \left(\left. \frac{d\sigma^{NSF}}{d\Omega} \right|_{\perp} - \left. \frac{d\sigma^{NSF}}{d\Omega} \right|_{\parallel} \right) = 2 \left(\left. \frac{d\sigma^{SF}}{d\Omega} \right|_{\parallel} - \left. \frac{d\sigma^{SF}}{d\Omega} \right|_{\perp} \right) \quad (46)$$

where, symbols \perp and \parallel denote the cross-sections measured at $\mathbf{H} \perp \mathbf{Q}$ and $\mathbf{H} \parallel \mathbf{Q}$, respectively.

All nuclear scattering contributions and the background cancel in the differences, if they are independent of the magnetic field. An advantage of this separation is that it eliminates a background which comes from the sample environment and from neighbor instruments and has no analytical expression. When the magnetic cross-section is large compared with $\sigma_{inc} + \sigma_{bg}$, it is enough to measure SF data [45].

4.2. Structural properties by small-angle x-ray scattering

Here, we will give an introduction to the basics of a small-angle scattering experiment. At first, we describe what kind of information about the sample can be obtained in terms of the scattering cross-section. Then, we will explain the meaning of form and structure factors. We recall some aspects of the derivation of the cross-section, since they are common for x-rays and neutrons.

The sketch of a typical small-angle scattering experiment is shown in Fig.19. A collimated beam of radiation (x-rays or neutrons) with wavelength λ_i and corresponding energy E_i is incident on a sample of thickness d . Most of the incident radiation is transmitted through the sample without any further interaction and some small part of the incident beam might be absorbed. Only a certain fraction of the incident beam is interacting with the sample and scattered at an angle $2\theta > 0$. The scattered intensity is measured as a function of the momentum transfer $Q = |\mathbf{Q}| = (4\pi/\lambda) \sin \theta$. In the following text we focus on static experiments where an energy transfer can be neglected and experiments at small scattering angles ($2\theta < 10^\circ$), i.e. the case of the elastic small angle scattering [46].

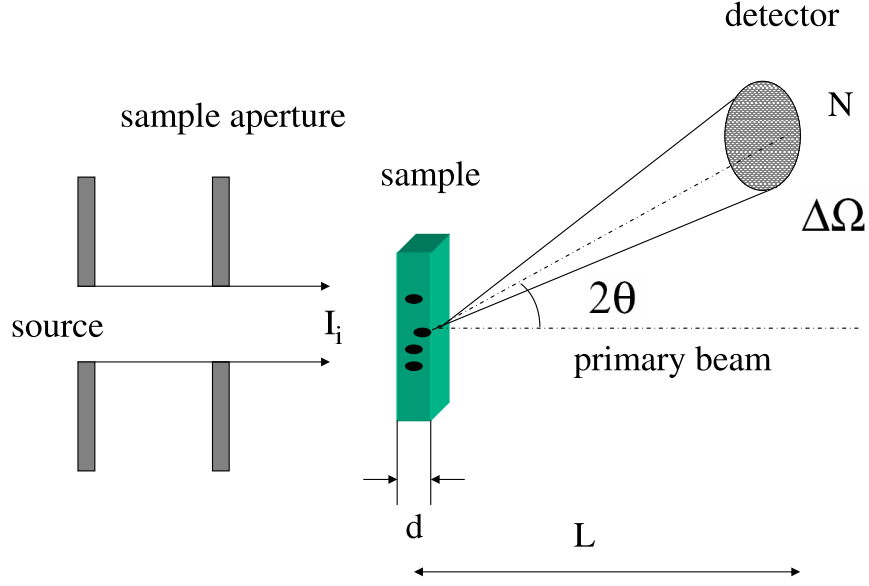


FIG. 19: The sketch of the typical small-angle scattering experiment. The scale is exaggerated for visualization.

The comparison of the incident intensity I_i and the intensity of scattered radiation by the sample I_f measured at an angle 2θ and a distance L on a detector area $A_{det} = \Delta\Omega L^2$ is the aim of the experiment. The ratio of both intensities is called differential scattering cross-section

$$\frac{d\sigma}{d\Omega} = I_f L^2 / I_i \quad (47)$$

where, N is the number of photons (or neutrons) per second scattered into the solid angle element $\Delta\Omega$

Usually, the differential scattering cross-section per unit sample volume is used:

$$\frac{d\Sigma}{d\Omega} = \frac{1}{V} \left(\frac{d\sigma}{d\Omega} \right) \quad (48)$$

where V is the sample volume.

$d\Sigma/d\Omega$ is the quantitative representation of the interaction radiation with a sample and contains all information on the structure and interactions within the sample.

Let us describe the scattering from an assembly of N atoms at individual positions \mathbf{r}_i . The scattering of radiation in this case is the interference of the waves scattered from an atom i at position \mathbf{r}_i with an amplitude A_i . The total scattering can be written as the sum of N wave functions with the amplitude A_i (Born approximation):

$$A(\mathbf{Q}) \sim \sum_N b_i e^{-i\mathbf{Q}\mathbf{r}_i} \quad (49)$$

where, b_i is a parameter describing the fraction of radiation scattered by atom i .

For small-angle scattering, the observed length scale is much larger than inter-atomic distances. Therefore, we can replace the sum by the integration over the sample volume:

$$A(\mathbf{Q}) \sim \int_V \rho(\mathbf{r}) e^{-i\mathbf{Q}\mathbf{r}} d\mathbf{r} \quad (50)$$

where, $\rho(\mathbf{r}) = \sum_i b_i/V$ is the scattering density distribution. For neutrons, ρ depends on the SLD, for x-rays, ρ depends on the electron density. The calculations of the contrast for x-ray and neutrons are given in Appendix A.

The cross-section depends on a square of the scattering amplitude:

$$\frac{d\sigma}{d\Omega}(Q) = |A(\mathbf{Q})|^2 = \left| \int_V \rho(\mathbf{r}) e^{-i\mathbf{Q}\mathbf{r}} d\mathbf{r} \right|^2 \quad (51)$$

Now we consider the system with total volume V composed of two phases only, one with SLD ρ_p (nanoparticles) and occupying the volume V_{all} , and the other with ρ_{sol} (solvent) and the volume V_{sol} (total volume of the system is $V = V_{all} + V_{sol}$). Then the cross-section can be rewritten for a two phase system:

$$\frac{d\sigma}{d\Omega}(Q) = \left| \int_{V_{all}} \rho_p e^{-i\mathbf{Q}\mathbf{r}} d\mathbf{r} + \int_{V_{sol}} \rho_{sol} e^{-i\mathbf{Q}\mathbf{r}} d\mathbf{r} \right|^2 \quad (52)$$

We would like to transform an integral to the particle volume only

$$\frac{d\sigma}{d\Omega}(Q) = \left| \int_{V_{all}} \rho_p e^{-i\mathbf{Q}\mathbf{r}} d\mathbf{r} + \rho_{sol} \left[\int_V e^{-i\mathbf{Q}\mathbf{r}} d\mathbf{r} - \int_{V_{all}} e^{-i\mathbf{Q}\mathbf{r}} d\mathbf{r} \right] \right|^2 \quad (53)$$

it can be rearranged as

$$\frac{d\sigma}{d\Omega}(Q) = \left| \int_{V_{all}} (\rho_p - \rho_{sol}) e^{-i\mathbf{Q}\mathbf{r}} d\mathbf{r} + (2\pi)^3 \rho_{sol} \delta(\mathbf{Q}) \right|^2 \quad (54)$$

We consider the case, when the system contains N identical nanoparticles with the same shape and the same SLD. Therefore, at $Q \neq 0$ the differential cross-section for nanoparticles dispersed in a solvent is written as

$$\frac{d\Sigma}{d\Omega}(Q) = n_p \Delta\rho^2 V_p^2 \left| \frac{1}{V_p} \int_{V_p} e^{-i\mathbf{Q}\mathbf{r}} d\mathbf{r} \right|^2 \quad (55)$$

where, $n_p = N/V$ is the number of particles per unit volume, $\Delta\rho$ is the scattering density contrast, and V_p is the volume of a particle.

In order to obtain the differential cross-section in absolute units it should be multiplied by factor C' . It is the calibration factor for the given experimental configuration and contains instrumental parameters (sample-to-detector distance L , incident beam intensity I_i and area of the sample diaphragm). The integral term in eq.(55) contains an information about the shape of the particles.

One can see that the differential cross-section is proportional to the square of the density contrast of scatters and gives an access to intrinsic properties of scatters (in our case nanoparticles). For polarized neutron scattering, the contrast becomes more complicated and allows one to describe the magnetic properties of magnetic nanoparticles (this will be discussed in the following section).

If we assume that the nanoparticles have a spherical shape and then integrate eq.(55) over the particle volume, then:

$$\frac{d\Sigma}{d\Omega}(Q) = n_p F^2(QR) = n_p \Delta\rho^2 V_p^2 f^2(QR) \quad (56)$$

where, $F(QR) = \Delta\rho V_p f(QR)$ is the form factor related to the structure of the single particles. For the homogeneous spherical particles $f(QR) = 3[\sin QR - QR \cos QR]/(QR)^3$. In general, the differential cross-section includes the information not only about the chemical and geometrical properties of an individual nanoparticle, but also about the interactions between them. The interactions are described by the structure factor $S(Q)$ and modify eq.(56) in the following manner:

$$\frac{d\Sigma}{d\Omega}(Q) = n_p F^2(QR) S(Q) \quad (57)$$

Therefore, dilute solutions with non-interacting nanoparticles present a special case when $S(Q) = 1$. Usually, the structure factor influences the low Q region of a scattering curve. The analytical description of the structure factor is complicated, however it can be obtained experimentally by comparing the scattering cross-sections of the dilute solution of

the nanoparticles ($S(Q)=1$) and the concentrated one ($S(Q) \neq 1$):

$$S(Q) = n_p^{conc} \left(\frac{d\Sigma}{d\Omega} \right)_{conc} / n_p^{dil} \left(\frac{d\Sigma}{d\Omega} \right)_{dil} \quad (58)$$

In case of spherical nanoparticles with no interactions, the small-angle scattering curve has a form as it is shown in Fig.47. At low Q it is flat and at higher Q it is decreasing as Q^{-4} (Porod regime) with minima corresponding to the averaged particle size.

The situation became more complicated in case of the core-shell model, when the core and shell have a different contrast with respect to the solution. In the model we assume a spherical core with radius R_c surrounded by the spherical shell with thickness δ and corresponding SLDs ρ_c and ρ_s . For the sake of simplicity we derive a form factor $F_{core-shell}(QR)$, instead of deriving it for the differential scattering cross-section (eq.55).

In order to take into account different contrasts contributing to the cross-section, the form factor in eq.(56) is rewritten:

$$F_{core-shell}(QR) = (\rho_c - \rho_{sol})V_c f(QR_c) + (\rho_s - \rho_{sol})V_s f(QR_s) \quad (59)$$

Now we use the same method of derivation as for the general case of a two phase system (see eq.53)

$$F_{core-shell}(QR) = (\rho_c - \rho_{sol})V_c f(QR_c) + (\rho_s - \rho_{sol}) [V_t f(QR_t) - V_c f(QR_c)] \quad (60)$$

and finally,

$$F_{core-shell}(QR) = (\rho_c - \rho_s)V_c f(QR_c) + (\rho_s - \rho_{sol})V_t f(QR_t) \quad (61)$$

where, $\rho_c - \rho_s, \rho_s - \rho_{sol}$ are the core/shell and shell/solvent contrasts, respectively. $V_c, V_s, V_t = V_c + V_s$ are the volumes of the core, shell and the total volume of a particle, with radius R_c, R_s and $R_t = R_s = R_c + \delta_{shell}$, respectively.

In reality the scatters can have a size distribution which will influence the scattering curve. The colloidal nanoparticles in microemulsion often show significant polydispersity. This is a result of thermodynamical equilibrium, where the system free energy is minimized. To take into account the polydispersity of nanoparticles one should rewrite eq.(57) as follows

$$\frac{d\Sigma}{d\Omega}(Q) = n_p \int_0^\infty D(R) F^2(QR) S(Q) dR \quad (62)$$

where, $D(R)$ is the size distribution function. In our simulations we always assume the log-normal distribution

$$D(R) = \frac{1}{\sqrt{2\pi}\sigma R} \exp\left(-\frac{(\ln R - \ln R_{av})^2}{2\sigma^2}\right) \quad (63)$$

with σ is the standard size deviation and R_{av} is the averaged particle radius.

The polydispersity effect plays an important role in analyzing the small-angle scattering data. The effect manifests itself in a smearing out of the intensity minima as it is shown in Fig.47. It is similar to the smearing due to the finite resolution of the instrument, thus it is important to distinguish between these two effects (see Section 8.3).

We can conclude that from the fit of the small-angle scattering curve the averaged size, size distribution and chemical properties of nanoparticles can be deduced.

4.3. Magnetic and structural properties by small-angle polarized neutron scattering

4.3.1. Non-interacting nanoparticles

Here, we will focus mainly on the theoretical basis of polarized SANS for a liquid solution of Co nanoparticles coated with a ligand shell.

For polarized neutrons where the neutron spins are aligned antiparallel (denoted by $+$) or parallel ($-$) to a preferred orientation $z \parallel \mathbf{H}$ (where \mathbf{H} is the magnetic field vector), four types of scattering processes have to be distinguished, two which conserve the neutron spin (NSF) and two with reversal of the spin (SF)[31].

For the case when the magnetizations of Co nanoparticles and the neutron polarization are directed along an external magnetic field, the intensities for different polarization states of incident neutrons can be written as a function of Q :

$$\begin{aligned} I^+(Q, \alpha) &= F_N^2 + (F_M^2 - 2PF_N F_M) \sin^2 \alpha \\ I^-(Q, \alpha) &= F_N^2 + (F_M^2 + 2P\varepsilon F_N F_M) \sin^2 \alpha \end{aligned} \quad (64)$$

where, α is the angle between scattering vector \mathbf{Q} and magnetic field \mathbf{H} , $P = \frac{n^+ - n^-}{n^+ + n^-}$ is the polarization (n^-, n^+ is the number of neutrons parallel and antiparallel to the field to

\mathbf{H} , respectively), ε is the spin flipper efficiency, F_M , F_N are the magnetic and nuclear form factors, respectively.

The form factors F_M and F_N for a particle of species j embedded in a homogeneous matrix (or dispersed in solution) are written as:

$$F_j(QR) = \int_{V_{pj}} d\mathbf{r} \Delta\rho_j e^{i\mathbf{Q}\mathbf{r}_j} = \Delta\rho_j V_{pj} f(QR) \quad (65)$$

where, $j = N, M$ defines the nuclear and magnetic part, respectively, V_{pj} is the volume of the particle, $f(QR)$ is the form factor which depends on a shape of a particle, $\Delta\rho$ is the difference between the SLD of a particle and the matrix. For the nuclear scattering the SLD is defined as:

$$\rho_N = \sum_i^N b_i^{coh} \frac{DN_A}{M} \quad (66)$$

Here b_i^{coh} is the coherent scattering length of atom i , N is the total number of atoms in the molecule, D is the bulk density, M is the molar mass of component i and N_A is Avogadro's number.

In case of the magnetic scattering:

$$\rho_M = (0.27 \cdot 10^{-12} cm) \frac{\sum_i c_i \mathbf{M}_i^\perp}{\Omega_i} \quad (67)$$

where, \mathbf{M}_i^\perp is the projection of the magnetic moment on a plane perpendicular to \mathbf{Q} . The scattered intensity in case of non-polarized neutrons can be defined as:

$$\frac{1}{2} [I^+(Q, \alpha) + I^-(Q, \alpha)] = I(Q, \alpha)_{non-pol} = F_N^2 + F_M^2 \sin^2 \alpha \quad (68)$$

The magnetic nuclear cross term is then defined as:

$$I^+(Q, \alpha) - I^-(Q, \alpha) = 2P(1 + \varepsilon)F_N F_M \sin^2 \alpha = B_{int}(Q) \sin^2 \alpha \quad (69)$$

were,

$$B_{int}(Q) = 2P(1 + \varepsilon)F_N F_M \quad (70)$$

The new parameter γ is the ratio between magnetic and nuclear form factors:

$$\gamma = \frac{F_M}{F_N} \quad (71)$$

This ratio is directly connected with the intensities in both polarization channels. The flipping ratio is defined as:

$$FR = \frac{I^-(Q, \alpha)}{I^+(Q, \alpha)} = \frac{1 + 2P\varepsilon\gamma + \gamma^2}{1 - 2P\gamma + \gamma^2} \quad (72)$$

The solution of this equation is given by

$$\gamma = B_{int}(Q)/[2A(Q)P(1 + \varepsilon)] \quad (73)$$

The cross-sections for the different polarization states can be rewritten:

$$\frac{d\sigma^\mp}{d\Omega} = A(Q) + B^\mp(Q) \sin^2 \alpha \quad (74)$$

where, $A(Q) = F_N^2$ in case of a complete alignment of all magnetic moments of Co nanoparticles along \mathbf{H} and it is independent of the polarization state, $B^\mp(Q)$ is the anisotropic part and depends on the polarization state of a neutron.

$B^+(Q) = F_M^2 - 2PF_NF_M$ - for neutrons polarized parallel to \mathbf{H} , $B^-(Q) = F_M^2 + 2P\varepsilon F_NF_M$ - for neutrons polarized antiparallel to \mathbf{H} .

When the polarization of the scattered neutrons is not analyzed (denoted here as SANS POL [30, 31]) the nuclear part of the scattering cross-section can be extracted from the intensity of a non-polarized beam (eq.68), at $\alpha = 0$,

$$A(Q) = F_N^2 \quad (75)$$

With $A(Q)$ obtained from the non-polarized scattering experiment at $\alpha = 0$ one can reconstruct the magnetic form factor F_M^2 according to the following formula:

$$F_M^2(Q) = \frac{B_{int}^2(Q)}{4A(Q)P^2(1 + \varepsilon)^2} \quad (76)$$

It is the main feature of SANS POL which allows to separate a weak magnetic scattering from a strong nuclear scattering.

4.3.2. Interacting nanoparticles

Similar to x-ray scattering, the neutron scattered intensity from interacting nanoparticles is written as a function of Q :

$$I(Q) = \sum_j \int_0^\infty n_{pj} F_j^2(QR) D_j(R) S(Q) dR \quad (77)$$

where, $S(Q)$ is the structure factor related to the interparticle interactions, $D_j(R)$ is the particle size distribution function, $F_j(QR)$ is the particle form factor, n_{pj} is the number of particles per unit volume.

At large Q only the form factor contributes to the scattered intensity. In the case of non-interacting (e.g. diluted samples) nanoparticles $S(Q) = 1$.

In case of non perfect alignment of the magnetization of the single domain particle in solution, the structure factor is developed into $S(Q, \alpha)$, where α is the angle between the scattering vector \mathbf{Q} and the magnetic field \mathbf{H} .

For the superparamagnetic Co nanoparticles an orientational distribution as a function of an effective field H_{eff} and temperature can be described by Langevin statistic:

$$L(x) = \frac{\coth x}{x} \quad (78)$$

with

$$x = \frac{M(R)H_{eff}}{k_B T} \quad (79)$$

The total magnetic moment $M(R)$ can be expressed as

$$M(R) = \frac{4\pi R^3 m_o}{3\Omega} \quad (80)$$

where, R is the radius of a particle, m_o is the saturation value of the atomic magnetic moment, Ω is the atomic volume of the particle.

To obtain the scattering cross-section for the interacting nanoparticles one can use a formalism similar to the one derived above. In the general case when the magnetizations of magnetic nanoparticles are not directed along the external magnetic field the scattering cross-section is

$$\frac{d\sigma}{d\Omega_{ij}}(Q, \alpha) = A_{ij}S(Q, \alpha) + B_{ij}F_M^2(Q) \quad (81)$$

where, $i, j = +, -$ defines four different cross-sections for polarized neutrons, $A_{i,j}$, $B_{i,j}$ are the weighting functions which are different for the four scattering processes and depend on the technique used (see Tab.IV).

The cross-sections consist of two parts: $A_{i,j}S(Q, \alpha)$ are the inter-particle correlations of the nuclear or/and magnetic origin, $B_{i,j}F_M^2(Q)$ result from the non-perfect alignment of magnetic nanoparticles along magnetic field.

TABLE IV: Weighting functions A_{ij} and B_{ij} for the scattering contributions of the inter-particle correlations $A_{ij}S(Q)$ and of the moment misalignment $B_{ij}F_M^2$, respectively, with the abbreviations: $a = L(x)/x$ and $b = [L^2(x) - 1 + 3L(x)/x]$, where $L(x)$ is the Langevin function.

The functions presented for three operation modes: SANS - the scattering with unpolarized neutrons, SANSPOL - polarized neutron scattering with no analysis of the polarization of the scattered neutrons, POLARIS - the polarization of the scattered neutrons is analyzed [30]

Process	A_{ij}	B_{ij}	$B_{ij}(H \rightarrow 0)$
POLARIS			
$I(-)$	$[F_M L(x) \sin^2 \alpha + F_N]^2$	$a \sin^2 \alpha - b \sin^4 \alpha$	$1/3 \sin^2 \alpha$
$I(++)$	$[F_M L(x) \sin^2 \alpha - F_N]^2$	$a \sin^2 \alpha - b \sin^4 \alpha$	$1/3 \sin^2 \alpha$
$I(+-), I(-+)$	$[F_M L(x) \sin \alpha \cos \alpha]^2$	$a(2 - \sin^2 \alpha) - b \sin^2 \alpha \cos^2 \alpha$	$1/3(2 - \sin^2 \alpha)$
$I(--) - I(++)$	$F_N F_M L(x) \sin^2 \alpha$	0	0
SANSPOL			
$I(-)$	$[F_M^2 L^2(x) + 2F_M F_N L(x)] \sin^2 \alpha + F_N^2$	$a - b \sin^2 \alpha$	$2/3$
$I(+)$	$[F_M^2 L^2(x) - 2F_M F_N L(x)] \sin^2 \alpha + F_N^2$	$a - b \sin^2 \alpha$	$2/3$
$I(-) - I(+)$	$F_N F_M L(x) \sin^2 \alpha$	0	0
SANS			
$I(Q)$	$F_M^2 L^2(x) \sin^2 \alpha + F_N^2$	$2a - b \sin^2 \alpha$	$2/3$

As it is seen from Tab.IV the SF processes have purely magnetic origin, when NSF have both a magnetic and nuclear origin.

5. CONTRAST VARIATION BY ANOMALOUS X-RAY SCATTERING APPLIED TO INVESTIGATION OF THE INTERFACE MORPHOLOGY IN A GMR FE/CR/FE TRILAYER

In recent years systems displaying the giant magnetoresistance effect (GMR) [3, 48] are in the focus of many research activities. Besides the fundamental interest in the magnetic and transport properties of thin film and nanostructured systems, GMR systems are attractive for many applications [49–51]. There are aspects concerning the GMR effect which are still far from understood. For instance, the dependence of the strength of the GMR effect on interfacial roughnesses is still under debate [52, 53]. It was shown that in an Fe/Cr superlattice, the GMR effect decreases with increasing roughness of the substrate [54], while it maybe enhanced by the presence of Fe/Cr interfacial roughness [55]. In order to confirm some theoretical predictions about the GMR effect [56, 57], exact structural information about every layer and every interface is required.

Surface sensitivity techniques, such as scanning tunneling microscopy (STM) are extremely powerful techniques to determine morphology of surfaces in situ during the film preparation. This has been shown for Fe/Ag interface and for Cr/Fe superlattices by Bürgler [63] and Schmidt [58]. However, as the next layer is deposited, the resulting interface morphology might be different from the morphology of the exposed surface. Moreover, STM probes only smaller sample regions and thus give access only to shorter lateral correlations lengths. To get access to a larger range of correlation length and to buried layer, scattering methods are the method of choice. x-ray and neutron scattering are non-destructive methods which are able to characterize quantitatively the properties of buried layers in superlattices. In previous publications [59–61], the analysis of measured x-ray reflectivity combined with off-specular scattering was introduced. This technique has to be extended for typical GMR multilayers, which consist of transition metal layers with nearly identical SLDs. For example in Fe/Cr/Fe GMR trilayers, Fe and Cr have nearly the same electron density and thus the interface between Fe and Cr is nearly invisible to conventional x-ray reflectometry. To overcome this problem we used the advantage of anomalous x-ray scattering. We were able to achieve the maximum contrast between Fe and Cr as well as the lowest one using two different photon energies.

In what follows, we will briefly outline the theoretical model used for the simulations, describe the fitting procedure to the measured data and discuss the quantitative description of the trilayer. The application of the outlined method will enable one to obtain a better understanding of the relation between morphology and functionality in similar spintronic devices.

5.1. Sample preparation

The sample under investigation is a typical GMR system - two ferromagnetic iron layers separated by a non-ferromagnetic chromium spacer layer. The nominal thickness of the Cr spacer layer is 11Å, which is appropriate to give rise to antiferromagnetic coupling between two Fe layers. The sample was produced in a ultra high vacuum molecular beam epitaxy (MBE) machine [62]. We followed the growing procedure of Fe/Cr/Fe layers on a GaAs (001) single crystal substrate with Ag buffer given in [63]. An overview of the sample preparation parameters is given in Tab.V. It is important that the roughness of the epitaxially grown layer depends on the deposition temperature [63, 64].

The nominal thicknesses were obtained with a quartz microbalance with uncertainties in the range of 5 - 10%.

After deposition of each layer, low-energy electron diffraction (LEED) patterns have been taken, in order to prove the single crystalline nature of every layer. While the morphology of a surface can be changed as it becomes an interface during deposition of the next layer, we expect the layers to remain single crystalline.

5.2. Experiment

The anomalous x-ray scattering measurements were performed at the beamline C1 in HASYLAB at two photon energies $E_1=5985\text{eV}$ and $E_2=6940\text{eV}$. At $E_2=6940\text{eV}$ iron and chromium display no contrast (see Fig.22(b)). The experimental details are the following: the sample size was $10\times 10\text{ mm}^2$, the sample-to-detector distance 1400 mm, the beam size at the sample position 0.47 mm and the opening of the slit in front of the NaI scintillation detector was 1 mm.

Close to the absorption K-edge of Cr ($E_{Cr}^K=5989\text{eV}$), the low electron density contrast be-

TABLE V: Sample preparation parameters. The layers are in the order of the deposition. d is the nominal thickness, T is the deposition temperature, r is the growth rate, LS is the lattice structure.

Layers	d[Å]	T[° C]	r [Å/s]	LS
GaAs	bulk	annealed at 640°C	-	-
Fe	10	120	0.1	bcc
Ag	1500	120	1.6	fcc
Fe	150	20	0.2	bcc
Cr	11	20	0.1	bcc
Fe	150	20	0.2	bcc

tween Fe and Cr is enhanced due to anomalous scattering (Fig.22(a)). For both energies a set of different measurements was performed. First, we measured the reflectivity ($\alpha_i = \alpha_f$) and longitudinal diffuse ($\alpha_i = \alpha_f + 0.05^\circ$) scans (Fig.23), then a number of omega scans ($\alpha_i + \alpha_f = 2\theta$, $2\theta = \text{const}$) was performed (Fig.24).

The geometry of the scattering experiment is shown in Fig.20. The scattering vector $\mathbf{q} = \mathbf{k}_f - \mathbf{k}_i$ depends on wave vectors of incident and scattered waves \mathbf{k}_i and \mathbf{k}_f , respectively. The projections of the \mathbf{q} vector on the x and z directions are:

$$q_x = \frac{2\pi}{\lambda} (\cos \alpha_f - \cos \alpha_i) \quad (82)$$

$$q_z = \frac{2\pi}{\lambda} (\sin \alpha_f + \sin \alpha_i) \quad (83)$$

where λ is x-ray wave length and α_i and α_f are the angles of incident and scattered photons, respectively. The scan conditions are shown in Fig.21.

The overview over the diffuse scattering measurements is presented in Fig.25., where the intensity of the scattered photons is plotted as a function of incident and outgoing angles of the photons.

5.3. Contrast variation

The refractive index for x-rays is defined as:

$$n = 1 - \delta + i\beta \quad (84)$$

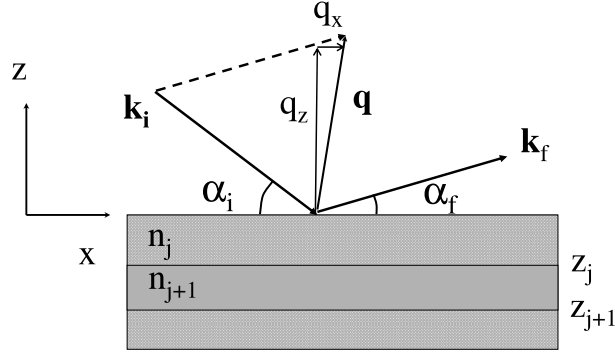


FIG. 20: The scattering geometry of the experiment.

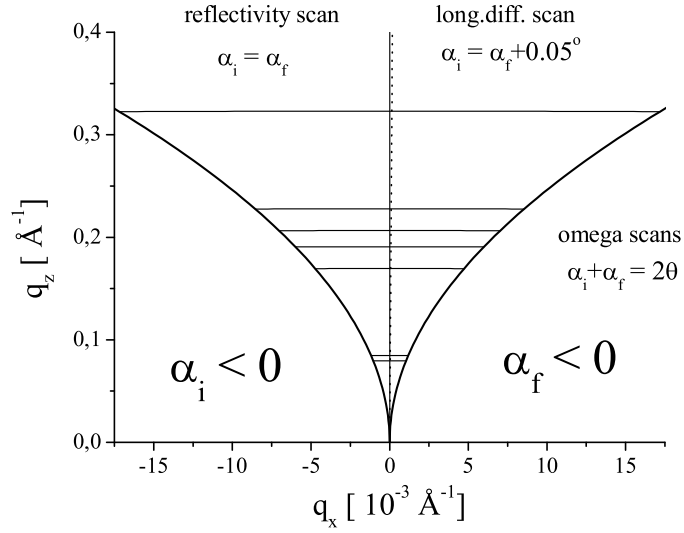


FIG. 21: Scans in (q_x, q_z) space for the energy $E_1=5985\text{eV}$. The vertical solid line is the reflectivity scan ($\alpha_i = \alpha_f$), the dashed line is the longitudinal diffuse scan ($\alpha_i = \alpha_f + 0.05^\circ$) and the solid horizontal lines are omega scans ($\alpha_i + \alpha_f = 2\theta$) at 2θ values listed in Fig.24(a). The regions below solid curved lines are not assessable with the experimental setup we used.

where, the dispersion δ is [65]

$$\delta = \frac{r_0}{2\pi} \lambda^2 N_A \sum_i \frac{\rho_i}{A_i} (Z_i + f'_i) \quad (85)$$

and the absorption β is

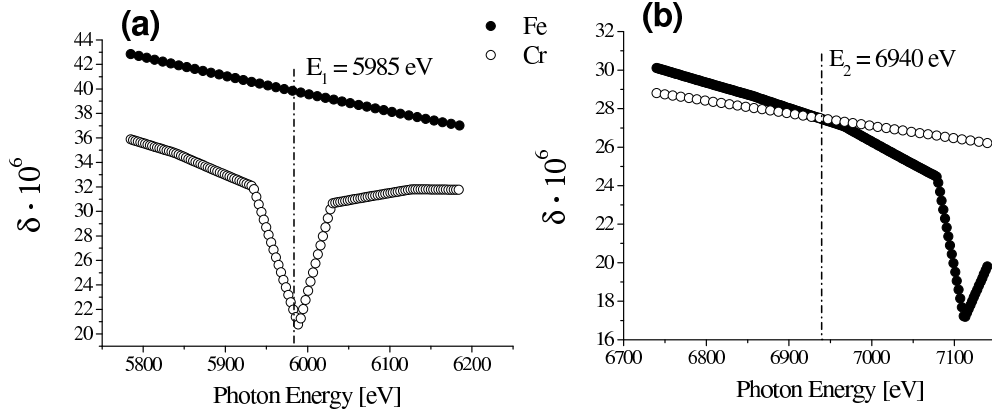


FIG. 22: The dispersion δ at: (a) - $E_1=5985$ eV - Cr absorption K-edge (b) - $E_2=6940$ eV [67].

$$\beta = \frac{r_0}{2\pi} \lambda^2 N_A \sum_i \frac{\rho_i}{A_i} f_i'' \quad (86)$$

where the summation is over all the constituent elements i ; r_0 is the classical electron radius, N_A is the Avogadro's number, ρ is the mass density, A and Z are atomic weight and number, respectively, f' and f'' are the anomalous scattering factors.

The values of f' and f'' change most at the absorption edge of the magnetic elements, therefore the contrast is enhanced.

5.4. Specular reflectivity

For the calculation of x-ray reflectivity a recursion Parratt formalism [70] is developed for the ratio X_j of reflected and transmitted amplitude in the medium between interfaces j and $j + 1$. Taking into account the boundary conditions for the tangential components of the electric and magnetic fields, one can obtain

$$X_j = \frac{R_j}{T_j} = e^{-2ik_{z,j}z_j} \frac{r_{j,j+1} + X_{j+1}e^{2ik_{z,j+1}z_j}}{1 + r_{j,j+1}X_{j+1}e^{2ik_{z,j+1}z_j}} \quad (87)$$

with Frensel coefficients

$$r_{j,j+1} = \frac{k_{z,j} - k_{z,j+1}}{k_{z,j} + k_{z,j+1}} \quad (88)$$

The wave-vector component perpendicular to the layer surface inside the respective

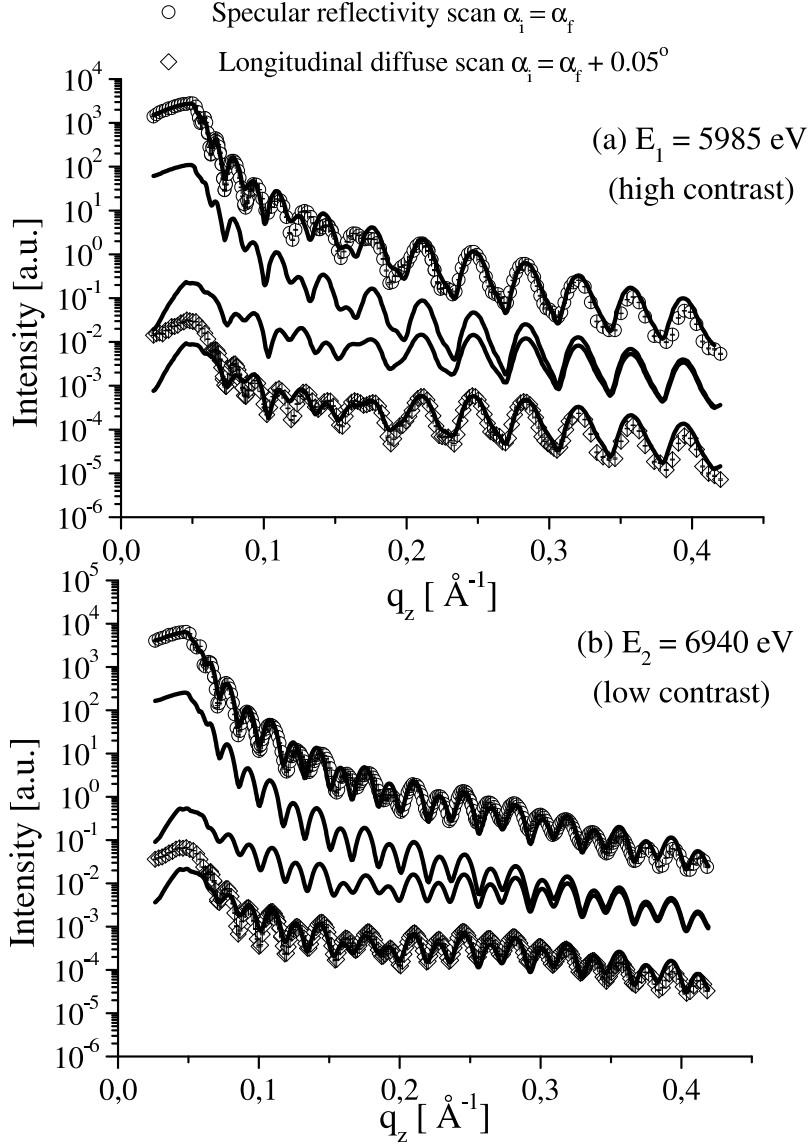


FIG. 23: Intensity measured at the specular position and longitudinal diffuse scans at: (a) - $E_1=5898\text{eV}$ (b) - $E_2=6940\text{eV}$. Open symbols are data points, the solid lines show the best fit obtained from a simultaneous refinement of all data. The calculated values for the specular intensity are a sum of the diffuse scattering for $q_x = 0$ calculated within DWBA and the true specular reflectivity calculated within a Parratt formalism.

For visualization the experimental data was displaced by factor 25 for specular reflectivity and by factor 1/25 for the longitudinal diffuse scan, with corresponding fitting curves. The crossing solid lines in the center of every plot are the fits of the original data with no displacement.

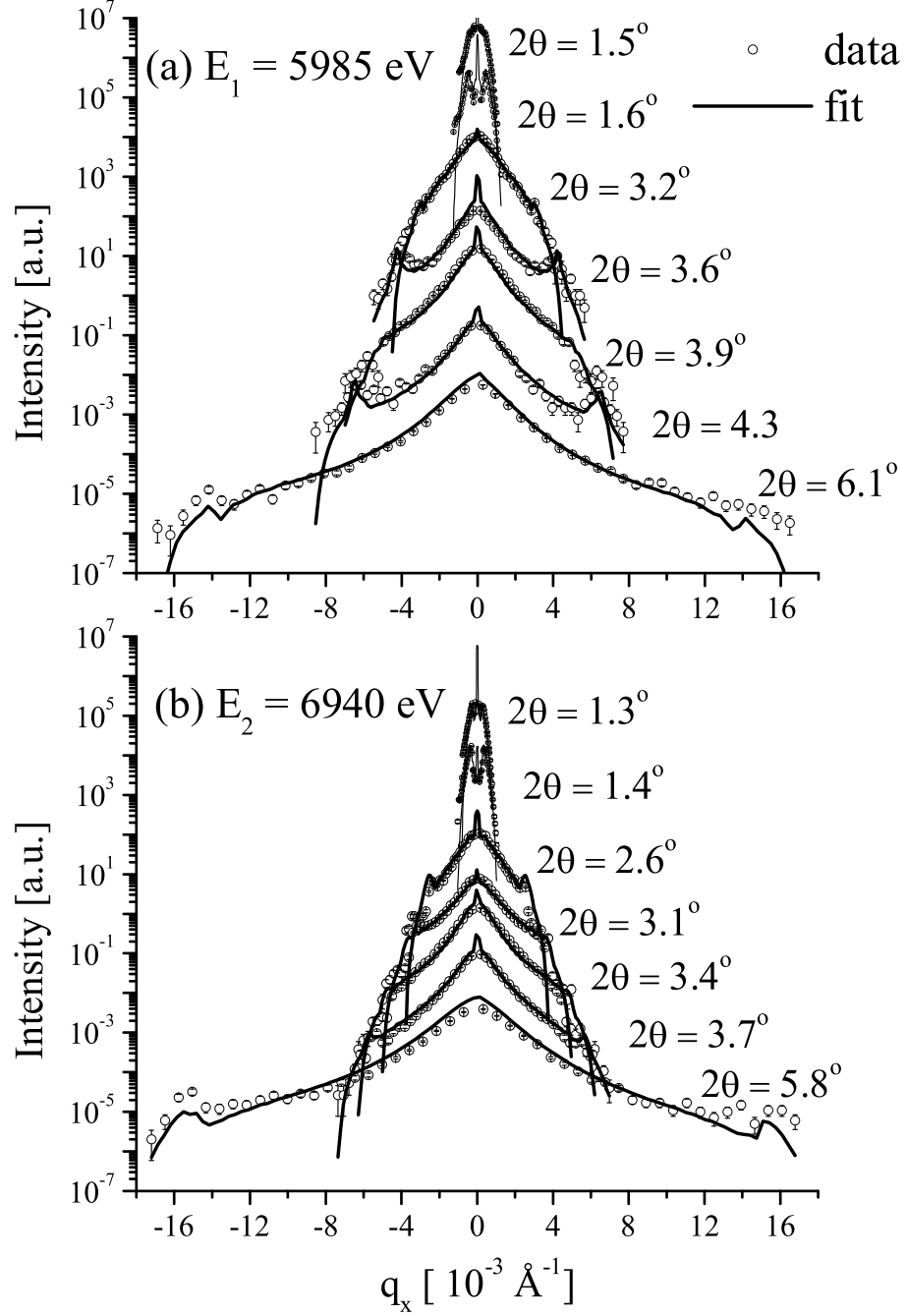


FIG. 24: Omega scans for different $2\theta = \alpha_i + \alpha_f$ values at: (a) - $E_1=5898\text{eV}$ (b) - $E_2=6940\text{eV}$. Open circles are data points, the solid lines show the simulation for the parameters obtained from the best fit. For visualization, all scans are displaced with respect to each other by one order of magnitude in intensity scale.

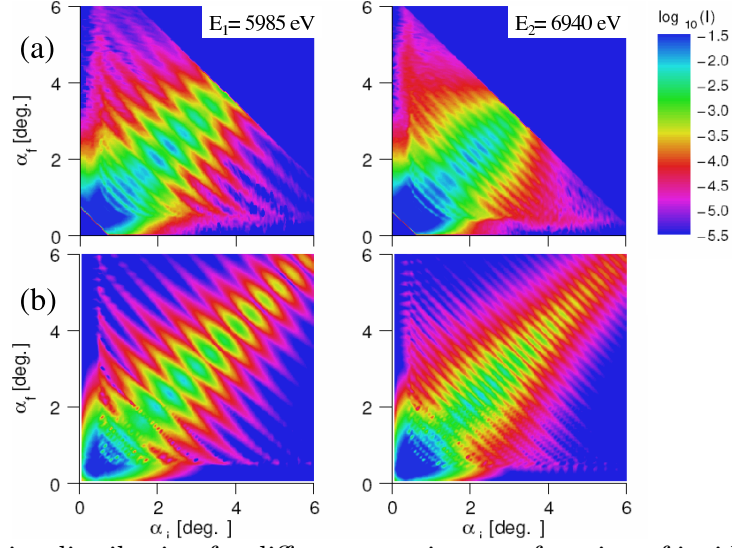


FIG. 25: The intensity distribution for diffuse scattering as a function of incident α_i and scattering α_f angles, (a) - the data, (b) - the simulations. The intensity from specular reflection is not shown.

medium is given by $k_{z,j} = k_1 \sqrt{n_j^2 - \cos^2 \alpha_i}$ with $k_1 = 2\pi/\lambda$ the modulus of the wave vector in the vacuum (λ is the x-ray wavelength) and the incidence angle α_i .

The specularly reflected intensity I can be obtained with eq.(87) via $I = |R_1|^2$, if the amplitude of the impinging x-ray wave is set to $T_1 = 1$ and a semi-infinite substrate is assumed $R_{N+1} = 0$.

Ideal interfaces have been assumed in deriving the Parratt formalism. The nonideality of the interface should be taken into account in real reflectivity calculations since most interfaces are not ideal on the length scale probed by the x-rays. For a non-ideal interface, the average electron density profile along the specimen normal can be modelled by an error function and assuming Gaussian interface roughness [66].

The probability density function of the interface position is

$$P_{Gauss}(z) = \frac{1}{\sqrt{2\pi}\sigma_j} e^{-z^2/2\sigma_j^2} \quad (89)$$

and resulting variation of the refractive index follows

$$n_{Gauss} = \frac{n_j + n_{j+1}}{2} + \frac{n_j - n_{j+1}}{2} \operatorname{erf} \left[\frac{z}{\sqrt{2}\sigma_j} \right] \quad (90)$$

The reflection coefficient turns out to be

$$r_{j,j+1}^{rough} = r_{j,j+1}^{ideal} e^{-2k_{z,j}k_{z,j+1}\sigma_j^2} \quad (91)$$

where, σ_j is the root mean square (rms) roughness of the j th interface.

5.5. Diffuse scattering

The fitting routine of the off-specular intensity is based on the distorted wave Born approximation (DWBA) introduced for scattering from interface roughnesses by S.K.Sinha [68] for one layer and extended by V.Holý [69] for multilayers. For the simulations of the specular reflectivity the well known Parratt formalism has been used [70]. To calculate the diffuse intensity, we used the equation for the differential scattering cross section as presented in [61, 71]:

$$\begin{aligned} \left(\frac{d\sigma}{d\Omega}\right)_{diff} = & \frac{Ak_1^2}{8\pi^2} \sum_{j,k=1}^N (n_j^2 - n_{j+1}^2)(n_k^2 - n_{k+1}^2)^* \\ & \sum_{m,n=0}^3 \tilde{G}_j^m \tilde{G}_k^{m*} \exp\left\{-\frac{1}{2}[(q_{z,j}^m \sigma_j)^2 + (q_{z,k}^{n*} \sigma_k)^2]\right\} S_{jk}^{mn}(q_x, q_{z,j}^m, q_{z,k}^n) \end{aligned} \quad (92)$$

with the structure factor:

$$S_{jk}^{mn}(q_x, q_{z,j}^m, q_{z,k}^n) = \frac{4\pi}{q_{z,j}^m q_{z,k}^{n*}} \int_0^\infty dX (\exp\{q_{z,j}^m q_{z,k}^{n*} C_{jk}(X)\} - 1) \cos(q_x X) \quad (93)$$

where j and k denote different interfaces, A is the illuminated area of the sample, n_j is the refractive index of the layer j just above interface j , $\mathbf{q}_j^m = (q_x, q_{z,j}^m)^T$ is the momentum transfer within each layer. \mathbf{q}_j^m decomposes itself into q_x , the in-plane component of the momentum transfer, and $q_{z,j}^m$ is the perpendicular component of the wave vector within this layer.

The terms $\tilde{G}_j^m \exp[-\frac{1}{2}(q_{z,j}^m \sigma_j)^2]$ appearing on the right hand side of eq.(92) have a clear physical meaning. For instance, the term $T_{j+1}^i T_{j+1}^f \exp[-\frac{1}{2}(q_{z,j}^0 \sigma_j)^2]$ expresses the scattering from the transmitted wave with amplitude T_{j+1}^i into the wave with amplitude T_{j+1}^f . The change of the wave vector corresponding to this process is $q_{z,j}^0 = k_{z,j+1}^i + k_{z,j+1}^f$. The exponential term represents a damping with a "Debye-Waller" - type factor due to interfacial roughnesses [72].

TABLE VI: The expression for G_j^m in eq.(94) with respective momentum transfers according to [71, 73]. T_{j+1}^i, R_{j+1}^i and T_{j+1}^f, R_{j+1}^f are the amplitudes of the transmitted and reflected incoming and outgoing beams, respectively in layer j as obtained from the Parratt formalism for sharp interfaces $k_{z,j}^{(i,f)} = k_1[n_j^2 - \cos^2 \alpha_{(i,f)}]^{1/2}$ is the z -component of the incoming (i) or outgoing (f) wave vector in layer j .

$G_j^0 = T_{j+1}^i T_{j+1}^f$	$q_{z,j}^0 = k_{z,j+1}^i + k_{z,j+1}^f$
$G_j^1 = T_{j+1}^i R_{j+1}^f$	$q_{z,j}^1 = k_{z,j+1}^i - k_{z,j+1}^f$
$G_j^2 = R_{j+1}^i T_{j+1}^f$	$q_{z,j}^2 = -q_{z,j}^1$
$G_j^3 = R_{j+1}^i R_{j+1}^f$	$q_{z,j}^3 = -q_{z,j}^0$

The quantity \tilde{G}_j^m is defined through

$$\tilde{G}_j^m = G_j^m \exp(-iq_{z,j}^m z_j) \quad (94)$$

where G_j^m are the coefficients describing the dynamical effects (see Tab.VI) and z_j is the vertical position of interface j (layer thickness $d_j = z_{j+1} - z_j$, see Fig.20).

The $C_{jk}(X)$ in eq.(93) denotes the auto ($j = k$) - and cross ($j \neq k$) - correlation functions between interface j and k . Here we assume that the interface heights are Gaussian variables of the lateral coordinate and that the interface j fluctuates with a root-mean-square (rms) roughness value that saturates to a value σ_j above an effective cutoff length denoted as ξ_j . Due to the horizontally focusing of our experimental setup we integrate over the corresponding intensity distribution along q_y .

Assuming self-affine rough interfaces at length scales well below ξ_j , the height-height auto-correlation function of interface j can be written as:

$$C_{jj}(X) = \sigma_j^2 e^{-(X/\xi_j)^{2h_j}} \quad (95)$$

The exponent ("Hurst parameter") h_j ($0 < h_j < 1$) determines how smooth or jagged such an interface is. Small values of h_j correspond to extremely jagged interfaces, while value of h_j approaching 1 correspond to smooth hills and valleys.

Therefore, in a statistical description using the model described in [68, 69] each interface and layer j is characterized by six parameters:

- d_j - the thickness of the layer j ;
- $n_j = 1 - \delta_j + i\beta_j$ - the refractive index of layer j which is energy dependent;
- σ_j - the rms roughness amplitude for interface j ;
- ξ_j - the lateral correlation length of roughness for interface j and h_j - the Hurst parameter for interface j .

To calculate the cross-correlation function C_{jk} , the auto-correlation function is first Fourier transformed. The Fourier transform of the cross-correlation function is then defined through

$$\tilde{C}_{jk}(q_x) = \left[\tilde{C}_{jj}(q_x) \tilde{C}_{kk}(q_x) \right]^{\frac{1}{2}} e^{-|z_j - z_k|/\xi_{jk}^{\perp}} \quad (96)$$

where, ξ_{jk}^{\perp} is a quantity of dimension "length" denoting how strong the height fluctuations of interface j and k are correlated ("vertical correlation length").

If $\xi_{jk}^{\perp} = 0$, interface j and k are not correlated and $\tilde{C}_{jk}(q_x) = 0$. If $\xi_{jk}^{\perp} \gg |z_j - z_k|$, the two interfaces are fully correlated.

The cross-correlation function in real space $C_{jk}(X)$ is then obtained by inverse Fourier transformation of $\tilde{C}_{jk}(q_x)$.

For our fits we assumed ξ_{jk}^{\perp} to be independent of the pair (j, k) of interfaces considered.

Due to the large number of parameters, an independent refinement without prior knowledge leading to good estimations of starting values will not be successful. Some estimations can be obtained from the preparation conditions and some from inspection of the raw data.

From the q_z period Δq_z of the Kiessig fringes in the reflectivity a layer thickness can be estimated by $D = 2\pi/\Delta q_z$. For the energy $E_1=5985\text{eV}$ with maximal contrast, the oscillations stem mainly from the thickness of the Fe layer, while for $E_2=6940\text{eV}$ at vanishing contrast, the total Fe/Cr/Fe trilayer thickness becomes visible.

From the data in Fig.23 we obtained thicknesses of Fe layers and of the spacer Cr layer, which are close to those obtained by the quartz microbalance during the sample preparation (see Tab.V). In the model we assumed the infinite thickness of Ag buffer layer and ignored the GaAs substrate.

Tabulated values were taken for δ_j and β_j for both energies [67]. This approximation is good enough due to the match of the critical angle of total reflection $\alpha_i^c \sim \sqrt{2\delta_2^{Ei}}$ for both energies. While δ_j was a free parameter, the absorption coefficients β_j were kept fixed during

the refinement since they are one order of magnitude smaller than the dispersion. To adjust the refractive indices and thicknesses of every layer we performed simulations. For the simulations of diffuse scattered intensity we have found first the initial values of the lateral correlation length $\xi_j = 3000\text{\AA}$ and the Hurst parameter $h_j = 0.8$ for each layer ($j = 1..5$). They were adjusted by the widths of the omega scans and were also constrained to be equal at all interfaces during the simulations and the following fits.

On top of the trilayer we introduced an oxide layer with reduced refractive index. The initial values of the thickness d_1 and refractive index n_1 of this layer were adjusted by the simulations of the reflectivity scans.

The correction of the measured data due to the illumination effect, which is related to the sample size and the the projection of the incoming beam onto the sample surface, and the instrumental resolution effect have been taken into account during simulations and fits, as it is described in [74].

At higher incident angles the specular reflected intensity in our experiment became comparable, or even less than the diffuse scattered photon intensity due to the scattering from "in-plane" roughness. There are methods [75] to separate the diffuse scattering from the specular reflectivity resulting in a "true specular reflectivity". But, as it was already discussed [73, 76] the fitting of the "true specular reflectivity" alone can give misleading results, especially in case when the intensity due to diffuse scattering is comparable with the intensity due to specular reflectivity. This is the reason why we fitted simultaneously the diffuse and specularly scattered intensities.

In a first step we performed the fits at the second energy $E_2=6940\text{eV}$. Due to the low Fe/Cr contrast a significant number of parameters, namely all those describing the interfaces between Fe and Cr layers, become irrelevant for the fit and can be fixed to tabulated values. Thus the free parameters during this fit were: the thickness of the oxide layer d_1 , the refractive index $\delta_1^{E_2}$ and the rms roughnesses of the air/Fe-oxide, Fe-oxide/Fe and Fe/Ag interfaces, as well as the Hurst parameter h_j and lateral correlation lengths ξ_j ($j = 1, 2, 5$).

While this is still a large number of parameters, one has to keep in mind that we have good estimations from prior knowledge of the system and that we used all data from specular as well as off-specular scattering for a simultaneous refinement.

Keeping these parameters constant we have performed the fits for photon energy E_1 using

d_j, δ_j, σ_j ($j = 3, 4$) as free parameters for the Fe/Cr and Cr/Fe interfaces.

The results of the simultaneous fits of the specular reflectivity, longitudinal diffuse and omega scans are shown in Fig.23 and Fig.24. The structural parameters obtained from the fits are presented in Tab.VII.

5.6. Results and discussion

Here, we will first examine the quality of refinement and point out the limitations of applied method. Then we will discuss the morphology of the multilayer system, comparing parameters expected from the preparation procedure with the actual structure of our sample. And finally, we will discuss the strength and limitations of the method.

At both energies, diffuse scattering can be observed extending for certain q_z values along the q_x direction (constant $\alpha_i + \alpha_f$). These "Bragg sheets" are characteristic for vertically correlated roughnesses between interfaces. However, the q_z period is quite different for both energies. Since for both energies, the biggest contrast comes from the interfaces of the trilayer with the substrate and with vacuum, the oscillations due to the total trilayer system are present at both energies. For the data at high contrast, the Fe/Cr interfaces become visible in addition as is nicely seen in the data presented in Fig.25. The beating effect between the many spatial frequencies present in Fig.23(a) amplifies the oscillations due to the Fe layer thickness in the Q-range from 0.2 to 0.4 \AA^{-1} , while the oscillations due to the total trilayer thickness are visible at low Q values. Corresponding to the larger thickness in real space, the oscillation period is small in Fourier space at E_2 . Based on the parameters obtained it was possible to reproduce the dispersion profile in z direction at both energies with the given roughnesses - Fig.26. Fig.27 shows one of the possible realizations of the sample structure in real space consistent with parameters given in Tab.VII. The refinement of the intensities at the specular position (see Fig.23(a,b)) deviate for both energies from the data at higher q_z values. As discussed in [68], the DWBA is a good approximation to calculate the diffuse scattering for $q_z\sigma < 1$ (see Ref.[68], before eq.(4.38)). In our case, we see deviations starting at q_z larger than 0.35 \AA^{-1} where, depending on the interface considered, we have values of $q_z\sigma$ between 1.5 and 3.5.

The fit of the reflectivity is not perfect in the q_z -range from 0.12 \AA^{-1} to 0.2 \AA^{-1} for both

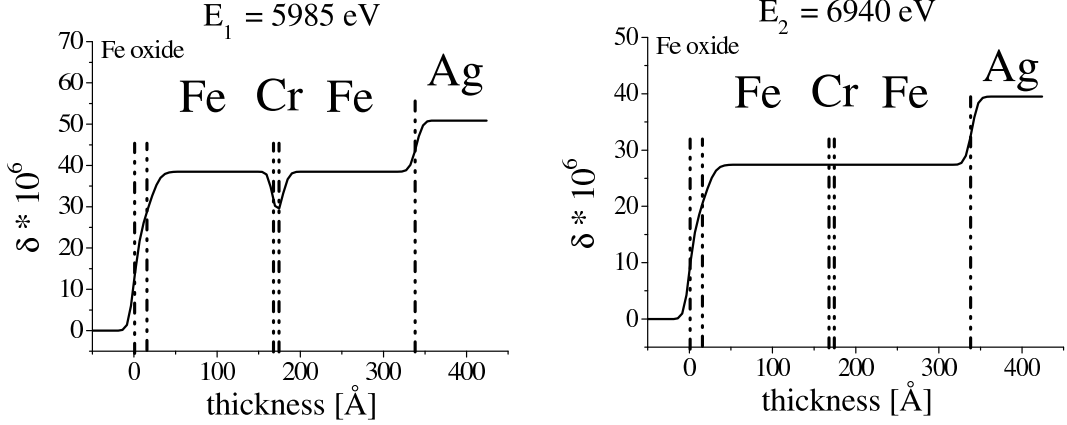


FIG. 26: The dispersion profile for both energies [47]. Note that the tanh profile at the interfaces results in a smearing out and plateau for the oxide layer and Cr layer vanish.

TABLE VII: The structural parameters obtained from the simultaneous fit of reflectivity, longitudinal diffuse scan and seven omega scans at both energies. We assumed fully vertical correlated roughness and thus fixed the corresponding correlation length $\xi_{\perp} = 10000\text{\AA}$ (infinite in practice). The β_j values were kept fixed to the tabulated values [67] during refinement. The values marked with a star were constrained to be equal during the fitting. In brackets: tabulated/nominal values used as starting values in the simulations, deduced from the data and sample preparation details.

j	layers	$d_j[\text{\AA}]$	$\delta_j^{E1} \times 10^6$	$\delta_j^{E2} \times 10^6$	$\sigma_j[\text{\AA}]$	$\xi_j[\text{\AA}]$	h_j
1	Fe oxide	17(1)	21(2)	15(1)	5(1)	2000*(1000)	0.79*(0.1)
2	Fe	150(1) [150]	38*(2) [39.8]	27*(3) [27.5]	10(1)	2000*	0.79*
3	Cr	7(2) [11]	18(3) [21.5]	27* [27.5]	5(1)	2000*	0.79*
4	Fe	164(2) [150]	38* [39.8]	27* [27.5]	7(1)	2000*	0.79*
5	Ag	<i>semi - infinite</i>	50(3) [52.8]	39(2) [39.5]	6(1)	2000*	0.79*

energies. These deviations are due to the top Fe oxide layer, which is not well described within the interface model used in [68, 69]. These deviations can be reduced by varying the fitting parameter for this layer, which mainly affects the fit in the corresponding region. The oxide layer is due to the intense x-ray beam from the synchrotron storage ring which causes a break up of the gas molecules in air and produces strongly reactive O_3 and HNO_3 even from rest gas in a vacuum recipient. This causes a chemical reaction with the exposed metal surface and is visible in a beam-footprint on the sample. It is likely that the assumption of a

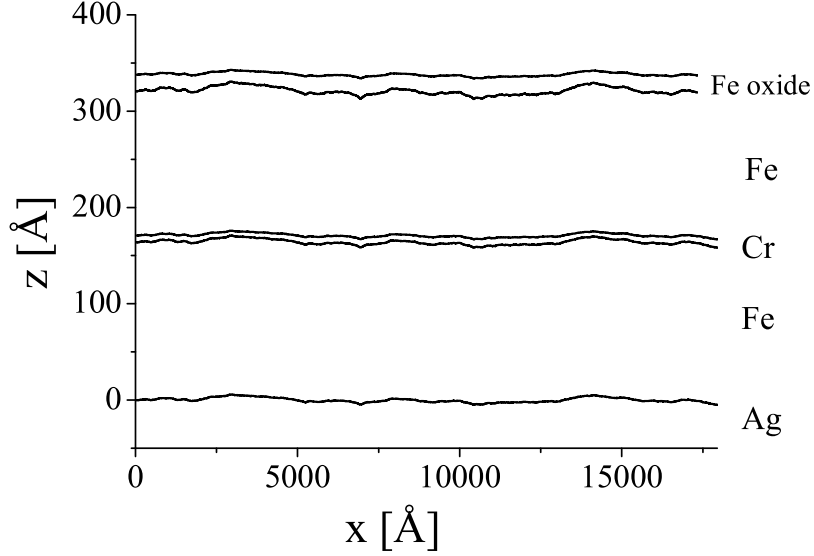


FIG. 27: A possible realization of the sample structure in (x, z) plane

self-affine rough interface does not hold for such oxide layer. Since we were mainly interested in the interfaces between Fe and Cr, we accepted the deviations in the reflectivity curve of Fig.23(a) after we had convinced ourselves that they were caused by limitation in the model description of the oxide layer only.

The thickness of the Cr layer evaluated from the fits (7.3\AA) is smaller than the one obtained by the quartz microbalance of MBE machine (11\AA). At the same time the thickness of the bottom-most Fe layer is larger than the one obtained by the microbalance (see Tab.VII). This can be an indication for interdiffusion at the Cr/Fe interface. As was shown [58, 77], interdiffusion at a Cr/Fe interface is stronger as compared to interdiffusion at a Fe/Cr interface. The explanation was given in terms of a higher melting point of Cr compared to Fe leading to different solubilities. In our case an introduction of interdiffusion layers between Cr/Fe and Fe/Cr interfaces with an averaged electron density did not improve the quality of the specular and longitudinal diffuse scans.

Introducing such additional layers increases the number of refined parameters significantly. Clearly, with our limited data set, these additional parameters can not be determined. Here we approach the limits of our method, as we already have to determine the parameters describing the morphology of four layers plus buffer. Nevertheless, we interpret the refined

layer thicknesses as an indication of dilution of Cr within the bottom Fe layer.

Apart from this observation, the statistical parameters describing the interfaces are rather similar.

In particular, due to the MBE preparation at moderate temperature, vertically strong correlated roughness appears as the main features of an exposed surface are reproduced during the deposition of the next layer. This explains why a continuous Cr interlayer exists despite the fact that its averaged layer thickness is comparable to the interfacial width characterized by the rms roughness. This is consistent with the observation of antiparallel coupling between the Fe layers, while pinholes in the Cr layer would lead to an enhanced parallel coupling.

In summary, we successfully applied the contrast variation method by means of anomalous x-ray scattering in order to achieve a description of the interface morphology of a Fe/Cr/Fe trilayer system on a Ag buffer.

Using two different energies $E_1=5985\text{eV}$ and $E_2=6940\text{eV}$ we achieved the maximum contrast between Fe and Cr layers and vanishing contrast, respectively. Simulations and fits in the frame of DWBA allowed us to describe quantitatively the structure of the sample, including the information about buried layers and a top most oxide layer.

6. MAGNETIC ORDER IN MNO NANOPARTICLES

In this section we will describe the magnetic behavior of MnO nanoparticles and compare this behavior with the magnetic properties of the bulk MnO. Due to the sample preparation the particles are embedded in a porous glass and represent the typical case of magnetism in confined geometry.

Confined geometries impose finite size effects and material dependent interactions with interfaces, which may alter the thermodynamic behavior. We have observed the wetting phenomena near interfaces by polarized neutron scattering near to order-disorder phase transitions. The structure of this section is organized as follows. At the beginning we discuss the magnetic properties of bulk MnO and the sample preparation details for the MnO nanoparticles. Then, the instrument we used is shortly described and the previous results obtained by unpolarized neutron scattering [79] are outlined.

At the end we present our experimental results obtained by polarized neutrons and the model to fit the data. The results of the modeling and obtained physical parameters are discussed.

6.1. MnO embedded in porous glass: sample preparation

The porous matrix was made from a sodium borosilicate glass [78]. It consists pure SiO_2 , which has a random interconnected network of elongated pores with a narrow distribution of pore diameters of $70 \pm 3 \text{ \AA}$. The inner structure of the glass matrix is shown in Fig.28. MnO was synthesized (in collaboration with S. B. Vakrushev, A. F. Ioffe Physico-Technical Institute, St.Petersburg, Russia) from a manganese nitrate solution by a chemical bath deposition method, without applying external pressure inside the glass matrix [79]. The amount of MnO corresponds to roughly 50 weight percent of a sample.

6.2. Physical and magnetic properties of bulk MnO

MnO is a antiferromagnetic below its Néel temperature of 118K [80]. The transition to the antiferromagnetic state is accompanied by distortion of the (fcc)-cubic structure. The room-temperature lattice constant is $4.4457 \pm 0.0002 \text{ \AA}$ and at the helium temperature it

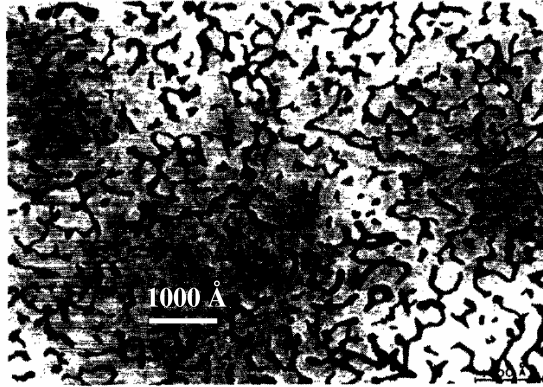


FIG. 28: The micrograph picture of the pore network (dark). Taken from [78].

is $4.4316 \pm 0.0002 \text{ \AA}$ [81]. The neutron diffraction experiments performed by Shull et.al., [80] demonstrated the temperature dependent magnetic behavior of the bulk MnO.

In their experiments they measured the intensity of (111) magnetic reflection for MnO powder at different temperatures as shown in Fig.29(a). The overview of the measurements are summarized in Fig.29(b).

Well below 118K, the magnetically ordered MnO consists of ferromagnetically aligned sheets of spins lying in (111) planes, while the spin directions of these sheets are arranged antiferromagnetically (due to superexchange via oxygen ions) from plane to plane, as it is shown in Fig.30.

6.3. Diffuse neutron scattering spectrometer DNS

The diffuse neutron scattering (DNS) instrument is a time-of-flight spectrometer with polarization analysis which has been designed to study static and dynamic disorder phenomena in condensed matter which give rise to diffuse and wide angle scattering [82]. The sketch of the instrument is shown in Fig.31. The instrument was located in the neutron guide hall (ELLA) at Jülich reactor DIDO until spring 2006 and then transferred to the FRM-2 reactor in Munich.

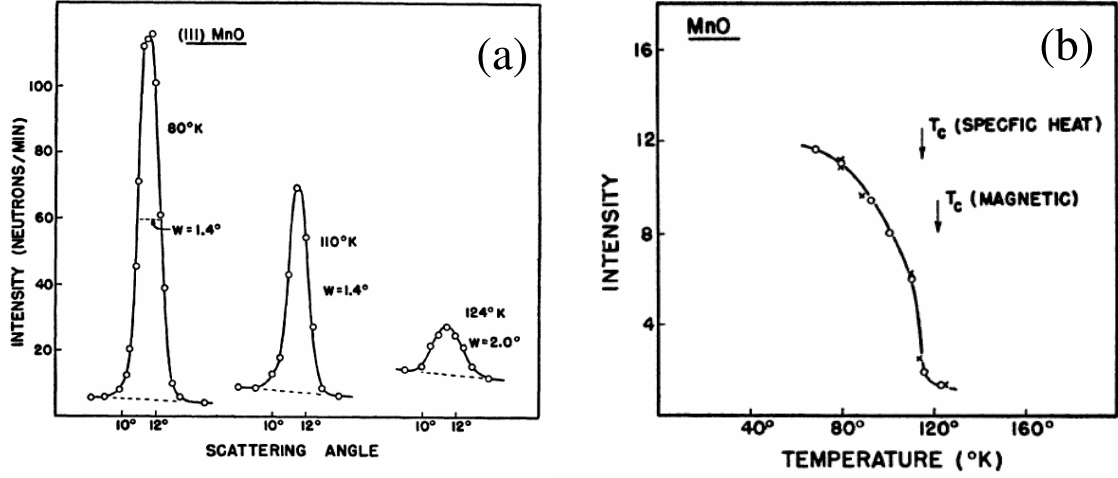


FIG. 29: Magnetic behavior of bulk MnO (a) Antiferromagnetic (111) reflection at different temperatures (b) Temperature dependence of the magnetic intensity. The Néel temperatures suggested by specific heat and magnetic susceptibility data are indicated. Taken from [80].

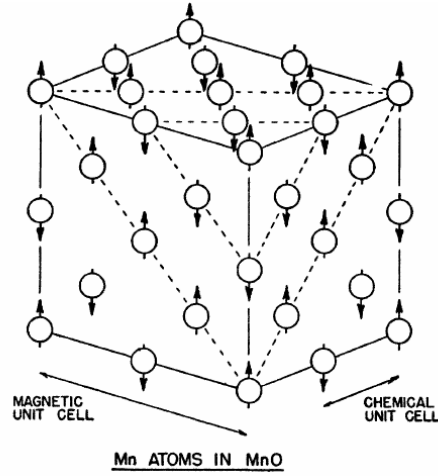


FIG. 30: Antiferromagnetic structure of MnO at low temperature. The magnetic unit cell is twice larger than the chemical unit cell. Only Mn atoms are shown. Taken from [80].

The instrument is suitable for powder diffraction measurements. Neutron polarization analysis can be performed to measure diffuse magnetic scattering and to separate coherent, spin-incoherent and magnetic scattering (see Section 4.1.4).

The SF and NSF processes can be measured with magnetic guide fields at the sample position. The polarization of neutrons can be turned in any desired direction by a setup

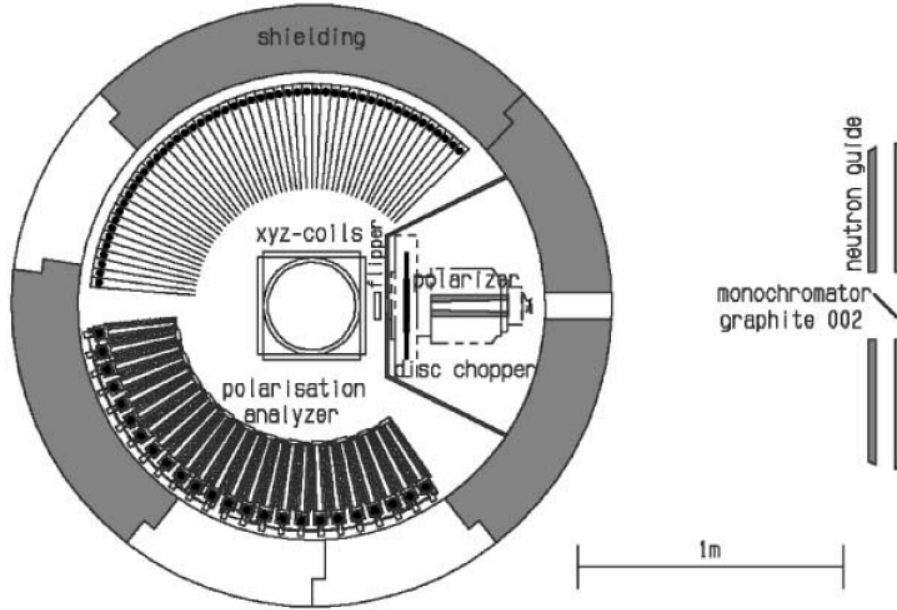


FIG. 31: The DNS instrument at Jülich. Taken from [82].

with xyz-coils around the sample. Therefore, complete vector analysis can be obtained using precessing neutron polarization.

The wavelength of DNS can be varied from 3.3 Å to 5.5 Å. A cryostat can be installed between the xyz-coils.

6.4. Polarized neutron scattering on MnO in porous glass

The aim of our polarized neutron scattering experiment was to study the magnetic phase transition of MnO nanoparticles embedded in a porous glass. Golosovsky et al. [79] have found in non-polarized neutron powder diffraction a continuous phase transition of such MnO nanoparticles, whereas bulk MnO undergoes a discontinuous order-disorder phase transition. In the experiments they used unpolarized neutrons, therefore, it is difficult to conclude unambiguously on the critical behavior because of a strong background from nuclear scattering from the glass (see Fig.32). As it was discussed in Section 4.1.4 the polarization analysis allows us to suppress this background by a few orders of magnitude and thus to observe the weak magnetic scattering.

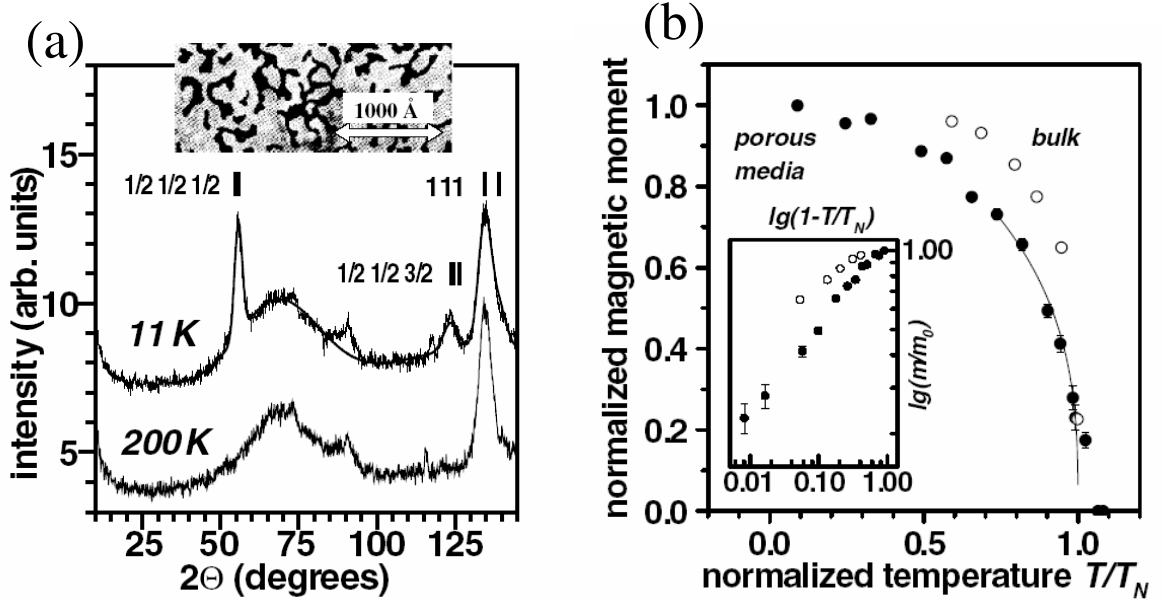


FIG. 32: (a) The unpolarized neutron diffraction patterns of MnO embedded in a porous glass measured at 11K and 200K ($\lambda = 4.732 \text{ \AA}$). The stripes mark the positions of Bragg reflections corresponding to the trigonal distorted lattice. (b) Temperature dependence of the scaled magnetic moment of MnO embedded in a porous glass (filled circles) and in the bulk MnO (open circles). The solid line corresponds to a fit with a power law. The moment dependencies on a logarithmic scale are shown in the inset. Taken from [79].

In our experiment we investigated the temperature dependence of the magnetic $(\frac{1}{2} \frac{1}{2} \frac{1}{2})$ Bragg peak using polarized neutrons with the wavelength of 5.24 \AA within the temperature range from 2K up to 130K. Angular resolution was improved by installing cadmium slits in front of the polarizer. The magnetic $(\frac{1}{2} \frac{1}{2} \frac{1}{2})$ Bragg peak at two different temperatures is shown in Fig.33. The reduction of the peak intensity was observed with increasing temperature up to 118K.

In order to avoid a confusion with the indexing of magnetic peaks in work of Golosovsky and Shull, we would like to stress the following. The Shull's indexing of the observed peaks below T_N was done using the magnetic unit cell (8.88 \AA), which is the doubled chemical unit cell (4.44 \AA). Therefore, the antiferromagnetic reflection is indexed as (111). Golosovsky et al., used the chemical unit cell for the indexing of the peaks. Therefore, the observed antiferromagnetic (111) reflection according to the Shull's notation becomes $(\frac{1}{2} \frac{1}{2} \frac{1}{2})$ reflection

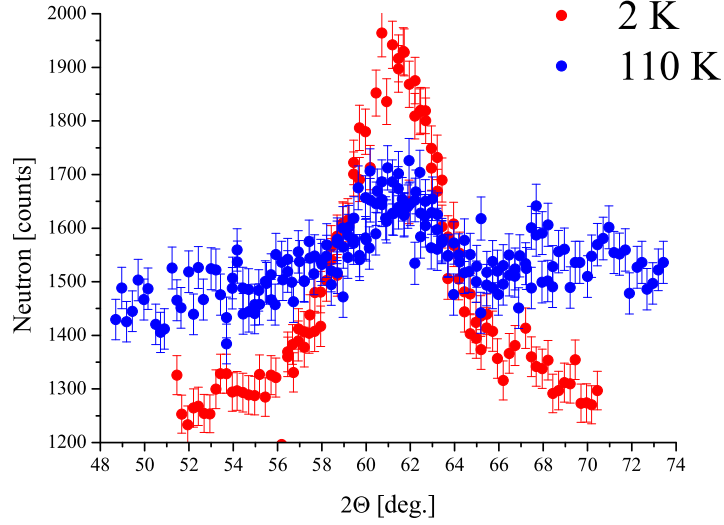


FIG. 33: Magnetic $(\frac{1}{2} \frac{1}{2} \frac{1}{2})$ Bragg peak of MnO embedded in glass at 2K and 110K. The peak is observed in the spin flip channel and contains spin incoherent and magnetic scattering.

in Golosovsky work and in our work as well.

As a reference, MnO powder was measured between 11K and 140K with the same experimental setup.

We have found rather strong diffuse magnetic scattering even in the ordered phase (at low temperatures), resulting probably from a canted magnetic structure close to the pore walls. It means that even at low temperature the outer part of MnO nanoparticles close to the glass walls is disordered and gives rise to the flat background.

The normalized intensity as a function of temperature was obtained from the observed diffraction peaks at different temperatures, for both MnO bulk and MnO nanoparticles (see Fig.34). In agreement with the result of Golosovsky et.al., we found that the transition temperature for MnO glass is slightly increased ($T_N = 122\text{K}$) compared to the one for MnO powder ($T_N = 118\text{K}$) however, the order parameter is lower for the MnO glass for all temperatures.

As seen from Fig.34 the phase transition for MnO nanoparticle becomes continuous at $T_N = 122\text{K}$. The increase of the transition temperature might be explained by strain ef-

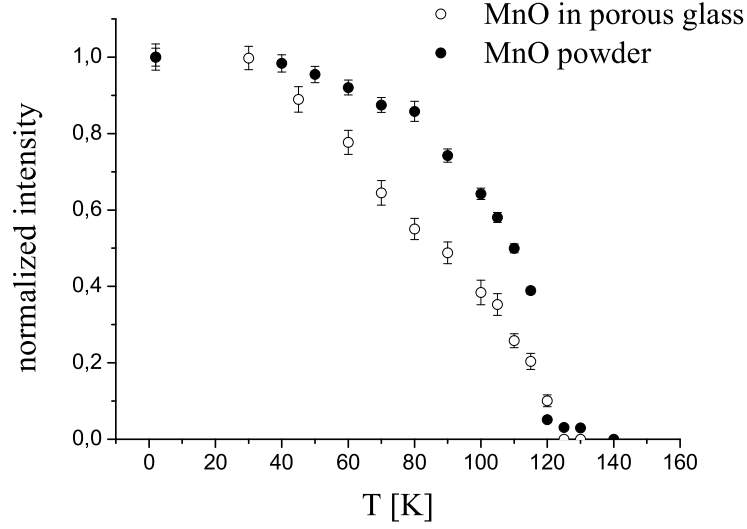


FIG. 34: The normalized intensity of the magnetic $(\frac{1}{2} \frac{1}{2} \frac{1}{2})$ Bragg peak as a function of temperature for MnO nanoparticles embedded in glass and MnO bulk powder.

fects in MnO nanoparticles induced by the glass walls.

We explained the experimentally observed behavior of the order parameter for MnO nanoparticles within a model of frustration due to broken bonds at the interface of MnO nanoparticles. The frustration (see Section 3.1.3) can lead to surface induced disorder and may explain why the order parameter of the MnO nanoparticles is lower compared to bulk MnO and resembles a continuous phase transition.

6.5. Analytical treatment of the measured data

In order to describe the phase transition we used the model of a critical wetting for semi-infinite systems [84] which can be applied to surface-induced disorder [85]. The model describes a situation when a layer of disordered phase gradually introduces at the surface and penetrates into the bulk. Because of the surface inhomogeneity we use this model instead of the description involving single critical exponents.

The detailed derivation of formulas is given in [84, 85]. Here, we present only short outline of the formulas we used to treat the measured data.

The total order parameter for a nanoparticle can be written as a sum of order parameters

for every atomic layer:

$$\Psi = \sum_n N_n \psi_n \quad (97)$$

where, N_n is the number of atoms in atomic layer n and ψ_n is the order parameter in this layer. Here, we neglect a size distribution of pores because it is extremely narrow ($< 5\%$). The order parameter in the n -th layer is expressed as [85]

$$\psi_n = \psi_{max} [1 + \exp \{-2\xi_{\perp}^{-1}(n - \hat{n})\}]^{-1} \quad (98)$$

where, n is the number of atomic layer, \hat{n} is the interface position, ψ_{max} is the maximum order parameter of a system (normally equal to 1), ξ_{\perp} is the interfacial roughness describing the extension of the transition region.

For dimensionality $d = 3$ it was found that the critical behavior at the wetting transition depends on the value of a dimensionless parameter ω :

$$\omega = k_B T_{c,b} / (4\pi \tilde{\Sigma} \xi_d^2) \quad (99)$$

where, k_B is the Boltzmann constant, $T_{c,b}$ is the phase transition temperature of bulk, $\tilde{\Sigma}$ is the interfacial stiffness between ordered and disordered phase, ξ_d is the correlation length of order parameter fluctuations in the disordered bulk phase.

There are two limiting cases which have to be distinguished. They are related to the different form of the potential used in the Hamiltonian describing the phase transition. Therefore, the interface between ordered and disordered phases behaves differently for the large interfacial stiffness ($0 < \omega \leq 1/2$) and for the small interfacial stiffness ($\omega > 1/2$). The preliminary simulations show that for our system the second condition is fulfilled, therefore [84]:

$$\xi_{\perp} = \xi_d \sqrt{\omega} [\ln(1/t)]^{1/2} \quad (100)$$

$$\hat{n} = \sqrt{2\omega} \ln(1/t)$$

where, $t = 1 - T/T_{c,b}$ is the reduced temperature.

Based on this model there is only one free parameter ω , the other parameters were estimated and kept constants. In the following section we will explain how the constant ξ_d and N_n were found.

6.5.1. Initialization of entry parameters

In order to understand the temperature dependent behavior of the order parameter in MnO nanoparticles one should quantitatively describe the system. The first estimate has to be made on the number N_n of atoms in every atomic layer. The first step would be to calculate the number of atomic layers within a MnO nanoparticles with a certain shape. It requires an approximation of shape and size of the MnO nanoparticles. As it was mentioned in the introduction, the particles are worm-like structures with the mean diameter of pores of 70Å. We assumed the particles to be cylindrical with the radius of 35Å. Taking into account the lattice constant of MnO 4.44Å, it is easy to see that such a cylindrical nanoparticle consists of 8 atomic layers.

In order to calculate the number of atoms in each atomic layer we found a volume of hollow cylinder created by an atomic layer n and then divided by the volume of the cubic unit cell. It gives a number of unit cells inside each atomic layer. Then the result was multiplied by the number of Mn atoms inside a unit cell (4).

The recurrent formula can be written for the number of atoms inside each atomic layer n :

$$N_n = 4 \frac{\pi L [(R_0 - (n - 1)a)^2 - (R_0 - na)^2]}{a^3} \quad (101)$$

where, $n = 1..8$ is the number of atomic layer, L is the length of cylinder, $R_0 = 35\text{Å}$ is the radius of cylinder, $a = 4.44\text{Å}$ is the lattice constant of MnO.

The exact knowledge of L is unnecessary since we normalize the resulting fitting curves. In Tab.VIII, the number of atoms are shown for every atomic layer calculated for $L = 250\text{Å}$. In the model we assumed that surface disorder penetrates from the sides of a cylinder and neglect the penetration from the bottom and the top of the cylinder, since its length is much larger than its radius.

The correlation length ξ_d can be derived from the FWHM (full width at half maximum) of the antiferromagnetic peak of MnO powder in the disordered phase, above its Néel temperature $T > T_N$. In the scattering experiment the observed FWHM of a peak is a result of the convolution of two functions. The one is an instrument resolution function which is temperature independent. And the other one is a "real" magnetic peak with the temperature dependent FWHM.

TABLE VIII: The number of atoms in every atomic layer in cylindrical MnO nanoparticles with $R_0 = 35\text{\AA}$ and $L = 250\text{\AA}$. The last column shows the ratio of this number to the total number of atoms in the nanoparticle

layer number	N_n	%
1	10448	23.77
2	9033	20.55
3	7617	17.33
4	6202	14.11
5	4787	10.89
6	3372	7.67
7	1957	4.45
8	542	1.23

If we assume both functions to be Gaussian function with the width $\delta\theta_{resol}$ and $\delta\theta_{real}$ respectively, then

$$\delta\theta_{observed} = \sqrt{\delta\theta_{real}^2 + \delta\theta_{resol}^2} \quad (102)$$

The resolution of our instrument was not good enough to define ξ_d unambiguously. Thus, neutron data of MnO powder by Shull et. al., [80] was used.

The ξ_d was reduced from the FWHM of the antiferromagnetic peaks observed at low and high temperatures (see Fig.29(a)). At T=80K the width is due to the finite instrumental resolution which is $\delta\theta_{resol} = 1.4^\circ$. The observed FWHM of the magnetic peak at T=124K is due to the resolution effect and the magnetic disorder.

From eq.(102) and the given resolution $\delta\theta_{resol}$, the FWHM of the peak in 2θ scan is:

$$\delta\theta_{real} = \sqrt{\delta\theta_{observed}^2 - \delta\theta_{resol}^2} \simeq 1.4^\circ \quad (103)$$

From the relation between the modulus of the scattering vector Q and the scattering angle θ ($Q = (4\pi/\lambda) \sin \theta$), the FWHM of the peak in Q -space corresponds to $\delta Q = 0.14\text{\AA}^{-1}$. The correlation length ξ_d can be calculated from FWHM of the observed peaks

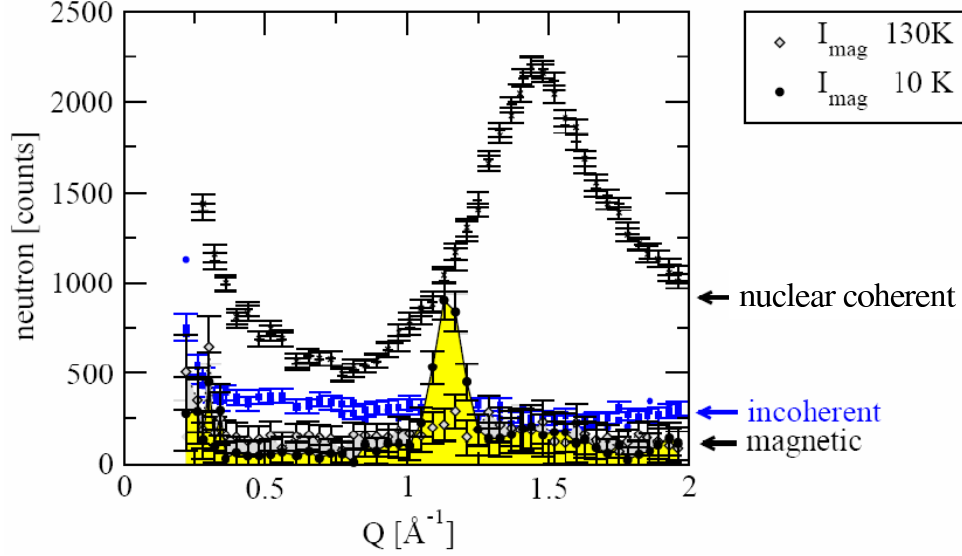


FIG. 35: Separation of nuclear coherent, nuclear incoherent and purely magnetic scattering with full polarization analysis on DNS for two temperatures: 130K and 10K ($\lambda = 3.3\text{\AA}$).

$$\xi_d \propto \frac{1}{0.5\delta Q} \simeq 14.2\text{\AA} \quad (104)$$

or in the other words, $\xi_d \sim 3$ lattice units.

The full polarization analysis for the magnetic Bragg peak of MnO nanoparticles was performed, in order to extract the pure magnetic scattering. The result is shown in Fig.35 for two temperatures above and below the phase transition. This data indicates that a part of MnO nanoparticles remains disordered even at very low temperatures, resulting in a flat background (see Fig.36).

We interpret this disorder as being due to interactions of the outmost MnO layers of the nanoparticles with glass walls. This contribution is turned to be temperature independent and cannot be explained within a frame of our model.

From the peak-to-background ratio at 10K we estimate that about 61% of atoms inside a MnO nanoparticle remain disordered (more details on calculation the peak-to-background ratio can be found in Appendix B).

Therefore, we excluded three atomic layers (which corresponds to 61% of atoms) from the surface by putting the number of atoms within these layers to zero: $N_{1-3} = 0$.

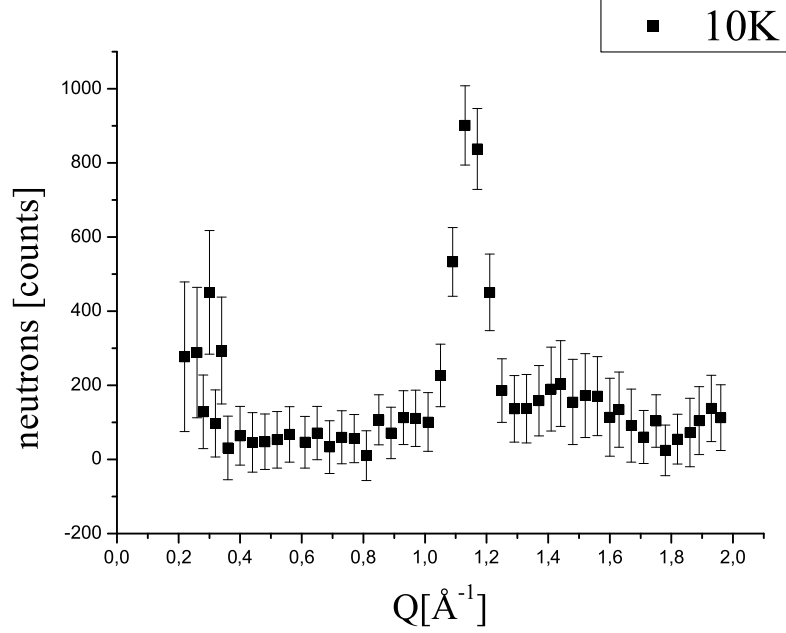


FIG. 36: The pure magnetic scattering obtained with polarization analysis on DNS for MnO nanoparticles at $T=10\text{K}$. Note that the neutron wavelength in this experiment was $\lambda = 3.3\text{\AA}$.

6.6. Results and discussion

Before the fitting, we performed preliminary simulations in order to check the relevance of estimated constants. The simulations indicated that $\omega > 1/2$ therefore, equations for the small interfacial stiffness have to be used. The simulation indicates the value of $\xi_d = 2$ which is in good agreement with the value estimated from the experimental data ($\xi_d = 3$). After initialization of all constants, only the ω parameter was fitted. The best fit is shown in Fig.37 as a solid line.

We found $\omega = 6.8 \pm 0.57$ which indicates a relatively smooth interface between order and disordered phases as it was expected for $\omega > 1/2$.

It can be seen from the order parameter profile (Fig.38) reconstructed for the given value of ω according to eq.(98).

Surprisingly, the outermost three layers are disordered due to the interaction with glass walls or surface spin-canting. According to the core-shell model introduced in Section 3.1.3 one may expect that only one atomic layer is disordered. However, the fit based on the core

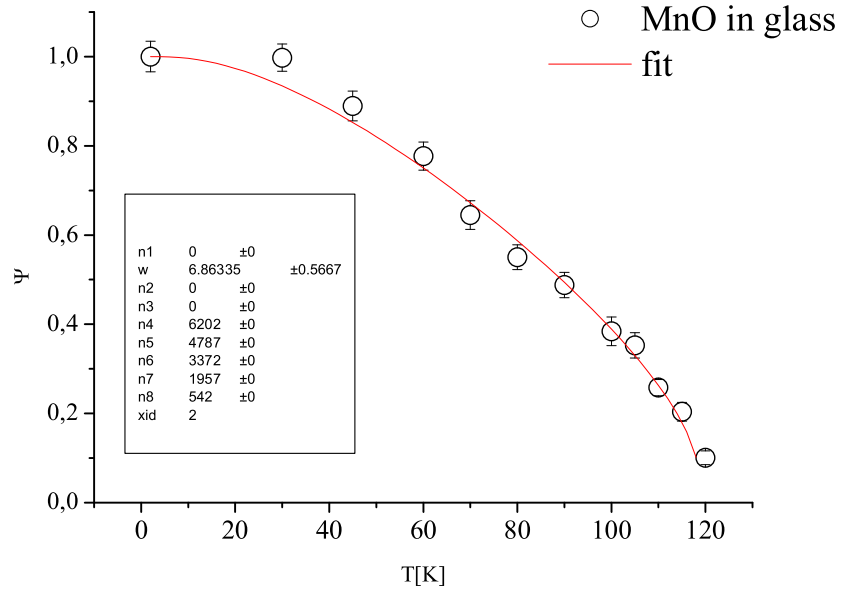


FIG. 37: The order parameter Ψ for MnO nanoparticles as a function of temperature. The solid line represents the best fit (see text for details).

and one-layer-shell model shows a poor agreement with experimental data.

The reason why three layers are disordered is not yet clear and require probably additional experiments which will be discussed in Section 8.2.

In conclusion, we have shown that surface induced disorder can explain the observed continues phase transition for MnO nanoparticles over the entire temperature range using a single free parameter related to the interface stiffness of the Mn spins in MnO.

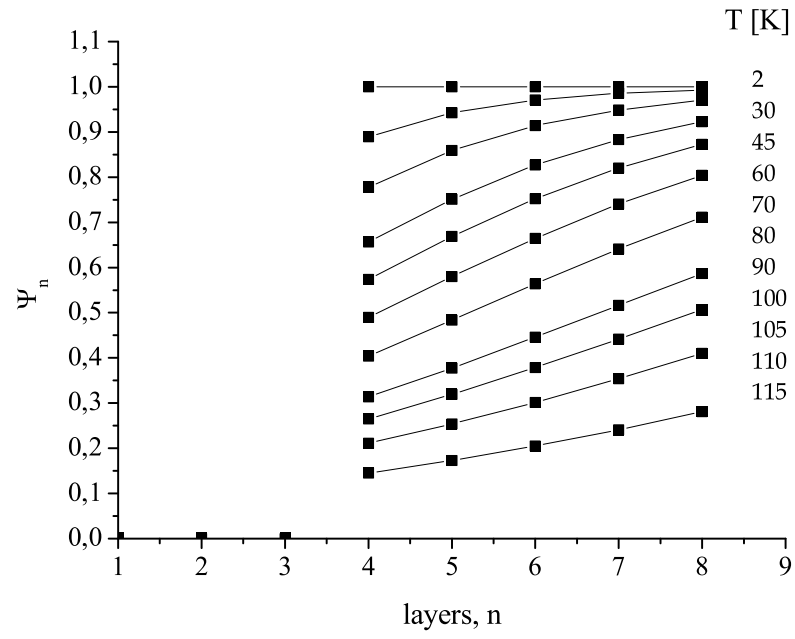


FIG. 38: The order parameter ψ_n in every atomic layer.

7. MAGNETIC AND STRUCTURAL PROPERTIES OF CO NANOPARTICLES

In this chapter we present a study of magnetic and structural properties of Co nanoparticles.

Due to the rich variety of physical phenomena magnetic nanoparticles display and due to possible technological applications, they are in the focus of current research activities. Co nanoparticles in particular are promising candidates for new types of magnetic memories.

We recall again the main effects which are expected for magnetic nanoparticles: superparamagnetic behavior, enhancement of anisotropy constant, a non-uniform magnetization distribution within a single particle, magnetic correlations in ordered array of nanoparticles, oxidation effects (exchange bias), self-assembly under external magnetic field and etc.

To study these effects on a microscopic scale magnetic neutron scattering is one of the most promising techniques. However, the structural and magnetic characterization of the nanoparticles has to be carried out in order to perform successful neutron scattering measurements and to prove that the particles are magnetic.

Despite intensive research very little is known about the magnetization distribution within a single particle and magnetic correlations in ordered arrangements of the nanoparticles. Our goal is to study highly monodisperse Co nanoparticles with a size distribution narrower than 10% in a solution with polarized small-angle neutron scattering. The aim is to measure magnetic and nuclear form factors and to thus determine the average magnetization density within a single particle. While it is expected be constant in the inner part of the particle, one expects deviations close to the surface of the particle. Up to now, this effect has not yet been observed with neutrons. But due to the structural morphology and local anisotropy, one expects a canting of the moments in a surface-near layer, which might be accessible to flipping ratio measurements of polarized neutrons for truly monodisperse nanoparticles. Here, we present a structural characterization by small-angle x-ray scattering and magnetic characterization by magnetization measurements.

7.1. Colloidal synthesis of nanoparticles

We developed a new synthesis route for Co nanoparticles employing microemulsions, which aims at a narrow size distribution. For the synthesis of the Co nanoparticles two

different routes are known from literature. One is the thermal decomposition of $\text{Co}_2(\text{CO})_8$ published by Murray and Sun [86]. The other route was first put forward by Pileni [87]. For the synthesis of the Co nanoparticles the interior of water-in-oil (w/o) microemulsions were employed as nanoreactors. Because of (i) the less dangerous starting reactions and (ii) our experience with microemulsions we decided to implement the Pileni route for the synthesis of our nanoparticles. Before we proceed with the sample preparation details, let us introduce the basic definitions used in colloidal chemistry.

The main idea behind the colloidal synthesis of nanoparticles is to use the constrained nono-size reactors. We used microemulsion templating to produce spherical Co nanoparticles.

A microemulsion is the thermodynamically stable, isotropic dispersion of two relatively immiscible liquids consisting of microdomains of one or both liquids stabilized by an interfacial film of surface active molecules (surfactant).

The microemulsions have the following properties which allowed us to use them for creation of nanoparticles:

- Droplets of dispersed phase are diffusing through a continuous phase
- Droplets are separated
- The average size and number of droplets remain constant as a function of time

The surfactant molecule consists of a polar head group and an aliphatic tail. Depending on the dispersed and continuous phases two types of microemulsions are distinguished: water-in-oil (w/o) and oil-in-water (o/w). In both cases, the dispersed phase consists of monodispersed droplets in the size range 10-100nm. The size and the particle shape is driven by the shape of the droplets (micelles). The micelles are formed above the critical micelle concentration (cmc). At this concentration it is more energetically favorable for surfactants molecules to form the micelle.

The shape of the micelles in microemulsions depending on surfactant, oil and water concentrations can be displayed in a Gibbs triangle (Fig.39). We would like to emphasis once again that the final particle morphology is influenced by properties of the microemulsion system.

Microemulsion templating

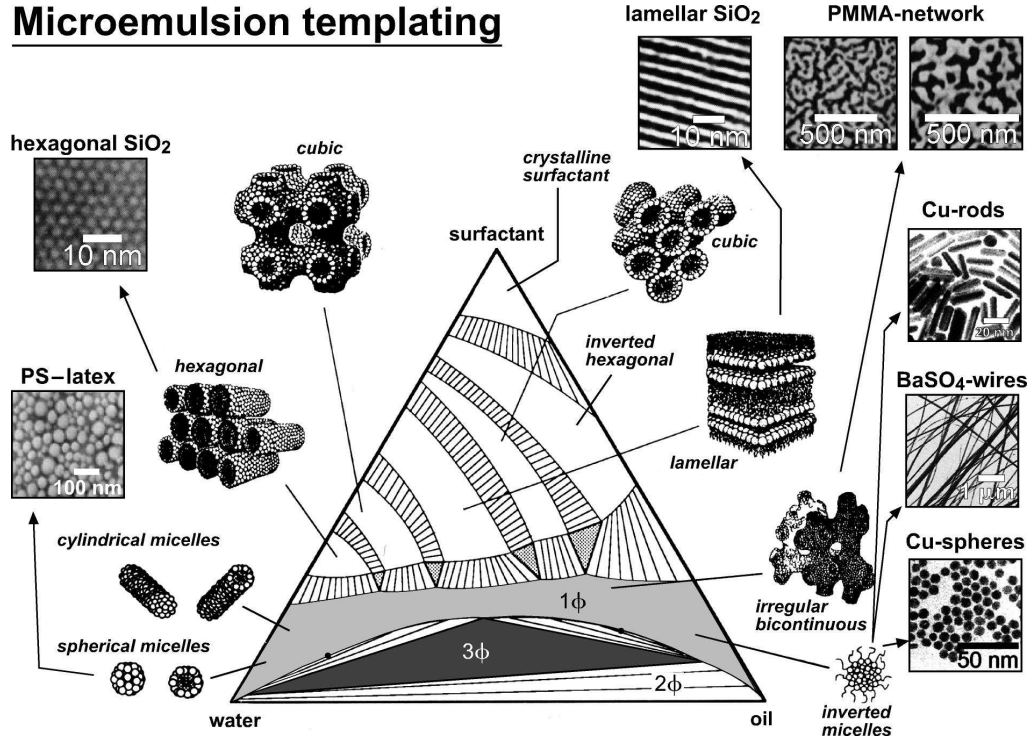


FIG. 39: Schematic Gibbs triangle displaying self-assembly structure formation in binary and ternary surfactant systems. The outer part shows examples for solid phases of different morphologies that have been prepared from the indicated self-assembled surfactant phases [88–91]. Taken from [92].

7.2. Sample preparation details

In their early paper [87] Pileni and coworkers used w/o microemulsions that were stabilized by NaAOT ($\text{NaC}_{20}\text{H}_{37}\text{SO}_7$), whereby the Co^{2+} -delivering microemulsion contained additionally $\text{Co}(\text{AOT})_2$ and water and the second microemulsion that delivered the reducing agent contained only NaAOT and the aqueous NaBH_4 -solution.

Let us explain the role of the reducing agent. Using the various concentrations of the reduction agent, one can separate the nucleation and growing of spherical metallic nanoparticles. Metal ions solubilized in the aqueous core become reduced when the reduction agent enters the droplet interior (Fig.40). If the number of metal atoms is higher than the critical aggregation number n^* a metal cluster nucleus forms that grows due to exchange of metal ions from other droplets. Nuclei formed grow via interdroplet exchange until all free metal

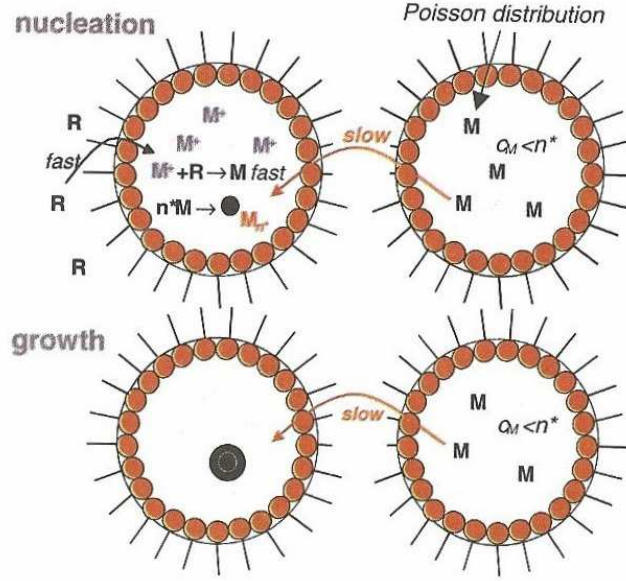


FIG. 40: The scheme of the nucleation and growth of spherical metallic nanoparticles. Where, M^+ are metal ions, n^* is the critical aggregation number, R is the reduction agent and the filled circles are metallic nanoparticles. Taken from [92].

ions are used up. Generally, the more nuclei are formed the less free metal ions are left for particle growth [92].

In this way, particle size and polydispersity could be adjusted by the water-to-surfactant ratio (w/s) and the molar ratio between Co^{2+} and $NaBH_4$. The major problem of this approach was the low yield of Co nanoparticles. Therefore, in recent papers Pileni et al. used microemulsions stabilized by $Co(AOT)_2$ only, to which they injected the aqueous $NaBH_4$ -solution directly [93]. However, this synthesis route is less defined, since the microemulsions phase separate upon addition of the $NaBH_4$ -solution. In order to circumvent both the low yield of Co nanoparticles and undefined particle formation conditions due to phase separation, we explored a synthesis route in which we employed w/o microemulsions that are stabilized by the nonionic surfactants of the ethoxylated alkyl- or arylether series such as $C_{12}E_5(C_{22}H_{46}O_6)$ and Igepal CO520 ($C_{25}H_{44}O_6$) and contain the $NaBH_4$ -solution. Co nanoparticle formation is then induced by injecting a solution of $Co(AOT)_2$ in hexane or toluene.

Preliminary magnetic measurements on the Co particles prepared in the microemulsions

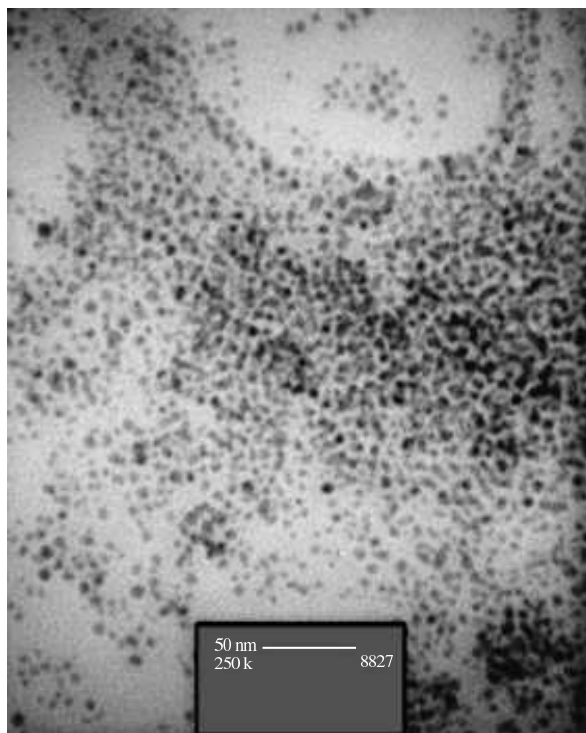


FIG. 41: The TEM picture of Co nanoparticles dried on Cu-grid. The white bar corresponds to 50nm.

show that they are not stable against oxidation. We found out that the water inside the microemulsion leads already to oxidation of the particles. We did not find exact preparation conditions in original Pileni's recipe which allows to avoid fast oxidation of Co nanoparticles. Therefore, we developed a new route without water by reducing $\text{Co}(\text{AOT})_2$ micellar solutions with organic borhydrides NaBu_3BH as a reduction agent for particle synthesis. An advantage of using this reduction agent that it is soluble in toluene in contrast to NaBH_4 which is soluble only in water. The reduction reaction was performed inside the glove box in order to prevent immediate oxidation of the Co nanoparticles due to the contact with oxygen and/or water.

The Co nanoparticles are stable in reverse micellar solution against oxidation for weeks if stored under the nitrogen atmosphere.

7.3. Magnetic properties

For a magnetic characterization, we performed SQUID measurements of the particles in solution, for which a special sample container had to be developed.

The sample container for measuring the liquid solution of Co nanoparticles has to fulfill a number of conditions. It should give a weak diamagnetic contribution compared to the superparamagnetic signal of the Co nanoparticles. The container should be chemically inert and has to be liquid and air tight to prevent oxidation and leakage of the sample inside SQUID.

In order to achieve the above listed requirements, we used quartz as a material for the sample container design. The sample was filled inside a long-neck sample holder (Fig.42(a)) under nitrogen atmosphere in a glove-box. Then, the lower part was frozen in liquid nitrogen and the long neck was sealed with a high temperature burner. As a result, Co nanoparticles are sealed in the quartz container (Fig.42(b)) without being exposed to air. The container is air and liquid tight. The measurements of an empty container were carried out for a correct background subtraction. The diamagnetic background due to the sample container was subtracted as it is shown in Fig.44. In order to define the blocking temperature T_B of our particles we performed ZFC/FC magnetic measurements. First, the Co nanoparticles solution was cooled down to 2K without applying magnetic field. Then, $H = 10$ mT was applied and magnetization as a function of temperature measured (ZFC). For FC measurements the sample was cooled down to 5K at $H = 10$ mT and magnetization as a function of temperature was measured.

We note that the magnetization M cannot be reliably obtained in absolute units (emu/g), due to undefined amount of Co ions which formed nanoparticles. Not all Co ions were reduced and therefore free Co(AOT)_2 micelles are still presented in inverse micellar solution. The ZFC/FC measurements (Fig.43) shows that the particles are superparamagnetic with a blocking temperature of about 10K. The peak in ZFC curve is rather narrow, indicating that the size distribution is small. Using eq.(6) and anisotropy constant for the bulk Co we estimated a radius of 1.4nm. The hysteresis loop is reversible even at 10K and shows no coercivity field, as expected for superparamagnetic nanoparticles (see Fig.46). We performed hysteresis loop measurement above 10K, however, only the diamagnetic signal from the empty cell was observed (Fig.45). The differences for 100K and 250K are likely

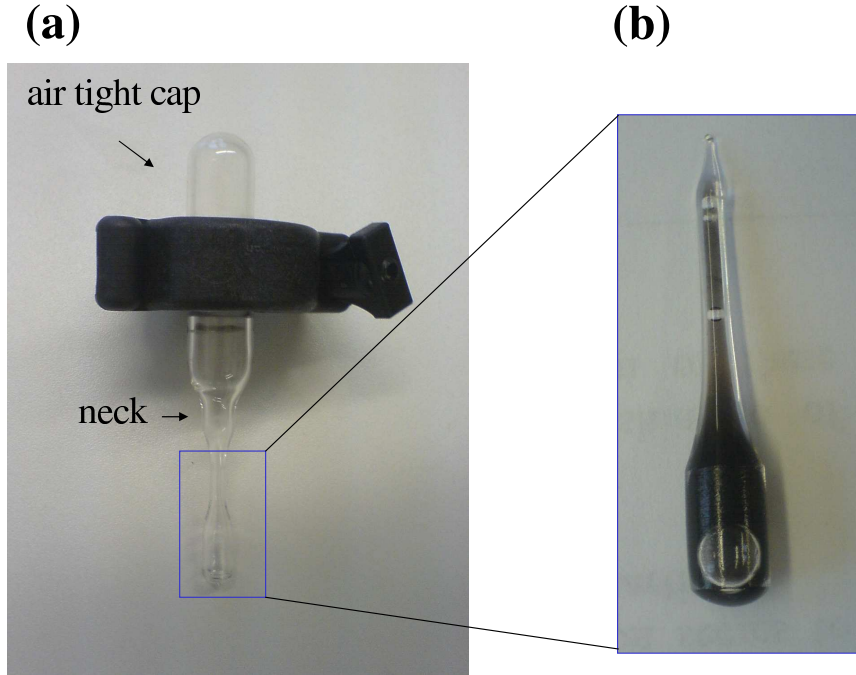


FIG. 42: The sample container design for SQUID measurement of Co nanoparticles: (a) air/liquid tight system for filling of the sample inside glove-box, (b) actual view of the sample container filled with Co nanoparticles solution.

due to magnetic impurity of conventional quartz which was used for constructing of the empty cell.

We would like to stress that the solution is concentrated (Co content is known from the sample preparation 50 mM/mL) thus the blocking temperature might be a result of inter-particle interactions. Due to the possible inter-particle interactions we did not perform the fit of the hysteresis loop with the Langevin function (see Section 3.1.2). For concentrated solutions, this procedure can give a misleading particle size and size distribution.

7.4. Structural properties

In order to examine the sample size and possible inter-particle interactions, small-angle x-ray scattering measurements were performed. We performed small-angle x-ray scattering experiments at the JUSIFA beamline of the DORIS storage ring at HASYLAB, Hamburg.

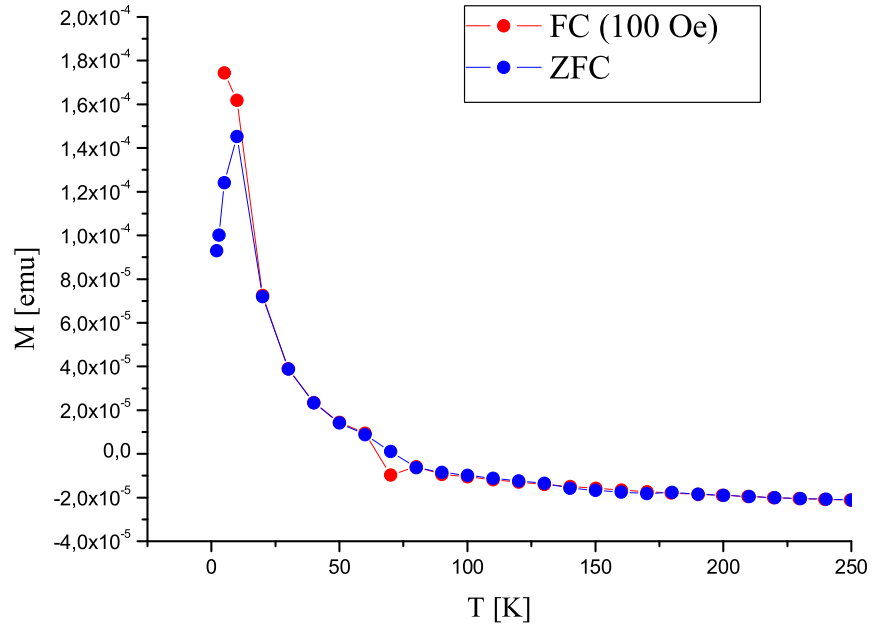


FIG. 43: The ZFC/FC measurement of the concentrated solution of Co nanoparticles.

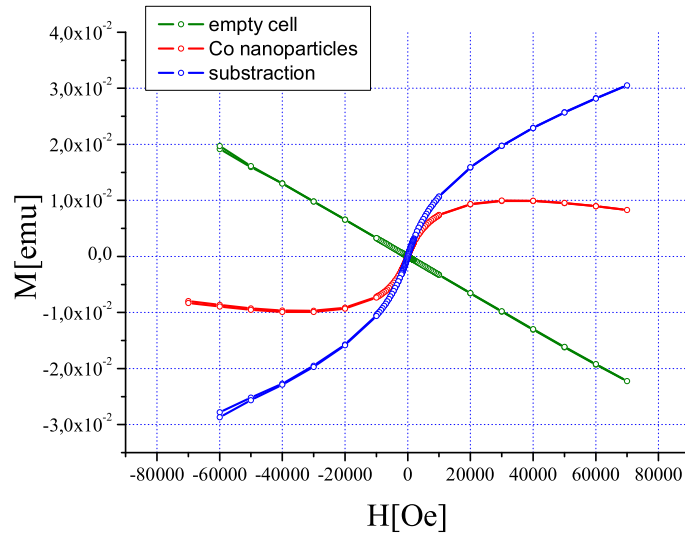


FIG. 44: The subtraction of the diamagnetic signal of the empty container from the signal of Co nanoparticles at 10K.

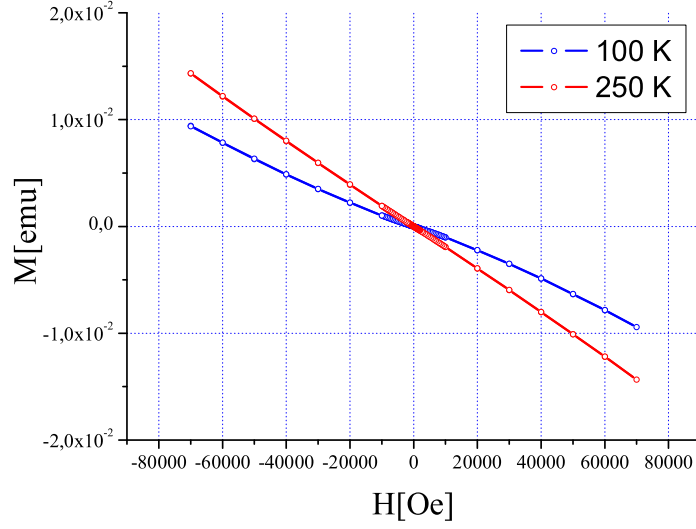


FIG. 45: The magnetization loop of Co nanoparticles in solution at high temperatures. The diamagnetic signal is due to the quartz sample container.

The advantage of using x-ray scattering for the preliminary characterization is the much higher contrast of Co nanoparticles in solution, compared to neutron scattering. The electron density profile for the Co nanoparticles covered with AOT ligand shell and dispersed in toluene is shown in Fig.48. The other advantage is that the x-ray flux at a synchrotron is much higher than the available neutron flux. Therefore, the measuring time is significantly reduced.

The scattering cross-sections in absolute units versus scattering vector Q are shown in Fig.49, after subtraction of the scattering from toluene. The two samples (named as Co-K and Co-G) contain the same amount of Co (10 mM/mL) were measured.

The difference between these two samples lies in different method of dilution. The inverse micellar solution of Co nanoparticles was diluted by factor 5 after the synthesis (Co-K). While for Co-G sample the Co(AOT)_2 solution was diluted first by factor 5 and then used in synthesis.

A refinement within the Beaucage's unified equation [94] was performed. The Beaucage's unified equation describes both the Guinier exponential and structurally limited power-law regimes without introducing new parameters beyond those used in local fits of Guinier

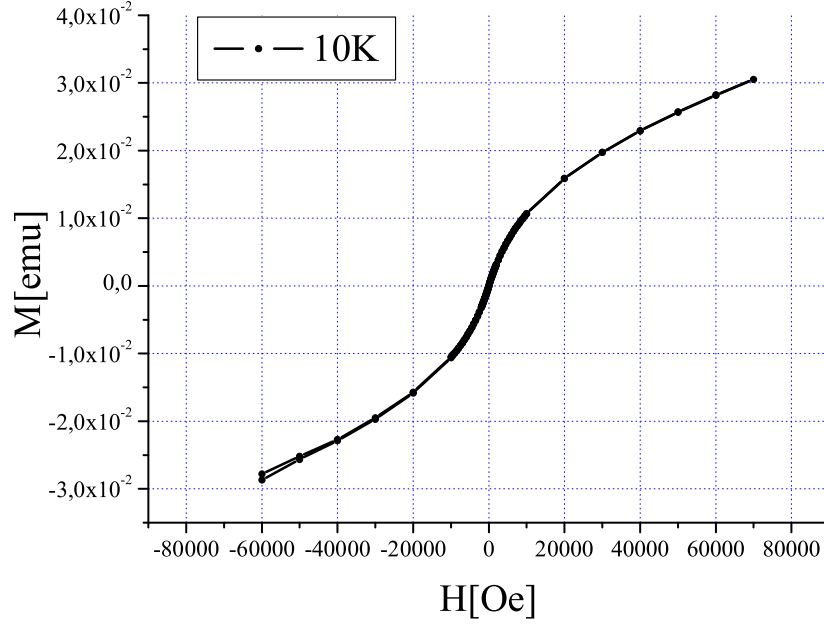


FIG. 46: The concentrated solution of Co nanoparticles at $T=10\text{K}$. The diamagnetic contribution of the quartz container is subtracted.

(low Q) and Porod (high Q) regimes. The unified equation describes a scattering over a wide range of sizes in terms of structural levels. One structural level pertains to a Guinier regime, describing an average structural size, and a power-law regime, describing the mass- or surface-fractal scaling for that structural level:

$$\frac{d\Sigma}{d\Omega} \simeq G \exp(-Q^2 R_g^2/3) + B(1/Q^*)^P \quad (105)$$

where, $Q^* = Q/[erf(kQR_g/\sqrt{6})]^3$, G is the Guinier prefactor defined above and B is a prefactor specific to the type of power-law scattering, P is the fractal dimension of the system, k is the empirical constant that has a value of 1 for steep power law decays, R_g is the radius of gyration (for spherical particles it is related to the real radius as follow: $R_g = \sqrt{\frac{3}{5}}R$).

The free parameters during fitting were G, B, P and R_g . The refinement yields particle diameters of $3.8(5)\text{nm}$ and $5.4(1)\text{nm}$, respectively. The fractal dimension obtained for both samples was $3 < P < 4$, which corresponds to the dimension of the surface fractals. It

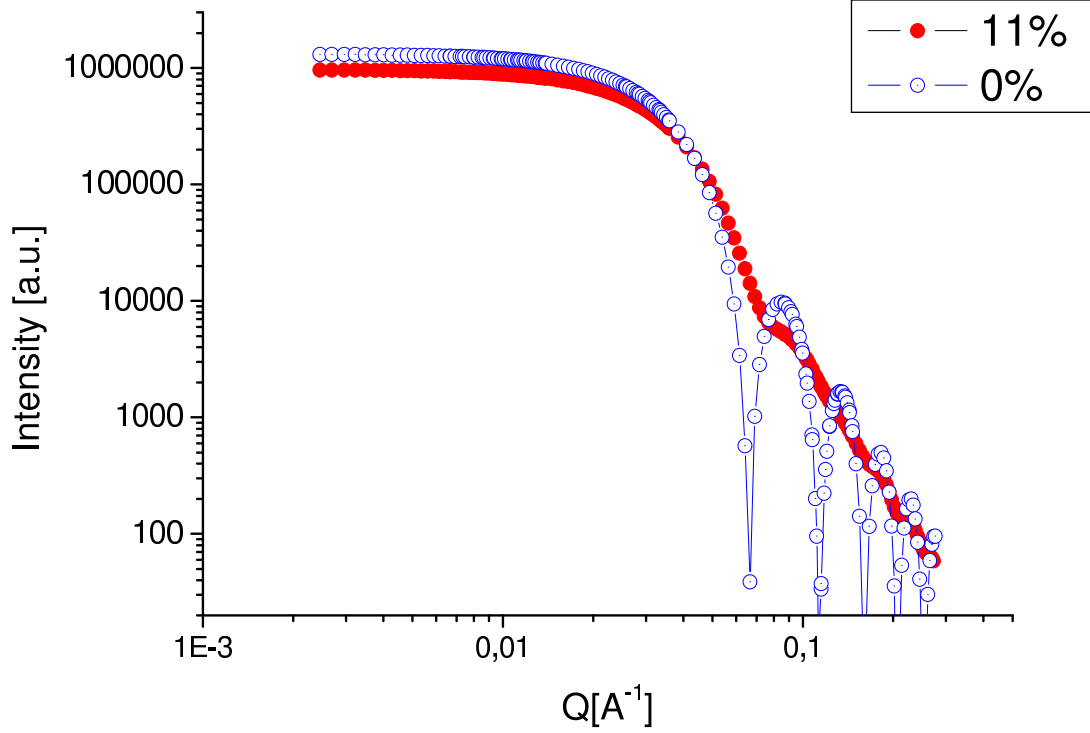


FIG. 47: The illustration of the effect of polydispersity on a small-angle scattering curve. Scattering from Co nanoparticles (dispersed in toluene) with a radius of 6.8nm and a size distribution of 0% and 11% is compared. The resolution is not taken into account.

seen from Fig.49 that the scattering curve of toluene is not flat at lower Q values due to the footprint of the primary beam or some parasitic scattering from the experimental setup. This affects the scattering curve of Co-G sample at low Q , because this sample scatters with a lower intensity compared to Co-K sample.

The deviation of the fitted curves at higher Q for both samples are due to the form factor which is beyond the scope of the Beaucage formalism. As we demonstrated in above sections, the form factor of the spherical nanoparticles manifest itself as a minimum in the scattering curve at higher Q . The Beaucage's unified equation describes only the power law behavior of the scattering curve at different Q values and it is not shape specific. Thus, the observed minimums for Co-K and Co-G cannot be fit within a frame of the Beaucage formalism. In order to fit the scattering curves a model describing the particle chemical and geometrical properties as well as possible inter-particles interactions has to be introduced.

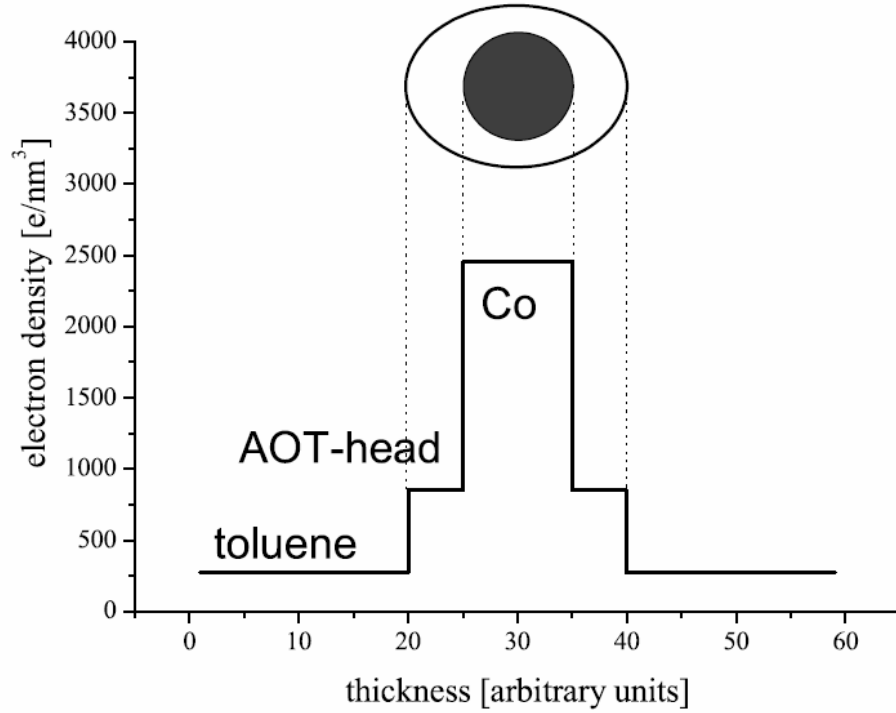


FIG. 48: The electron density profile for the Co nanoparticles dispersed on toluene.

7.5. Results and discussion

We have developed a new synthesis route for the production of stable Co nanoparticles with a diameter of about 4 nm. We could show that these particles are superparamagnetic with a blocking temperature of 10K.

The magnetic properties of the dilute samples Co-K and Co-G could not be measured with the available magnetometers and the available sample containers. Even at temperatures below 10K the diamagnetic signal of the quartz container was dominant. Only the magnetic signal of a five times more concentrated sample (Fig.46) could be reliably measured by a SQUID magnetometer. Therefore, the size extracted from the blocking temperature measurements cannot be compared with the size obtained by small-angle x-ray scattering, since inter-particle interactions cannot be excluded for the concentrated solution. However, we obtained clear evidence that the nanoparticles are magnetic. The magnetization of an individual nanoparticle should not depend on the level of dilution.

Due to the low contrast which Co nanoparticles display for conventional TEM it was not

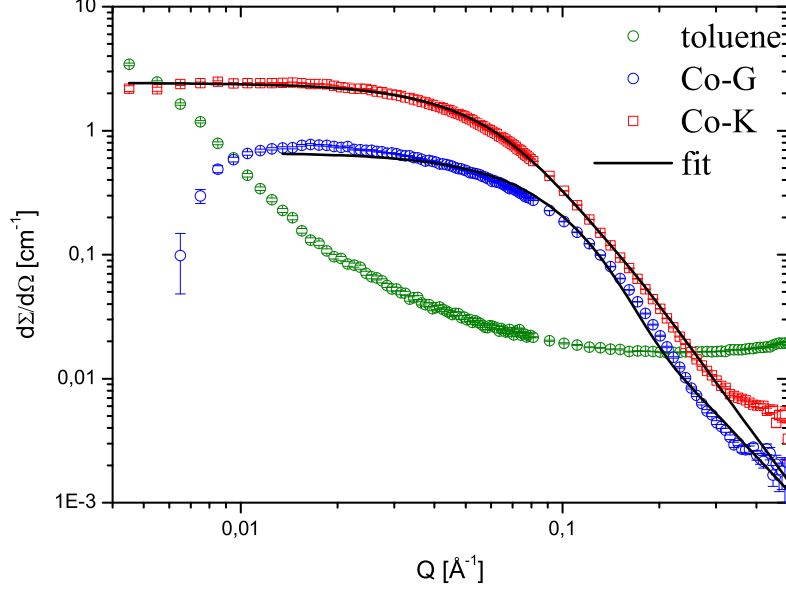


FIG. 49: The plot shows two curves for the Co nanoparticles in toluene (Co-K) and (Co-G) at $E = 7709\text{eV}$ and the scattering from toluene. The solid lines are the fits within Beaucage formalism [94].

possible to obtain the particle size distribution from electron microscopy. Moreover, the particles are covered with an AOT shell which decreases the contrast even more. Therefore, we applied the scattering methods to study the particle size.

Based on the small x-ray scattering data we can conclude the following. The scattering intensity of Co-G sample is lower compared to Co-K in the lower Q region. It is likely due to the fact that the Co-G sample is more dilute. The region at low Q is flat and displays the typical behavior of the form factor of spherical particles. The flatness of the curve in this region is a sign of an absence of the structure factor. However, it is hard to conclude since the fractal dimension is $3 < P < 4$. In case of non-interacting particles one should expect the fractal dimension $P = 4$, defining the Porod law at higher Q .

The refinement with Beaucage unified exponential/power law does not give any information on the contrast. Therefore, no conclusions on the chemical properties of the system can be made. It is just extended Guinier formalism combined with the Porod law, which gives an

information about an averaged particle size and hint on possible inter-particle interactions. No information considering the polydispersity can be delivered by this method.

The refinement of the scattering curve taking into account the core-shell model (see Fig.48) and possible inter-particle interactions has to be performed.

Due to the sample preparation one can expect the present of small aggregates of AOT micelles as well as NaAOT in the solution. Thus, the additional x-ray measurement has to be done on these solutions for a proper background subtraction.

8. OUTLOOK: FURTHER DEVELOPMENT OF TOPICS

In this section we will describe the further experiments for developing the topics which were the part of this work. Mainly, we will discuss the development of the topic concerning magnetization distribution within Co nanoparticles. The preliminary structural and magnetic characterizations are carried out and allowed us to optimize the parameters for successful polarized SANS experiment.

8.1. GMR properties of Fe/Cr/Fe trilayer and multilayer compared with x-ray data

Here, we propose to study the dependence of GMR effect on the structural parameters obtained by anomalous x-ray scattering. Since the electron scattering at the interface is responsible for GMR effect, the structural analysis of interfaces is the key for understanding the electron transport properties. The method we used gives a quantitative description of the interface morphology of the GMR trilayer. The further steps would be to study GMR effect dependence on the structural parameters for Fe/Cr tri- and multilayers.

However, with the present technique we cannot access the very small lateral correlation lengths in the order of a few nanometers. Since the electron mean free path is not μm but rather nm, these are the relevant length scales for the transport properties. The grazing incidence small-angle x-ray scattering is can be used in order to access smaller correlation lengths.

The structure of interfaces might be varied by changing the growing conditions, i.e. sputtering pressure, sputtering power, substrate temperature or by post-deposition treatments like ion irradiation and thermal annealing.

Similar studies were carried out by Ustinov et.al.,[95] and Paul et.al.,[54].

Ustinov et.al., used conventional CuK_α x-ray reflectometer to measure the specular reflectivity of $[\text{Fe}(20\text{\AA})/\text{Cr}(9\text{\AA})]_8$ multilayer grown by MBE. From the fits of the reflectivity using the Parratt formalism they obtained vertical rms interface roughnesses of Fe-on-Cr and Cr-on-Fe as a function of deposition temperature (see Fig.50). The magnetoresistance $r(H) = [R(H) - R(0)]/R(0)$ was measured as a function of growth temperature (Fig.51). They have claimed that both interface roughening and interdiffusion reduce the value of the GMR effect.

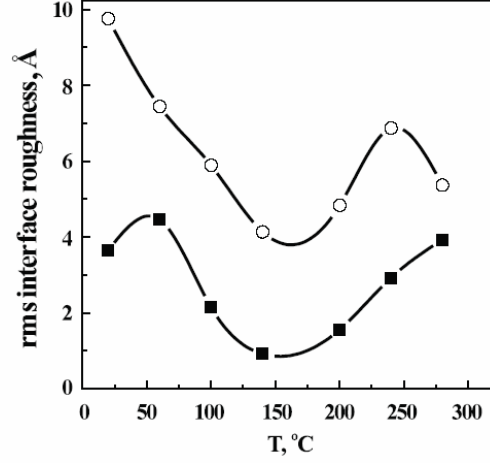


FIG. 50: Substrate temperature T dependence of vertical rms roughness at Fe-on-Cr (squares) and Cr-on-Fe (circles) interfaces in Fe/Cr multilayers deduced from x-ray data. Taken from [95].

In their work A.Paul et.al., investigated GMR effect in $[\text{Fe}(30\text{\AA})/\text{Cr}(12\text{\AA})]_{20}$ as a function of the substrate roughness, which they assume to govern the roughness of the Fe/Cr interfaces. The x-ray specular reflectivity and AFM measurements were carried out for the structural characterization of samples. The GMR value as a function of the substrate roughness obtained by AFM is shown in Fig.52.

Authors noticed that due to the low contrast between Fe and Cr in their refractive indices it is not possible to fit the reflectivity data to get reliable information. Therefore, only substrate roughnesses were investigated by AFM.

Here, we would like to propose the similar study accomplished by anomalous x-ray scattering for Fe/Cr tri-and multilayers. We demonstrated that the method is good enough to describe the interfacial properties of Fe/Cr/Fe trilayer. Varying the deposition temperature and measuring the value GMR effect we can correlate it with the structural data obtained by anomalous x-ray scattering. Therefore, the influence of the lateral correlation length and Hurst parameter can be an aim of future experiments. The fitting time of the off-specular intensity in case of multilayer will be significantly increased.

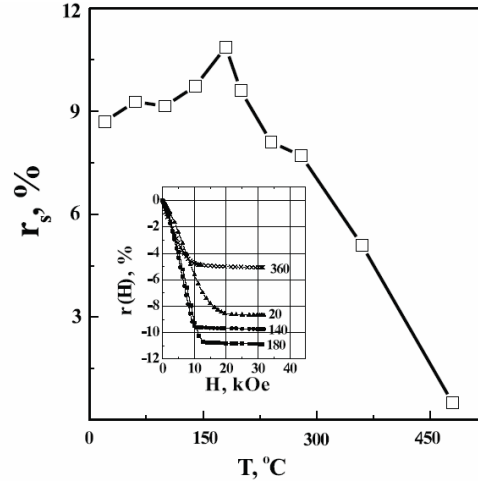


FIG. 51: The value of the giant magnetoresistance effect as a function of growth temperature. The insets show magnetic field dependencies of magnetoresistance in some multilayers grown at different temperatures. r_s is the saturation magnetoresistance value. Taken from [95].

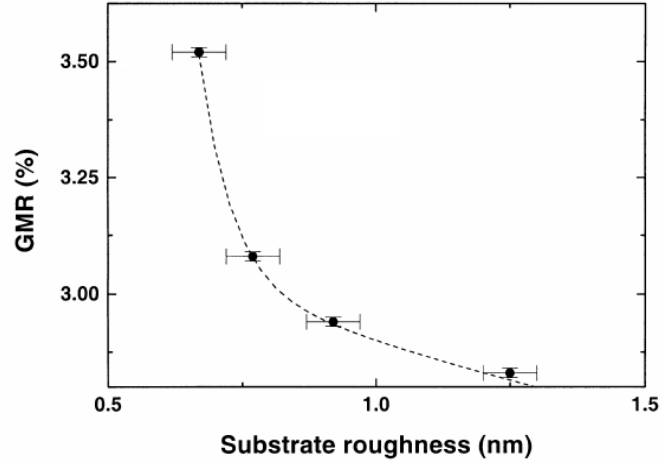


FIG. 52: Variation of percentage GMR with surface roughness of the substrates. Taken from [54].

8.2. Magnetic correlations in MnO nanoparticles

Here we will propose the polarized neutron measurements of MnO nanoparticles in confined geometry with high Q -resolution aiming to explore the magnetic correlation length within the sample.

Golosovsky et.al., [79] obtained the temperature dependence of the volume-averaged diameters D_{mag} and D_{nucl} from the width of the observed Bragg peak (see Fig.32). The diffraction peak is broadened compared to the instrumental resolution at low temperature indicating finite range correlations. D_{nucl} was assumed to be the same for all temperatures and kept to the peak width well above T_N . Therefore, the broadening of the peak at higher temperatures was attributed to the finite magnetic correlations. Both values were found significantly larger than the mean pore diameter of 70Å (see Fig.53). It is an indication that MnO forms a interconnected fractal-like structure rather than isolated particles.

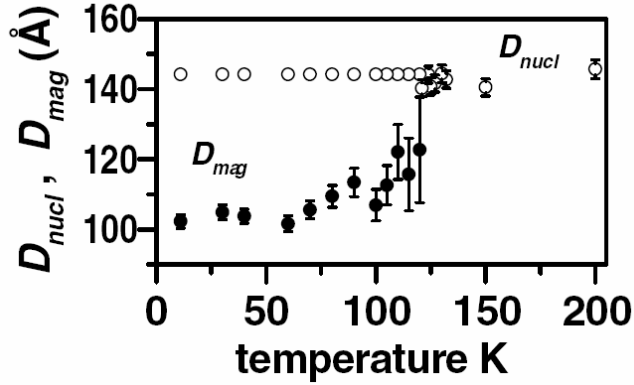


FIG. 53: Temperature dependencies of the volume-averaged diameters D_{mag} and D_{nucl} for the magnetic and nuclear regions, respectively, for MnO nanoparticles measured with unpolarized neutrons. Taken from [79].

The increase of D_{mag} with temperature is surprising, since it corresponds to an increase of the MnO domain size at higher temperatures.

Two interpretations have been given to explain the observed values of D_{mag} compared to an

average size of nanopores. The first in terms of a breakdown of the large magnetic aggregates into smaller ones caused by irregularities in porous glass. The other suggestion is the random canting of the surface spins in MnO nanoparticles.

In our work we obtained experimental evidences that spin-canting effect takes place for MnO nanoparticles. However, it was not possible to access the correlation lengths due to relatively low Q -resolution of DNS instrument. As one can see from Fig.54, the width of the two Bragg peaks for MnO powder is the same (1.7 deg.) at low and high temperatures. It means that for both cases we observed mainly the finite resolution of our instrument.

We propose to use an advantage of polarized neutron scattering with polarization analysis in order to study the width of the magnetic Bragg peak, with high Q -resolution (for example IN12 instrument at ILL). High resolution is necessary to determine the domain size of ordered MnO regions. With the polarization analysis there is no need to make an assumption about D_{nucl} and magnetic correlations will be probed directly. By this we will be able to examine the behavior of D_{mag} as a function of temperature more accurately.

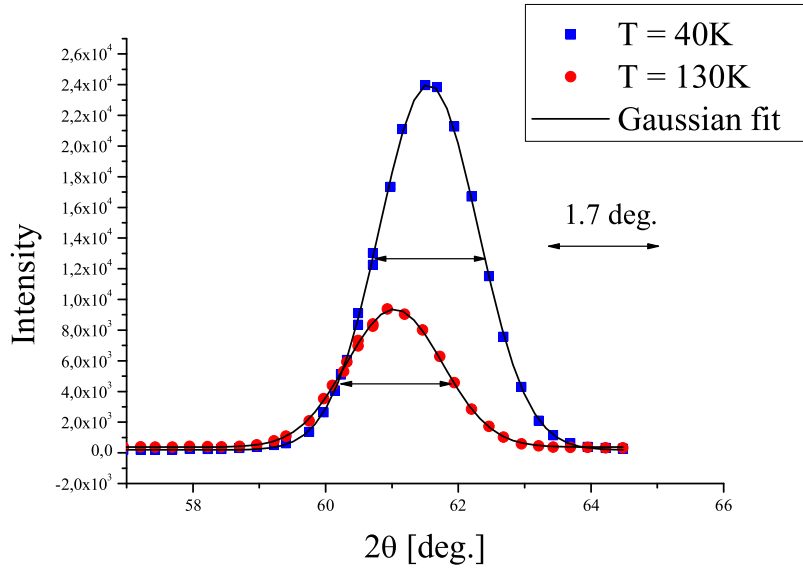


FIG. 54: The $(\frac{1}{2}\frac{1}{2}\frac{1}{2})$ Bragg peaks for the bulk MnO at $T = 40K$ and $T = 130K$, in the spin flip channel containing spin incoherent and magnetic scattering. The black solid lines are the fits with Gaussian function.

8.3. Polarized neutron measurements of Co nanoparticles in solution

In this section we will discuss how the small-angle polarized neutron scattering measurements on Co nanoparticles can be performed in order to study the spin-canting effect. Based on the structural information obtained for our sample by small-angle x-ray scattering we simulated the corresponding polarized neutron cross-sections. We kept the same concentration in our simulations, while the size of the particles was increased up to 4nm in radius. At the moment we are able to produce the Co nanoparticles with a radius of about 2nm. However, for such small particles the spin-canting effect will be difficult to observe, due to the similar size of the core and the shell. This is the reason we used larger particles in our simulations. The experimental observation of the spin-canting effect by means of polarized neutrons is a non-trivial task and samples themselves as well as instrumentations have to meet the special demands. The demands on instrument are discussed on example of small-angle neutron scattering instrument KWS-2 located in Munich.

First let us recall the equation describing the scattering cross-section (in cm^{-1} units) for small-angle polarized neutron scattering (see Section 4.2)

$$\frac{d\Sigma}{d\Omega}(Q) = n_p \int_0^\infty D(R) F^2(QR) S(Q) dR \quad (106)$$

where, n_p is the number of particles per unit volume, $F(QR)$ and $S(Q)$ are the form and structure factors, respectively, $D(R)$ is the size distribution function.

The form factor for magnetic Co nanoparticles surrounded by non-magnetic organic shell and dispersed in solvent is described in terms of the core-shell model:

$$F_{core-shell}(QR) = (\rho_c - \rho_s) V_c f(QR_c) + (\rho_s - \rho_{sol}) V_t f(QR_t) \quad (107)$$

where, $\rho_c = \rho_N \pm \rho_M$ is the spin dependent SLD of magnetic Co nanoparticles and $\rho_c - \rho_s, \rho_s - \rho_{sol}$ are the core/shell and shell/solvent contrasts, respectively. $V_c, V_s, V_t = V_c + V_s$ are the volumes of the core, shell and the total volume of a particle, with radius R_c, R_s and $R_t = R_c + R_s$, respectively.

In this section we will assume the simplest case when no interactions between the particles exist, i.e. $S(Q) = 1$. Therefore, a dilute solution of Co nanoparticles has to be chosen, because it reduces the number of unknown parameters in modelling the SANS cross-sections. It is seen from eq.(106) that the cross-section depends on SLD contrast, size and concentration of the particles. These three parameters have to be adjusted in order to perform

successful polarized SANS experiment.

8.3.1. Background due to incoherent scattering

In every neutron scattering experiment the signal-to-background ratio is crucial. Regardless of the origin of the background, the ratio has to be sufficiently large to obtain reliable experimental data. For small-angle scattering it is important that the scattered intensity of Co nanoparticles is at least one order of magnitude larger than the scattering from the solution. In a typical experiment one measures separately the scattering from the Co nanoparticles in solution and from the solution itself in order to subtract and separate off the scattering from the Co nanoparticles.

Only coherently scattered neutrons carry the information about the sample. In SANS incoherent scattering from hydrogen manifests itself as an isotropic background signal. This can be a problem if there is too much hydrogen in the sample since hydrogen has a much larger incoherent neutron scattering length (25.3fm) than most of other common nuclei (i.e. for Co it is -6.2fm).

On the other hand the large difference in coherent scattering length between hydrogen (-3.74fm) and deuterium (6.6fm) allows one to vary the contrast in solution by mixing deuterated and protonated materials. Thanks to contrast variation the scattering problem can be significantly simplified. An example of the contrast variation is shown in Fig.55., where the SLD of d-hexane was reduced by h-hexane in order to match SLD of AOT ligand shell. In this case the second term in the core-shell form factor vanishes (eq.107) and it reduces to a simply core form factor. This method is commonly used in soft-matter physics when one sample is measured with different contrasts and the data are fitted simultaneously with the same structural parameters.

The incoherent scattering is a concern for our samples where the particles are covered with AOT ligand shell which already contains a large amount of hydrogen: $C_{20}H_{37}SO_7$. Thus, the contrast matching by protonating d-hexane (or d-toluene) has to be carefully studied. There is no simple way to calculate this incoherent background and usually it is measured experimentally [96]. Maconnachie [97] has shown that the incoherent scattering

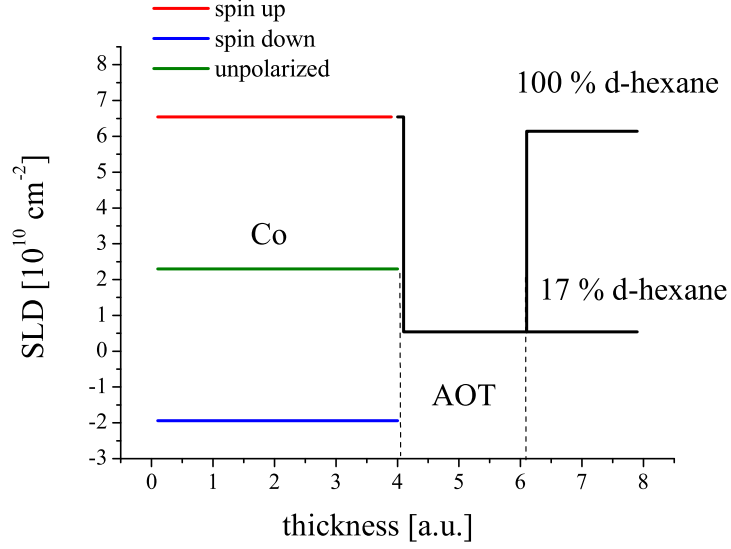


FIG. 55: Contrast variation of Co nanoparticles in solution at saturation magnetic field. The x-axis scale is exaggerated for visualization.

is anisotropic and the cross-section is temperature- and wavelength-dependent. Therefore, the first experiment would be to measure the incoherent contribution from AOT micelles dispersed in different mixture of d-hexane and h-hexane in order to estimate the background. Based on these measurements one could perform the simulation of SANS intensity expected from the particles and estimate signal-to-background ratio for different contrasts. It might happen that for our samples described in Section 7 some of the contrasts will be irrelevant due to the small signal-to-background ratio.

We would like to note that in case of polarization analysis the non-magnetic background can be separated. It will lead to significant increase of the measuring time which may not be accessible in neutron facilities.

To overcome the background problem the concentration and size of the particle has to be adjusted. Of course, the limit of concentration exists above which the particles can not be considered any longer as non-interacting or they will agglomerate.

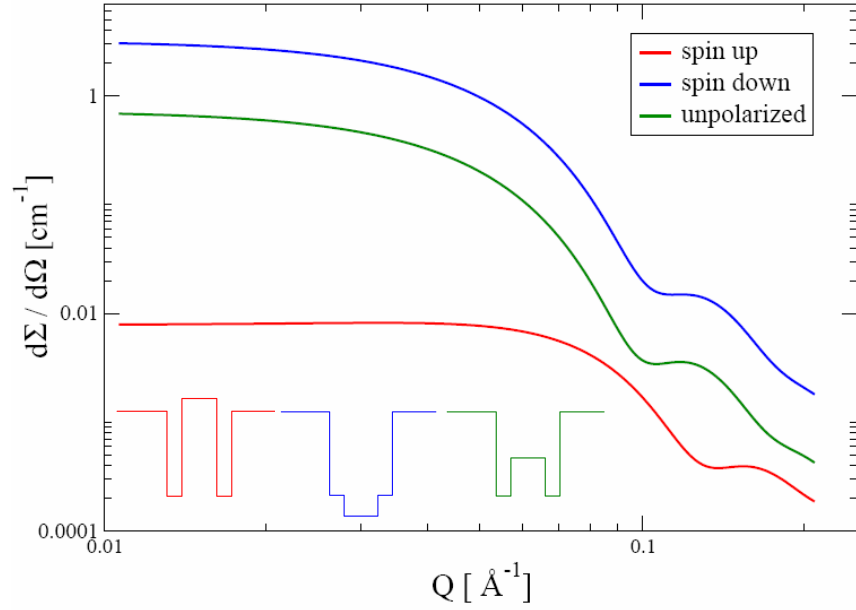


FIG. 56: Simulations of polarized neutron scattering from the saturated Co nanoparticles dispersed in d-hexane. Concentration was taken from the SAXS experiment ($n_p=3.5 \cdot 10^{15}$ and $R = 4\text{nm}$), with the polydispersity of 15% and $\lambda = 4.5\text{\AA}$. The resolution function is neglected. The inset presents the SLD contrast for unpolarized, spin up and spin down neutrons.

8.3.2. Required Q -range

The other aspect of successful SANS experiment lies in the Q -range needed to observe form factor minima. This problem is related to the particle size and experimental setup. For smaller particles a larger Q -range is needed to observe the minima. Therefore, it is important to estimate the Q -range necessary for our samples. It is already seen from SAXS measurements (see Fig.49) that all scattering features are in Q -range $0.01 - 0.4\text{\AA}^{-1}$. In order to explore the necessary Q -range of our samples in case of polarized SANS and demonstrate the contrast variation due to different contrast for spin-up/spin-down neutrons we performed simulations of the scattering curves (Fig.56).

In simulations we assumed non-interacting Co nanoparticles with $R = 4\text{nm}$ and polydispersity of 15% at saturation magnetic field. The concentration was obtained from the SAXS data and the particle size was increased compared with the existing sample. Spin canting effects are neglected, and we assume that all spins perfectly align along an external magnetic field.

Based on this simple simulation curve we can conclude that the following SANS instruments are suitable for our samples: KWS-1,2 (FRM-2, Munich), SANS 1,2 (SINQ, PSI), V4 (HMI)

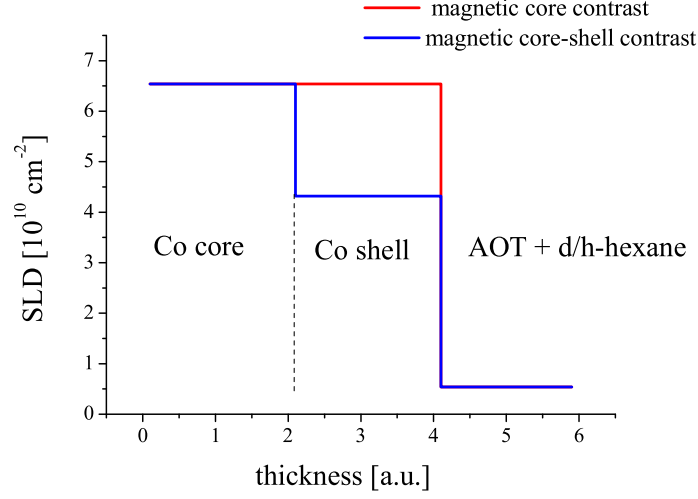


FIG. 57: The SLD contrast for spin up neutrons of Co nanoparticles dispersed in d/h-hexane at saturation for the ideal core and for the of magnetic core-shell model. The x-axis scale is exaggerated for visualization.

and D22 (ILL).

8.3.3. Resolution effects

The other important issue is the ability of SANS instrument to resolve the minima positions. To estimate this instrumental effect a resolution function has to be calculated.

The calculation of the resolution function is given by J.S.Pedersen et.al.,[98]. It takes into account the smearing effects due to the wavelength spread, finite collimation of the beam and detector resolution.

The measured intensity is the convolution of the sample cross-section and the resolution function:

$$I(\mathbf{Q}_0) = \int_{-\infty}^{+\infty} R(\mathbf{Q}\mathbf{Q}_0) \left(\frac{d\Sigma}{d\Omega}(\mathbf{Q}) \right) d^3\mathbf{Q} \quad (108)$$

where, $\frac{d\Sigma}{d\Omega}(\mathbf{Q})$ is the scattering cross-section, $R(\mathbf{Q}\mathbf{Q}_0)$ is the combined resolution function, \mathbf{Q}_0 is the scattering vector corresponding to the setting of the instrument. The radiation

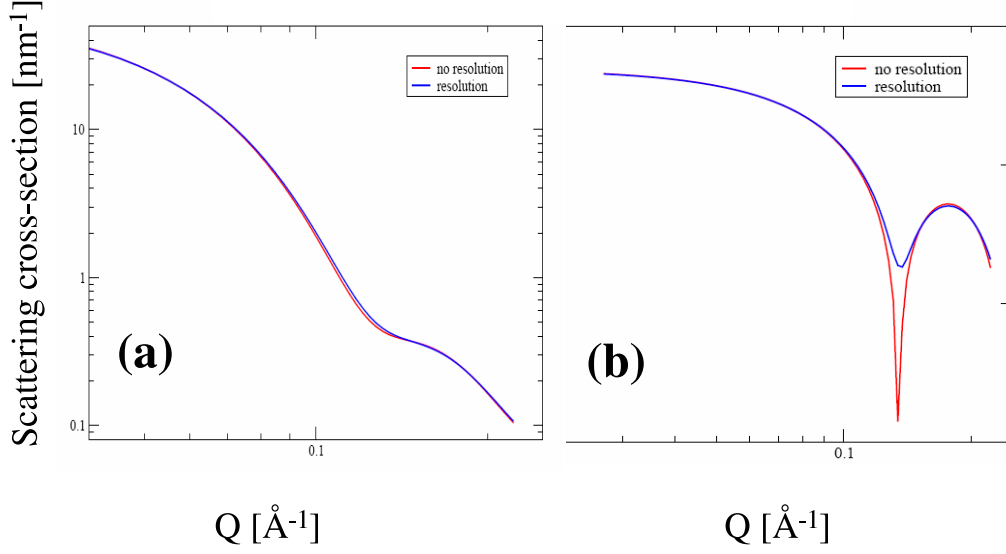


FIG. 58: The combined resolution function σ_Q^2 effect on (a)polydispersity (15%) (b) monodisperse Co nanoparticles. In the calculation of the resolution function we assumed the following parameters: $\Delta\lambda/\lambda = 0.1$, the detector-to-sample and the collimation distances were 2 meters.

with \mathbf{Q} scattering vector (in the range of \mathbf{Q}_0) also contributes to the scattering due to the spread of wavelength and finite collimation.

The combined resolution function is written as

$$R(\mathbf{Q}\mathbf{Q}_0) = \frac{Q}{\sigma_Q^2} \exp\left(-\frac{Q^2 + Q_0^2}{2\sigma_Q^2}\right) \mathfrak{S}_0\left(\frac{QQ_0}{\sigma_Q^2}\right) \quad (109)$$

with $\mathfrak{S}_0\left(\frac{QQ_0}{\sigma_Q^2}\right)$ is the modified Bessel function of the first kind, and

$$\sigma_Q^2 = \frac{1}{8\ln 2} \left[Q^2 \left(\frac{\Delta\lambda}{\lambda} \right) + k_0^2 \Delta\Theta^2 \right] \quad (110)$$

Here we neglect the detector resolution (which is the case for KWS-2 instrument) and the resolution function for radial averaged data.

The combined resolution function acts differently on mono- and polydisperse nanoparticles. The effect of the resolution is shown for Co nanoparticles with different polydispersity (Fig.58). The resolution effect is smearing out of the minimum for monodisperse nanoparticles, while in case of polydispersity the effect is minor.

8.3.4. *Simulations of the spin-canting effect*

In this section we will present simulations of the polarized neutron scattering cross-section for Co nanoparticles with the non-uniform magnetization distribution within a single nanoparticle. The challenges of the experimental observation of this effect are discussed based on the simulations.

As an example we simulate the simplest case when the particles are in the core contrast (i.e. SLD of solvent matches SLD of AOT ligand shell). The scattering problem becomes simple due to the fact that only one type of scatter is present. For the contrast matching the mixture of 83% of h-hexane and 17% of d-hexane was used (see Fig.57). We would like to note that this contrast might not be relevant for the real scattering experiment due to large amount of hydrogen. The core contrast can be also achieved by deuteration of AOT shell, but this product is not commercially available up to now.

Within the core contrast describing the contrast between Co nanoparticles and surrounding medium we introduced so-called "magnetic core-shell contrast". This describes the situation where the magnetic nanoparticles have a magnetically ordered core and a disordered shell. To take into account this effect we simply reduced magnetic SLD of the magnetic shell by factor of 2 (see Fig.57). The nanoparticles are assumed to be saturated in an external magnetic field. The radius of the core is 3.6nm and the radius of the shell is 0.6nm, according to the thickness of one atomic layer for fcc-Co [99]. In simulations we assume that only one atomic layer is magnetically disordered at the saturation field. Of course such a step-like profile will not reflect the real magnetization profile as it was observed in case of MnO nanoparticles in porous glass (see Section 6). But our model is good enough to demonstrate the sensitivity of polarized SANS measurements to the spin-canting effect.

Our samples provide the highest contrast for spin up neutrons. Thus, we performed the simulations of the spin up neutron intensity (Fig.59) for the particles with no spin-canting effect, and with spin-canting effect assuming the corresponding contrasts for each case (Fig.57). We assume the same polydispersity of 15% for both cases and neglected resolution effects. As we have shown already they are negligibly small for the particles with polydispersity of 15% (see Fig.58).

As one can see the spin-canting effect manifests itself in a slight shift of the minima to the lower Q -range. We would like to emphasize that simulations do not take into account the

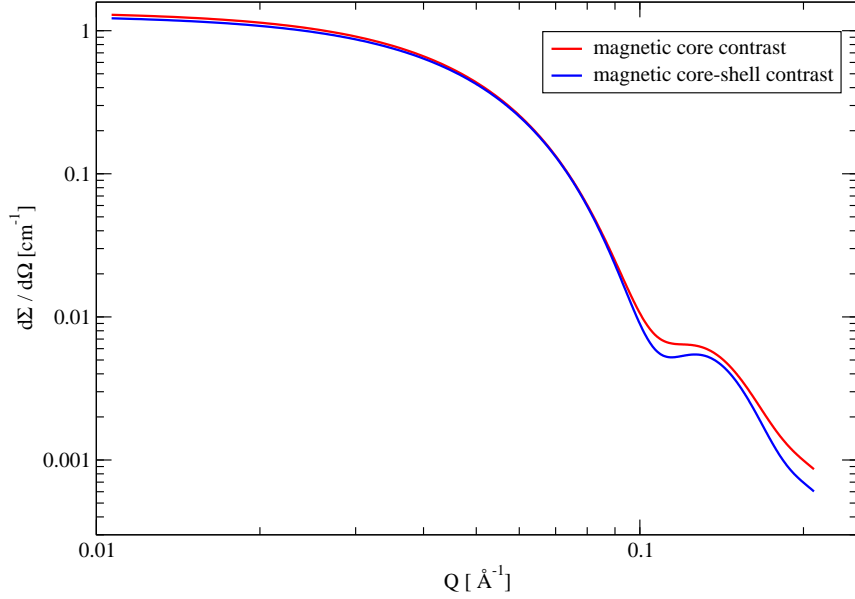


FIG. 59: The differences in scattering curves for the magnetic core and magnetic core-shell contrast. The contrast for both cases is shown in Fig.57.

experimental standard deviations due to the counting statistics. They depend on the measuring time and the experimental setup used, therefore they cannot be reliably simulated. The effect is more pronounced for the particles with polydispersity below 10%, due to more number of minimums resolved (Fig.60).

By this simulation we demonstrated that even such a sharp magnetic contrast results in small changes in the scattering curve. We assume that the combined resolution function is known and its effect can be de-convoluted from the data.

If it is impossible to achieve the prefect core contrast for Co nanoparticles due to large incoherent background the deuterated solvent has to be used. This will modify the contrast and form factor describing the magnetic core-shell and non-magnetic core-shell contrast at the same time has to be introduced.

The other challenge would be to describe more complicated magnetization profile within a single Co nanoparticle apart from the simplest step-like profile. In reality one should expect the smoother transition in magnetization profile from core to shell. The more realistic model which takes into account size-dependent transition is so-called "cap and gown" model [100]. The model takes into account uniform core (cap) and shell (gown) with decaying density

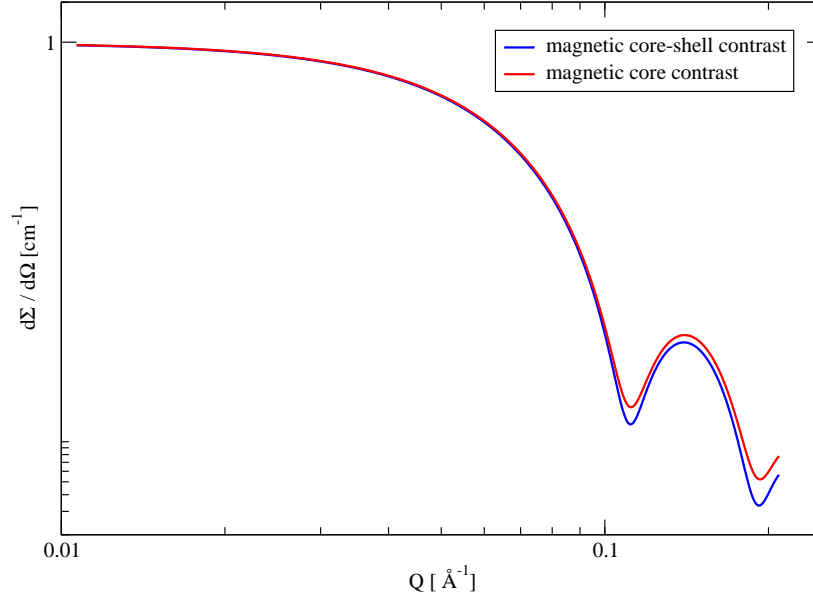


FIG. 60: The spin up scattering curve for the same particles as in Fig.59, but with polydispersity 7%.

profile of width σ :

$$\rho(r) = ke^{r^2/\sigma^2} \quad (111)$$

where, k is the constant proportional to excess SLD, r is the radial distance from center to surface of a particle. It would be simple assumption where the SLD profile exponentially decays from the magnetic core to shell.

The other important modification of the scattering curve might come from the surface roughness of the Co nanoparticles. These roughnesses of the surface can be taken into account by Debye-Waller factor $e^{-(\sigma_s Q)^2/4}$ [101]. The influence of the surface roughness on a scattering curve is shown in Fig.61. To accomplish the neutron scattering data the contrast variation using anomalous x-ray scattering (ASAXS) can be used as for Fe/Cr/Fe trilayer. Measurements at different energies close to the K-edge of Co allow the separation of the scattering contribution of Co from all other contributions.

Therefore, only a combined study using the polarized SANS in the core contrast for the magnetization profile and ASAXS for the structural information will provide the full structural and magnetic information about Co nanoparticles dispersed in solution.

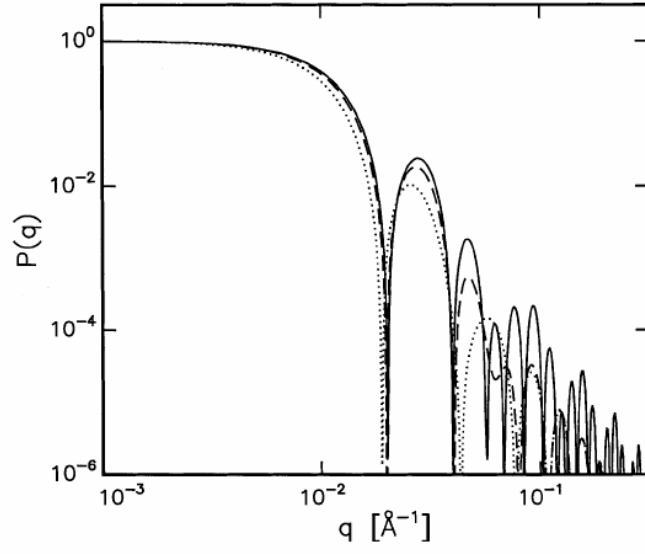


FIG. 61: The form factor of a shell modified by the Debye-Waller factor. The parameters are $R_{core} = 200\text{\AA}$, $R_{shell} = 100\text{\AA}$, and $\sigma_s = 0, 25, 50\text{ \AA}$ for the full, broken and dotted curve, respectively. Taken from [101].

APPENDIX A: SCATTERING LENGTH DENSITY AND ELECTRON DENSITY

The nuclear SLD of one molecule of component i is calculated as

$$\rho_N = \sum_i^N b_i^{coh} \frac{DN_A}{M} \quad (\text{A1})$$

Here b_i^{coh} is the coherent scattering length of atom i , N is the total number of atoms in the molecule, D is the bulk density, M is the molar mass of component i and N_A is Avogadro's number.

The magnetic part of the SLD was obtained experimentally at saturation magnetic field.

The electron density contrast for x-ray small-angle scattering was calculated as follow:

$$\rho = \frac{N_e N_A D}{M} \quad (\text{A2})$$

where, N_e is the number of electrons.

TABLE IX: The nuclear (ρ_N) and magnetic (ρ_M) SLD. The coherent scattering lengths are taken from [102]

material	$b^{coh}[10^{-13}\text{cm}]$	D[h/cm ³]	$\rho_N[10^{10}\text{cm}^{-2}]$	$\rho_M[\text{cm}^{-2}]$
Cr	3.63	7.10	2.99	
Fe	9.45	7.86	8.09	5.12
Co	2.49	8.90	2.30	4.24
Ag	5.92	10.5	3.50	
H ₂ O	-1.68	1.000	-0.56	
D ₂ O	19.15	1.107	6.30	
h-hexane (C ₆ H ₁₄)	-12.45	0.659	-0.56	
d-hexane (C ₆ H ₁₄)	133.31	0.767	6.14	
h-toluene (C ₇ H ₈)	15.66	0.865	0.94	
d-toluene (C ₇ D ₈)	99.91	0.943	5.67	
AOT (C ₂₀ H ₃₇ SO ₇ -)	38.11	0.990	0.544	

TABLE X: The electron density for some materials used in small-angle x-ray scattering.

material	N_e	$\rho[\text{e}/\text{nm}^3]$
Co	27	2455.18
H ₂ O	10	333.63
D ₂ O	10	332.82
h-hexane (C ₆ H ₁₄)	50	230.25
d-hexane (C ₆ H ₁₄)	50	230.28
h-toluene (C ₇ H ₈)	50	258.38
d-toluene (C ₇ D ₈)	50	281.68
AOT (C ₂₀ H ₃₇ SO ₇)	229	327.12

APPENDIX B: CALCULATION OF THE PEAK-TO-BACKGROUND RATIO FOR MAGNETIC BRAGG PEAK AT LOW TEMPERATURE

Here we discuss in more details how we estimated the number of disordered atoms in the MnO nanoparticle. The proper weighing factor has to be taken into account before an estimation.

We would like to point out the main difference between a single crystal and powder diffraction. In a powder a large number of crystallites are randomly oriented. Thus, it is not possible to see individual diffraction spots as in the single crystal diffraction experiment. In contrast to the single crystal diffraction, one observes rings of diffracted intensity (Debye rings) on a flat screen instead of sharp diffraction spots (see Fig.62). Assuming that diffracted intensity is distributed evenly around the base of each cone there is usually no need to measure the intensity of entire Debye ring. In conventional powder diffraction experiment the intensity is measured along a narrow rectangle centered at the circumference of the equatorial plane of the Ewald's sphere.

Let us stress again that in the powder diffraction experiment the three dimensional information of the reciprocal space of a crystal is collapsed into a one dimensional diffractogram. Therefore, for a proper estimation of the total scattered intensity one needs to introduce a weighting factors to the measured intensity.

In order to take into account the total intensity which is distributed on the surface of the

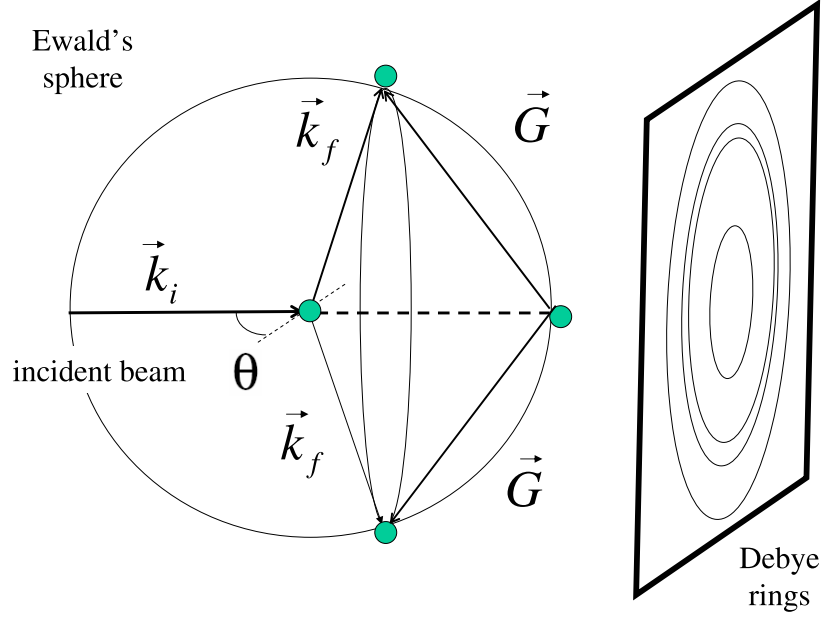


FIG. 62: The powder diffraction cone is schematically shown. The Bragg reflections occur when $\mathbf{Q} = |\mathbf{k}_f - \mathbf{k}_i| = \mathbf{G}$, where \vec{G} is vector of the reciprocal lattice. On the right side a number of Debye rings resulting in the real space from the different cones are shown on the flat screen.

sphere we should multiply intensity at this Q by the Lorentz factor (LF) for the powder [103]:

$$I_{tot} = \frac{1}{LF} I_{mes} \quad (\text{B1})$$

Basically, this factor is a modification of the well known Lorentz factor for the single crystal $1/\sin 2\theta$ which arises from the fact that the irradiated area of a crystal volume element changed as the diffraction angle is varied.

The Lorentz factor for powder accounts the following effects related to the diffraction from randomly oriented grains and the experimental geometry:

- number of grains contributing to the diffracted intensity ($\sim \cos \theta$)
- fraction of the Debye ring measured by the detector ($\sim 1/\sin 2\theta$)

Due to the geometry of the experimental setup only a certain number ΔN of powder grains will contribute to the measured intensity. The normals to the reflecting planes are distributed within a small stripe as it is shown in Fig.63. The fraction of these grains is proportional to the ratio between a stripe of the width $k\Delta\theta$ (where, $k = k_i = k_f$) and the total surface of

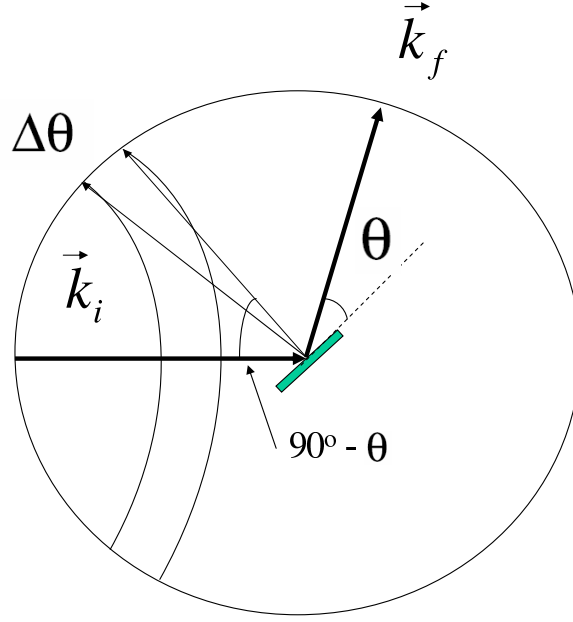


FIG. 63: The illustration of the grain orientation effect. The orientation of some grains lead to the diffraction which cannot be detected with the given experimental setup.

the Ewald's sphere. The area of the stripe is then the width $k\Delta\theta$ multiplied with its length $2k \sin(90^\circ - \theta)$, leading to

$$\frac{\Delta N}{N} = \frac{k\Delta\theta 2\pi k \sin(90^\circ - \theta)}{4\pi k^2} \sim \cos \theta \quad (\text{B2})$$

where, N is the total number of grains.

In our experiment only a part of the Debye ring was measured. The total intensity is then defined as a ratio between this part (ΔW) and the total length of the Debye ring, i.e. $\Delta W/k \sin 2\theta \sim 1/\sin 2\theta$. Therefore, the Lorentz factor for the powder is written as

$$LF = \frac{1}{4 \sin^2 \theta \cos \theta} \quad (\text{B3})$$

In Fig.64 the measured intensity multiplied by $\sin^2 \theta \cos \theta$ is shown as a function of Q . We note that the constants used in Lorentz factor are unimportant, since we are interesting in peak-to-background ratio.

For the proper estimation of peak-to-background ration we have to take into account only this background and the peak intensity which are coming from the first Brillouin zone. We can calculate exactly the volume of the first Brillouin zone for MnO fcc lattice with a lattice constant $a = 4.44\text{\AA}$ [11]:

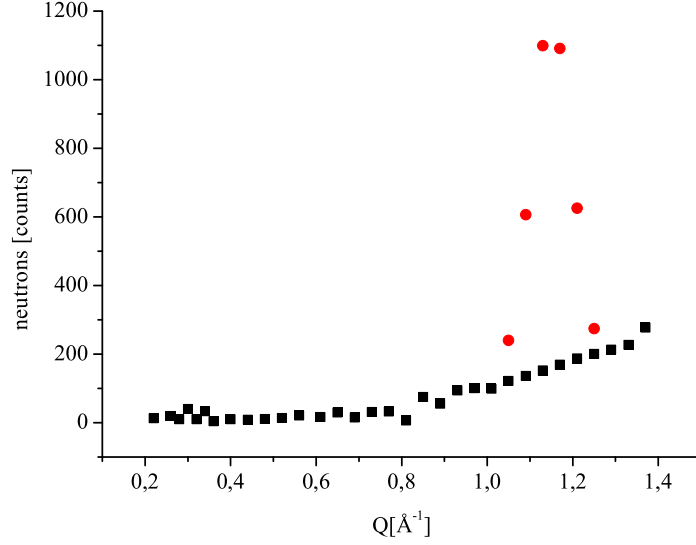


FIG. 64: The scattered intensity of the magnetic Bragg peak within the first Brillouin zone multiplied by $\sin^2 \theta \cos \theta$. The filled circles are the peaks points, the filled squares are the background points.

$$V_{1BZ} = 4 \left(\frac{2\pi}{a} \right)^3 = 11.4 \text{Å}^{-3} \quad (\text{B4})$$

Then we can assume a sphere with a volume equals to the volume of the first Brillouin zone, i.e.

$$\frac{4\pi}{3} Q^3 \approx V_{1BZ} \quad (\text{B5})$$

this corresponds to $Q = 1.4 \text{Å}^{-1}$. Thus, we have to assume a background coming from this Q -range. Because a half of the magnetic peak belongs to the first Brillouin zone and we have to take into account the background within the same zone. Therefore, the area below the peak (here, integrated intensity) has to be divided by 2. It schematically shown in a simplified 2-dimensional case that $(\frac{1}{2}, \frac{1}{2})$ reciprocal lattice point is situated on the border between the first and the second Brillouin zone (see Fig.65). The figure is might be misleading, because in reality we deal with 3-dimensional unit cell. However, it is fairly good to explain that only half of the peak belongs to the first Brillouin zone. Then we did the estimation of the peak-to-background ratio in several steps. First, we calculated the integrated intensity of

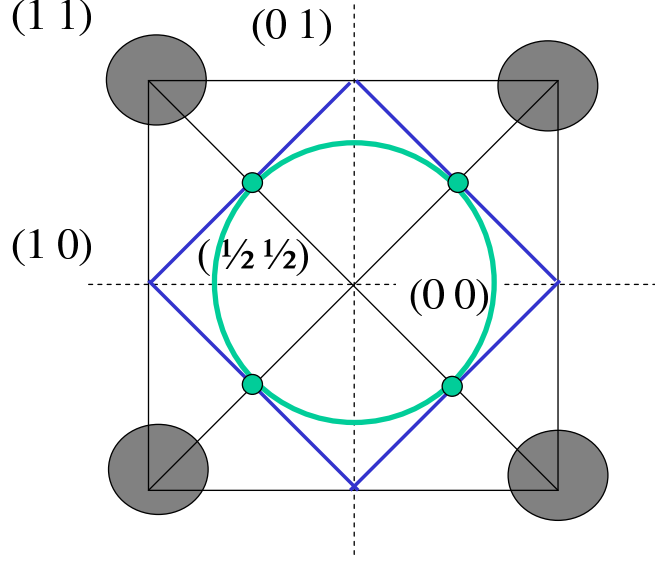


FIG. 65: The first Brillouin zone (blue curves) in 2-dimensional case of fcc lattice. The $(\frac{1}{2} \frac{1}{2})$ reciprocal point is on the edge between the first and the second zone.

the peak which belongs to the first Brillouin zone:

$$S_{1BZ}^{peak} = \frac{(S_{total} - S_{bkg})}{2} \simeq 58.1 \quad (B6)$$

where, S_{total} is the total integrated intensity related to the first Brillouin zone, S_{bkg} is the background integrated intensity related to the first Brillouin zone (below $Q = 1.4 \text{\AA}^{-1}$). We omitted the units in eq.(B6) due to the ratio which will be calculated. Second, we calculated the peak-to-background ratio

$$r = \frac{S_{bkg}}{S_{1BZ}^{peak}} \simeq 61\% \quad (B7)$$

It means that 61% of atoms in a nanoparticle are disordered due to the possible interaction with glass walls and cannot be described in the frame of our model.

APPENDIX C: THE LIST OF THE FREQUENTLY USED SYMBOLS AND ABBREVIATIONS

- *GMR* - Giant magnetoresistance
- *AFM* - antiferromagnetic
- *FM* - ferromagnetic
- T_N - Néel temperature
- T_C - Curie temperature
- *MTJ* - magnetic tunnel junction
- *TMR* - tunnelling magnetoresistance
- *MRAM* - magnetic random access memory
- *RT* - room temperature
- *NP* - nanoparticle
- *TEM* - tunneling electron microscope
- k_B - Boltzmann constant
- T_B - blocking temperature
- *ZFC* - zero-field cooled
- *FC* - field cooled
- *SLD* - scattering length density
- *SANS* - small-angle neutron scattering
- *SANSPOL* - polarized small-angle neutron scattering experiment with no analysis of the polarization of the scattered neutrons
- *POLARIS* - polarized small-angle neutron scattering experiment with analysis of the polarization of the scattered neutrons

- NSF - non-spin flip
- SF - spin-flip
- m_n - mass of neutron
- $\mathbf{k}_i, \mathbf{k}_f$ - initial and final neutron wave vectors, respectively
- $MOKE$ - magneto-optical Kerr effect
- μ_N - nuclear magneton
- μ_n - neutron magnetic moment
- $\hat{\mu}$ - neutron magnetic moment operator
- $\underline{\sigma}_x, \underline{\sigma}_y, \underline{\sigma}_z$ - Pauli spin matrices
- \mathbf{I} - nuclear spin
- $\hat{1}$ - 2×2 unit matrix
- $F(\mathbf{Q})$ - total scattering amplitude
- $SAXS$ - small-angle x-ray scattering
- $F(QR)$ - form factor
- $S(Q)$ - structure factor
- MBE - molecular beam epitaxy
- $LEED$ - low energy electron diffraction
- UHV - ultra high vacuum
- $DWBA$ - distorted wave Born approximation
- $HADAS$ - the name of the neutron reflectometer
- $ASAXS$ - anomalous small-angle x-ray scattering

APPENDIX D: ACKNOWLEDGMENTS

Here, I would like to thank the following people without whom this work would not have been possible:

Prof. Dr. Thomas Brückel - for supervising my PhD work and editing the manuscript,

Dr. Emmanuel Kentzinger - for writing the simulation and fitting programs of specular and off-specular intensities for x-ray scattering,

Dr. Wiebke Sager and Dr. Klaus Pollmeier - for the synthesis of Co nanoparticles,

Dr. Ulrich Rücker - for the help in Fe/Cr/Fe sample preparation and for many fruitful discussions,

Dr. Werner Schweika - for the help in neutron measurements of MnO nanoparticles and analyzing the data,

Dr. Robert Mueller - for the help in construction of the empty cell for SQUID measurements,

Dr. Amitesh Paul - for the help in SQUID measurements of Co nanoparticles,

Dr. Günter Goerigk - for performing SAXS measurements of Co nanoparticles in solution,

Nicole Ziegenhagen, Dr. Yingang Wang, Dr. Dmitri Novikov, Dr. Wolfgang Caliebe and Dr. Oliver Seeck - for their contribution to the anomalous x-ray measurements of Fe/Cr/Fe trilayer,

Dr. Aurel Radulescu and Dr. Vitaliy Pipich - for sharing their experience and knowledge about SANS,

Dr. Sergey Vakhrushev - for the preparation of the MnO nanoparticles embedded in a porous glass,

Dr. Alexander Ioffe - for many fruitful discussions about neutron scattering technique.

And I am also very grateful to my family, my bride and all my friends for their enormous support.

APPENDIX E: CURRICULUM VITAE

Personal Data	
Name	Mikhail Feygenson
Date of Birth	10.07.1980
Place of Birth	Komsomolsk-on-Amure
Citizenship	Russian
Address	Meyburginsel 31/39, D52428 Jülich, Germany
Education	
1987-1997	School No.51,Komsomolsk-on-Amure
1997-2003	St. Petersburg State Polytechnical University (Experimental Physics Department)
2003-2007	RWTH Aachen (Department of Mathematics, Informatics and Nature Science)
Grades	Thesis Title
June 2001 (Bachelor of Physics)	"Chaotic dynamics of electrons in a quantum well in a tilted magnetic field"
June 2003 (Master of Physics)	"The theoretical and experimental investigation of resonance states in a Fe/Co/Fe neutron quantum well"

APPENDIX F: EIDESSTATTLICHE ERKLÄRUNG

Hiermit versichere ich an Eides statt, dass ich die Arbeit selbstständig verfasst habe und keine anderen Hilfsmittel als die angegebenen benutzt habe. Die Stellen der Arbeit, die anderen Werken dem Wortlaut oder dem Sinn nach entnommen sind, sind in jedem einzelnen Fall als Entlehnung unter Angabe der Quelle kenntlich gemacht. Das gleiche gilt auch für beigegebene Zeichnungen und Abbildungen.

Datum

Unterschrift

-
- [1] J. M. D. Coey J.All.Comp. 326 (2001) 2
 - [2] P. Grünberg, R. Schreiber, and Y. Pang and M. B. Brodsky and H. Sowers Phys. Rev. Lett. 57 (1986) 2442
 - [3] M. N. Baibich, J. M. Broto, A. Fert, F. Nguyen Van Dau and F. Petroff and P. Eitenne, G. Creuzet, A. Friederich, and J. Chazelas Phys.Rev.Lett. 61 (1988) 2472
 - [4] J. M. D. Coey JMMM 226-230 (2001) 2107
 - [5] S.A.Nikitin Soros Education Journal 8 (2004) 2
 - [6] W. H. Meiklejohn and C. P. Bean Phys. Rev. 102 (1956) 1413
 - [7] J. Nogués and I. K. Schuller JMMM 192 (1999) 203
 - [8] W. H. Meiklejohn J.Appl. Phys. 33 (1962) 1328
 - [9] P. Grünberg, "Magnetic Field Sensor With Ferromagnetic Thin Layers Having Magnetically Antiparallel Polarized Components", U.S. Patent 4,949,039.
 - [10] J. Belleson <http://www.hitachigst.com>
 - [11] C. Kittel *Introduction to Solid State Physics* (New York) 1987
 - [12] D. L. Leslie-Pelecky and R. D. Rieke Chem. Mater. 8 (1996) 1770
 - [13] S. Mørup and B. R. Hansen Phys.Rev. B 72 (2005) 024418
 - [14] E. P. Wohlfarth JMMM 39 (1983) 39
 - [15] J. Hormes and H. Modrow and H. Bönnemann and C. S. S. R. Kumar J.Appl.Phys. 97 (2005) 10R102
 - [16] D. Sudfeld and K. Wojczykowski and W. Hachmann and P. Jutzi and G. Reiss and A. Hütten J.Appl.Phys. 93 (2003) 7328
 - [17] J. M. D. Coey Phys.Rev.Lett. 27 (1971) 1140
 - [18] R. H. Kodama and A. E. Berkowitz and E. J. McNiff, Jr. and S. Foner J.Appl.Phys. 81 (1997) 5552
 - [19] R. H. Kodama and A. E. Berkowitz Phys.Rev.B 59 (1999) 6321
 - [20] K. Haneda and H. Kojima and A. H. Morrish and P. J. Picone and K. Wakai J.Appl.Phys. 53 (1982) 2686
 - [21] D. Lin, A. C. Nunes, C. F. Majkrzak and A. E. Berkowitz JMMM 145 (1995) 343

- [22] F. Gazeau, J. C. Bacri, F. Gendron, R. Perzynski, Yu. L. Raikher, V. I. Stepanov and E. Dubois JMMM 186 (1997) 175
- [23] F. Gazeau, E. Dubois and M. Hennion Europhys.Lett. 40 (1997) 575
- [24] R. H. Kodama and A. E. Berkowitz and E. J. McNiff, Jr. and S. Foner Phys.Rev.Lett. 77 (1996) 394
- [25] F. Liu, M. R. Press, S. N. Khanna, and P. Jena Phys.Rev.B 39 (1989) 6914
- [26] R. H. Kodama JMMM 200 (1999) 359
- [27] J. P. Chen, C. M. Sorensen, and K. J. Klabunde and G. C. Hadjipanayis Phys.Rev.B 51 (1995) 11527
- [28] H. Kachkachi, A. Ezzir, and M. Noguès Eur.Phys.J. B 14 (2000) 681
- [29] P. Prené, E. Tronc, J. P. Jolivet, J. Livage, R. Cherkaoui, M. Noguès and J. L. Dormann Hyper. Inter. 93 (1994) 1049
- [30] A. Wiedenmann Physica B 356 (2005) 246
- [31] A. Wiedenmann J.Appl.Cryst. 33 (2000) 428
- [32] A. Wiedenmann A. Hoell, M. Kammel and P. Boesecke Phys.Rev.E 68 (2003) 031203-1
- [33] X. Batlle and A. Labarta J.Appl.Phys.D 35 (2002) R15
- [34] S. Mørup, C. Frandsen, F. Bødker, S. N. Klausen, K. Lefmann, P.-A. Lindgård and M. Hansen Hyper.Inter. 144/145 (2002) 347
- [35] S. Mørup F. Bødker, P. V. Hendriksen, and S. Linderøth Phys.Rev.B 52 (1995) 287
- [36] M. F. Hansen and C. B. Koch and S. Mørup Phys.Rev.B 62 (2000) 1124
- [37] S. Mørup and E. Tronc Phys.Rev.Lett. 72 (1994) 3278
- [38] J. I. Martin, J. Nogués, K. Liu, J. L. Vicent and I. K. Schuller JMMM 256 (2003) 449
- [39] M. F. Hansen and S. Mørup JMMM 184 (1998) L262
- [40] C. Petit, A. Taleb and P. Pileni Adv.Mater. 10 (1998) 259
- [41] M.F.Collins *Magnetic Critical Scattering*(New York) 1989
- [42] W. G. Williams *Polarized Neutrons* (Oxford) 1988
- [43] W. Schweika *Introduction to Polarized Neutron Scattering*, Lecture in Polarized Neutron Scattering Course at FRJ, IFF (2002)
- [44] B. P. Toperverg *Polarized Neutron Reflection and Off-Specular Scattering* Lecture in Polarized Neutron Scattering Course at FRJ, IFF (2002)

- [45] G. Shirane, Y. J. Uemura, and J. P. Wicksted and Y. Endoh and Y. Ishikawa Phys.Rev.B 31 (1985) 1227
- [46] P. Lindner "Scattering Experiments: Experimental Aspects, Initial Data Reduction and Absolute Calibration", lecture in the European Summer School on "SCATTERING METHODS APPLIED TO SOFT CONDENSED MATTER", Bombannes 2002
- [47] <http://www.hmi.de/>
- [48] G.Binash, P. Grünberg, F. Saurenbach and W. Zinn Phys. Rev. B 39 (1989) 4828
- [49] J.-G. Zhu and Y. Zheng and G. A. Prinz J.Appl.Phys. 87 (2000) 6668
- [50] M. M. Miller, P. E. Sheehan, R. L. Edelstein, C. R. Tamanaha, L. Zhong, S. Bounnak, L. J. Whitman and R. J. Colton JMMM 225 (2001) 138
- [51] S.S.P. Parkin, IBM J. Res. Develop. 42 (1) (1998) 3
- [52] T. Thomson and P. C. Riedi and D. Greig Phys. Rev. B 50 (1994) 10319
- [53] D. Olligs D. E. Bürgler, Y. G. Wang, E. Kentzinger, U. Rücker, R. Schreiber, Th. Brückel and P. Grünberg Europhys. Lett. 59 (2002) 458
- [54] A. Paul, A. Gupta, S. M. Chaudhari and D. M. Phase Vacuum 60 (2001) 401
- [55] E. E. Fullerton D. M. Kelly, J. Guimpel, and I. K. Schuller and Y. Bruynseraede Phys. Rev. Lett. 68 (1992) 859
- [56] P. M. Levy, S. Zhang and A. Fert Phys. Rev. Lett. 65 (1990) 1643
- [57] J.Inoue, A. Oguri, S. Maekawa J. Phys. Soc. Jpn. 60 (1991) 376
- [58] C.M.Schmidt et.al., J. Appl. Pys. 89 (2001) 181
- [59] V. Nitz, M. Tolan, J.-P. Schlomka, O. H. Seeck, J. Stettner, and W. Press and M. Stelzle and E. Sackmann Phys.Rev.B 54 (1996) 5038
- [60] U. Zimmermann, J.-P. Schlomka, M. Tolan, J. Stettner, and W. Press and M. Hacke and S. Mantl J. Appl. Phys. 83 (1998) 5823
- [61] J. Stettner, L. Schwalowsky, O. H. Seeck, M. Tolan, and W. Press and C. Schwarz and H. v. Känel Phys. Rev. B 53 (1996) 1398
- [62] U. Rücker, Schichtsysteme aus ferromagnetischen Metallen und magnetischen Halbleitern, Diploma thesis, University of Cologne,(1994)
- [63] D. E. Bürgler, C. M. Schmidt, D. M. Schaller, F. Meisinger, R. Hofer, and H.-J. Güntherodt Phys.Rev. B 56 (1997) 4149

- [64] C. M. Schmidt, D. E. Bürgler, D. M. Schaller, F. Meisinger, and H.-J. Güntherodt Phys. Rev. B 60 (1999) 4158
- [65] Z. H. Ming, A. Krol, Y. L. Soo and Y. H. Kao and J. S. Park and K. L. Wang Phys.Rev.B 47 (1993) 16373
- [66] L. Nevot and P. Croce Phys.Appi. 15 (1980) 761
- [67] http://www.cxro.lbl.gov/optical_constants/getdb2.html
- [68] S. K. Sinha, E. B. Sirota, and S. Garoff and H. B. Stanley Phys. Rev. B 38 (1988) 2297
- [69] V. Holý, J. Kuběna, and I. Ohlídal and K. Lischka and W. Plotz Phys. Rev. B 47 (1993) 15896
- [70] L. G. Parratt Phys. Rev. 95 (1954) 359
- [71] J. Stettner, Charakterisierung von rauhen MBE- $CoSi_2$ /Si-Schichtsystemen mittels Röntgenstreuung, PhD thesis, University of Kiel,(1995)
- [72] P. Debye Ann.Physik 43 (1914) 49
- [73] J.-P. Schlomka, M. Tolan, L. Schwalowsky, O. H. Seeck, J. Stettner, and W. Press Phys. Rev. B 51 (1995) 2311
- [74] V.Holý *High-resolution x-ray scattering from thin films and multilayers* (Springer) 1999
- [75] I. D. Kaendler, O. H. Seeck and J.-P. Schlomka, M. Tolan, W. Press, and J. Stettner and L. Kappius and C. Dieker and S. Mantl J. Appl. Phys. 87 (2000) 133
- [76] F. Prokert, N. Schell, A. Gorbunov Nucl. Instr. and Meth. in Phys. Res. B 199 (2003) 123
- [77] A. Gupta, A. Paul, M. Gupta, C. Meneghini, U. Pietsch, K. Mibu, A. Maddalena, S.D.S. Dal Toé and G. Principi JMMM 272-276 (2004) 1219
- [78] P. Levitz, G. Ehret and S. K. Sinha and J. M. Drake J.Chem.Phys. 95 (1991) 6151
- [79] I. V. Golosovsky I. Mirebeau, G.André, D. A. Kurdyukov, Yu.A. Kumzerov, and S. B. Vakhru-shev Phys.Rev.Lett. 86 (2001)
- [80] C. G. Shull W. A. Strauser, and E. O. Wollan Phys.Rev. 83 (1951) 333
- [81] B. Morosin Phys.Rev. B 1 (1970) 236
- [82] W. Schweika and P.Böni Physica B 297 (2001) 155
- [83] http://www.fz-juelich.de/iff/wns_dns
- [84] R. Lipowsky Ferroelectrics 73(1987) 69
- [85] W. Schweika and D. P. Landau and K. Binder Phys.Rev.B 53 (1996) 8937

- [86] C. B. Murray, S. Sun, W. Gaschler, H. Doyle, T. A. Betley and C. R. Kagan IBM J. Res. Dev., 45 (2001) 47
- [87] C. Petit, A. Taleb, M. P. Pileni J. Phys. Chem. B 103 (1999) 1805
- [88] G.S. Attard, J.C. Glyde, C.G. Göltner Nature 378 (1995) 366
- [89] J. Tanori, M.P. Pileni Langmuir 13 (1997) 639
- [90] J. D. Hopwood, S. Mann Chem. Mat. 9 (1997) 1819
- [91] L. M. Gan, T.D. Li, C. H. Chew, W. K. Teo, L. H. Gan Langmuir 11 (1995) 3316
- [92] W. Sager, *IFF – Ferienkurs* 33 (2002)
- [93] I. Lisiecki and M. P. Pileni Langmuir 19 (2003) 9486
- [94] G. Beaucage, H. K. Kammler and S. E. Pratsinis J.Appl.Cryst. 37 (2004) 523
- [95] V. V. Ustinov, L. N. Romashev, T. P. Krinitsina, E. A. Kravtsov, M. A. Milyaev, A. V. Semerikov, V. A. Tsurin, N. V. Kourtina JMMM 240 (2002) 511
- [96] W. S. Dubner, J. M. Schultz, G. D. Wignall J.Appl.Cryst. 23 (1990) 469
- [97] A. Maconnachie Polymer 25 (1984) 1068
- [98] J. S. Pedersen, D. Posselt and K. Mortensen J.Appl.Cryst. 23 (1990) 321
- [99] M. J. Mehl and D. Papaconstantopoulos Phys.Rev.B 54 (1996) 4519
- [100] V. Castelletto and I. W. Hamley Curr.Opin.Coll.Inter.Sci 7 (2002) 167
- [101] R. Lund, L. Willner, J. Stellbrink, A. Radulescu and D. Richter Macromolecules 37 (2004) 9984
- [102] <http://www.ncnr.nist.gov/resources/n-lengths/>
- [103] V. K. Pecharsky and P.Y.Zavalij *Fundamentals of Powder Diffraction and Structural Characterization of Materials*